

Multifunctional Silica Particles as Contrast Agents for Optical
and Magnetic Resonance Imaging

Multifunktionale Silica-Partikel als Kontrastmittel
für Optische Bildgebung und Magnetresonanztomographie

DISSERTATION

der Mathematisch-Naturwissenschaftlichen Fakultät
der Eberhard Karls Universität Tübingen
zur Erlangung des Grades eines
Doktors der Naturwissenschaften
(Dr. rer. nat.)

vorgelegt von
DIPL.-CHEM. VERENA FELDMANN
aus München

Tübingen
2011

Tag der mündlichen Prüfung:

29.11.2011

Dekan:

Prof. Dr. Wolfgang Rosenstiel

1. Berichterstatter:

Prof. Dr. Hermann A. Mayer

2. Berichterstatter:

Prof. Dr. Reiner Anwander

Die vorliegende Arbeit wurde im Zeitraum von April 2009 bis September 2011 am Institut für Anorganische Chemie der Eberhard Karls Universität Tübingen unter Anleitung von Herrn Prof. Dr. Hermann A. Mayer angefertigt.

Meinem Doktorvater,

Herrn Prof. Dr. Hermann A. Mayer,

danke ich herzlich für die Bereitstellung des interessanten Themas, die zahlreichen wertvollen Anregungen und Diskussionen, sein stetes Interesse an meiner Arbeit, das hervorragende Arbeitsklima, sowie die Möglichkeit, meine Ergebnisse auf internationalen Konferenzen zu präsentieren.

Dem Bundesministerium für Bildung und Forschung (BMBF) danke ich für die finanzielle Unterstützung im Rahmen des Verbundprojektes FKZ 01EZ0812.

Danksagung

Dem Arbeitskreis Mayer – Dr. David Ruiz Abad, Dr. Cornelia Futter, Dr. Jörg Henig, Filiz Kocak, Dr. Wolfgang Leis, Marc Stickel, Helene Strauch und Sophie Wernitz – möchte ich für das freundschaftliche Klima und die gute Zusammenarbeit danken.

Dem Arbeitskreis Speiser, insbesondere Adrian Ruff und Dr. Nicolas Plumeré, danke ich für die gute Zusammenarbeit.

Dem Arbeitskreis Gauglitz und den Mitarbeitern der Biometrics GmbH danke ich für die hervorragende Zusammenarbeit, die Tipps zum Umgang mit den Antikörpern und dafür, dass ich Geräte und Ressourcen nutzen konnte.

Bei Dr. Klaus Eichele möchte ich mich herzlich für die Einführung in die praktische (Festkörper-) NMR-Spektroskopie bedanken.

Für die REM-Aufnahmen am XL 30-FEG von Philips danke ich Peter Nill, Inst. f. Angewandte Physik, am ZEISS DSM 962 Prof. Dr. Thomas Chassé und Elke Nadler, am FEI ESEM Dual Beam Quanta 3D FEG Dr. Jörg Henig, CES, Ruhr-Universität Bochum.

Dr. Thomas Wendel und Annegret Walz vom Inst. f. Geologie und Paläontologie danke ich für den Zugang zur ASAP 2010, Prof. Dr. Reiner Anwander zur ASAP 2020.

Dr. Jochen Glaser und Markus Kalmutzki danke ich für die Aufnahme der TG-Messungen.

Prof. Dr. Rolf Daniels und Klaus Weyhing, Pharmazeutische Technologie, danke ich für den Zugang zum Zetasizer und für die Hilfe bei den Messungen.

Dr. Jörn Engelmann, Dr. Rajendra Joshi, Dr. Sven Gottschalk und Hildegard Schulz, Max-Planck-Institut für biologische Kybernetik, Tübingen, möchte ich herzlich für die schöne Kooperation, sowie die Experimente in den MR-Tomographen und die Zellstudien danken.

Dr. Wolfgang Koestner und Prof. Dr. Martin G. Sauer, Medizinische Hochschule Hannover, danke ich ebenfalls für die schöne Kooperation, sowie für die Analysen der Antikörper-funktionalisierten NPs und die fluoreszenzmikroskopischen Untersuchungen *in vitro* und *in vivo*.

Danke Flo, für alles.

Contributions

Parts of this work are results from collaborations with Dr. Jörn Engelmann, Dr. Rajendra Joshi and Dr. Sven Gottschalk (High-Field Magnetic Resonance Center, Max Planck Institute for Biological Cybernetics, Tübingen, Germany) and Dr. Wolfgang Koestner and Prof. Dr. Martin G. Sauer (Pediatric Hematology & Oncology, Hannover Medical School, Hannover, Germany). Collaborations were performed in the frame of a project, funded by the German Ministry for Education and Research (BMBF, FKZ 01EZ0812, -13, -14) and by the HILF (“Hochschulinterne Leistungsförderung”) program of Hannover Medical School (Dr. Koestner).

The MRI experiments (chapter 4.6) and the cell studies (chapter 4.7.2.2), Figures 4.24, 4.25 and 4.26 and the relaxivity values in Table 4.22 and 4.23 were performed, generated, and provided by Dr. Jörn Engelmann, Dr. Sven Gottschalk and Dr. Rajendra Joshi. Figure 4.27 and 4.28, the western blot assay and its results (chapter 4.8.2.1) and the enzyme-linked immunosorbent assay and its results (chapter 4.8.2.2) were developed, performed, and provided by Dr. Wolfgang Koestner.

A further collaboration on the synthesis of silica particles existed with Prof. Dr. Bernd Speiser (Institute for Organic Chemistry, Tübingen, Germany) and Dr. Nicolas Plumeré (CES, Ruhr-Universität Bochum, Germany). Results are submitted for publication and parts of chapter 4.2 are taken from ref. 64.

Publications

Feldmann, V.; Gottschalk, S.; Engelmann, J.; Mayer, H. A.:

“Synthesis, Characterisation and Examination of Gd[DO3A-hexylamine]-functionalised Silica-Nanoparticles as Contrast Agent for MRI-Applications” (*J. Colloid Interface Sci.* **2012**, *366*, 70-79)

Plumeré, N.; Ruff, A.; Speiser, B.; Feldmann, V.; Mayer H. A.:

“Redox-active Silica Nanoparticles. Part 5. Stöber Silica Particles as Basis for Redox Modifications – Particle Shape, Size, Polydispersity and Porosity.” (*J. Colloid Interface Sci.*, doi:10.1016/j.jcis.2011.10.070)

Janisch, J.; Ruff, A.; Speiser, B.; Wolff, C.; Zigelli, J.; Benthin, S.; Feldmann, V.; Mayer, H. A.:

“Consistent Diffusion Coefficients of Ferrocene in some Non-Aqueous Solvents: Electrochemical Simultaneous Determination together with Electrode Sizes and Comparison to Pulse Gradient Spin Echo NMR Results” (*J. Solid State Electrochem.* **2011**, *15*, 2083-2094)

Posters

Electrochemistry 2010, 2010, Bochum, Germany:

Ruff, A.; Janisch, J.; Wolff, C.; Zigelli, J.; Speiser, B.; Feldmann, V.; Mayer, H. A.

“Consistent Simultaneous Determination of Diffusion Coefficients and Electrode Dimensions by Means of Cyclic Voltammetry at Macro- and Microelectrodes”

2nd International Conference on Multifunctional, Hybrid and Nanomaterials: “Hybrid Materials”, 2011, Strasbourg, France:

Feldmann, V.; Joshi, R.; Engelmann, J.; Koestner, W.; Sauer, M. G.; Mayer, H. A.

“Multifunctional Silica Nanoparticles for Optical and Magnetic Resonance Imaging”

6th European Molecular Imaging Meeting, 2011, Leiden, the Netherlands:

Feldmann, V.; Engelmann, J.; Gottschalk, S.; Joshi, R.; Koestner, W.; Sauer, M. G.; Mayer, H. A.

“Synthesis, Characterisation and Examination of Gd(III)chelate-functionalised Silica Nanoparticles as Contrast Agents for MRI”

6th European Molecular Imaging Meeting, 2011, Leiden, the Netherlands:

Joshi, R.; Feldmann, V.; Koestner, W.; Mayer, H. A.; Sauer, M. G.; Engelmann, J.

“Silica nanoparticles with multiple functionalities for optical and magnetic resonance imaging applications”

COST Action D38, 2011, Oxford, UK:

Feldmann, V.; Joshi, R.; Gottschalk, S.; Engelmann, J.; Koestner, W.; Sauer, M. G.; Mayer, H. A.

“Multifunctional Silica Nanoparticles for Optical and Magnetic Resonance Imaging Applications”

Nanotoday Conference, 2011, Waikoloa Beach, HI, USA:

Feldmann, V.; Engelmann, J.; Joshi, R.; Gottschalk, S.; Koestner, W.; Sauer, M. G.; Mayer, H. A.

“Multifunctional Silica Nanoparticles for Optical and Magnetic Resonance Imaging Synthesis, Characterisation and Examination”

Table of Contents

Abbreviations.....	IV
1 Introduction.....	1
2 Aim of this Work.....	3
3 General Basics.....	4
3.1 Stöber Particles.....	4
3.1.1 Sol-Gel Processing of Aqueous Silicates.....	4
3.1.2 The Stöber Process.....	8
3.2 Functionalisation of Silicas.....	9
3.2.1 Silanisation.....	9
3.2.2 Hydrosilylation.....	10
3.2.3 Photochemical Hydrosilylation.....	10
3.3 Characterisation.....	11
3.3.1 Physisorption Isotherms.....	11
3.3.1.1 Specific Surface Area.....	11
3.3.1.2 Porosity.....	12
3.3.2 Dynamic Light Scattering (DLS).....	13
3.3.3 Diffuse Reflectance Infrared Fourier Transform Spectroscopy (DRIFTS).....	14
3.3.4 Scanning Electron Microscopy (SEM).....	15
3.4 Magnetic Resonance Imaging (MRI).....	16
3.4.1 MRI Contrast Agents.....	17
3.5 Nanoparticulate Contrast Agents.....	19
4 Results and Discussion.....	20
4.1 Syntheses of LnDOTA- and LnDO3A-Derivatives.....	20
4.2 Syntheses and Characterisation of Stöber Particles.....	23
4.2.1 Synthesis of Stöber Particles.....	23
4.2.2 Characterisation of Stöber Particles.....	24
4.2.2.1 Size and Shape.....	24
4.2.2.2 Spectroscopic Investigations.....	26
4.2.2.3 Specific Surface Area and Porosity of the Stöber Particles.....	29
4.2.2.4 Specific Surface Concentration of $\equiv\text{Si-OH}$ Groups.....	30
4.3 Surface Modification of Stöber Particles.....	31

4.3.1	Silanisation.....	32
4.3.2	Chlorination-Reduction.....	32
4.3.3	Characterisation of Surface Modified Stöber Particles.....	33
4.3.3.1	Size and Shape.....	33
4.3.3.2	Particle-Particle Interactions.....	34
4.3.3.3	Spectroscopic Investigations.....	36
4.3.3.4	Specific Surface Area of the surface modified Stöber Particles.....	40
4.3.3.5	Specific Surface Concentration of Functional Groups.....	41
4.4	Coupling of Ln[DOTA] and Ln[DO3A] Derivatives to M1C ₃ NH ₂ and M2GOPTS	42
4.4.1	Syntheses.....	42
4.4.2	Characterisation.....	44
4.4.2.1	Size and Shape.....	44
4.4.2.2	Particle-Particle Interactions.....	44
4.4.2.3	Spectroscopic Investigations.....	45
4.4.2.4	Specific Surface Concentration of Gadolinium.....	47
4.5	Further Functionalisation of Si-H modified Materials M3SiH and M4SiH.....	48
4.5.1	Syntheses.....	48
4.5.1.1	Photochemical Hydrosilylation.....	48
4.5.1.2	Coupling of Ln[DO3A-HA].....	49
4.5.1.3	Coupling of Y[DOTA-ButAm].....	50
4.5.2	Characterisation and Examination.....	50
4.5.2.1	Size and Shape.....	50
4.5.2.2	Particle-Particle Interactions.....	51
4.5.2.3	Spectroscopic Investigations.....	54
4.5.2.4	Specific Surface Concentration of Functional Groups.....	56
4.5.2.5	Specific Surface Concentration of Gadolinium.....	59
4.5.2.6	Stability under Physiological Conditions.....	61
4.6	Magnetic Resonance Imaging of Gd(III) modified NP Containing Agar Phantoms	61
4.7	Multifunctionality.....	67
4.7.1	Syntheses of Bimodal Silica Particles.....	67
4.7.2	Characterisation and Examination of Bimodal NPs.....	68
4.7.2.1	Specific Surface Concentration of Gadolinium.....	68
4.7.2.2	<i>in vitro</i> Cell Studies.....	69

4.7.2.3	<i>in vivo</i> Studies	70
4.8	Antibody modified Stöber Particles.....	71
4.8.1	Synthesis.....	71
4.8.2	Examination of AB modified NPs.....	72
4.8.2.1	Western Blot.....	72
4.8.2.2	ELISA.....	73
5	Conclusion.....	75
6	Experimental Part.....	77
6.1	Syntheses of the Lanthanide Complexes	77
6.1.1	Solvents and Reagents	77
6.1.2	Analytical methods	77
6.1.3	Syntheses	78
6.1.3.1	Synthesis of Gd[DO3A-HA] (3)	78
6.1.3.2	Synthesis of Y[DO3A-HA] (2)	78
6.1.3.3	Synthesis of DOTA-ButAm (10)	78
6.1.3.4	Synthesis of Y[DOTA-ButAm]Na (11)	80
6.1.3.5	Synthesis of DOTA-BA (4)	81
6.1.3.6	Synthesis of Ln[DOTA-BA][<i>n</i> -Bu ₄ N] (5, 6).....	81
6.1.3.7	Synthesis of DOTA-GA (7)	81
6.1.3.8	Synthesis of Ln[DOTA-GA][<i>n</i> -Bu ₄ N] (8, 9)	81
6.2	Syntheses and Modification of Silica Nanoparticles	81
6.2.1	Solvents, Reagents and Equipment	81
6.2.2	Characterisation Methods	82
6.2.3	Syntheses	86
7	References	92
8	Summary	97
9	Zusammenfassung.....	101

Abbreviations

A	specific surface area
AB	antibody
AES	atomic emission spectrometer
APTES	(3-aminopropyl)triethoxysilane
B	magnetic field
BET	Brunauer-Emmet-Teller
CA	contrast agent
CP	cross polarisation
Γ	surface concentration
δ	chemical shift in ppm (NMR)
δ	bending vibration (IR)
d	diameter
D	diffusion coefficient
DCM	dichloromethane
DIC	<i>N,N'</i> -diisopropylcarbodiimide
DIPEA	<i>N,N</i> -diisopropylethylamine
DLS	dynamic light scattering
DMF	dimethylformamide
DMSO	dimethyl sulfoxide
DOTA	1,4,7,10-tetraazacyclo-dodecane-1,4,7,10-tetracetic acid
DO3A	1,4,7,10-tetraazacyclo-dodecane-1,4,7-triacetic acid
DRIFT	diffuse reflectance infrared fourier transform
EC	endothelial cell
EDC	<i>N</i> -(3-dimethylaminopropyl)- <i>N'</i> -ethylcarbodiimide hydrochloride
EDTA	ethylenediaminetetraacetic acid
ELISA	enzyme-linked immunosorbent assay
eq.	molar equivalents
ESI	electrospray ionisation
Et	ethyl (-CH ₂ -CH ₃)
EtOH	ethanol
FITC	fluorescein isothiocyanate

GVHD	graft versus host disease
G	magnetic field gradient (strength)
GOPTS	(3-glycidyloxypropyl)trimethoxysilane
h	Planck constant
η	viscosity
HBSS	hank's balanced salt solution
HPDEC	high power decoupling
HRP	horseradish peroxidase
IR	infrared
<i>i.v.</i>	intravenous
J	coupling constant (NMR)
k_B	Boltzmann constant
m	multiplet (NMR)
m	mass
MAS	magic angle spinning
Me	methyl (-CH ₃)
MeOH	methanol
MRI	magnetic resonance imaging
MS	mass spectrometry
m/z	mass to charge ratio (MS)
N_A	Avogadro constant
NHS	<i>N</i> -hydroxysuccinimide
NMR	nuclear magnetic resonance
ν	stretching vibration (IR)
$\tilde{\nu}$	wave number in cm ⁻¹ (IR)
p^0	saturation pressure
p/p^0	relative pressure
PBS	phosphate buffered saline
PDI	polydispersity index
PEG	polyethylene glycol
ppm	parts per million
ρ	(spin) density
r_1	longitudinal relaxivity

r_2	transverse relaxivity
RES	reticuloendothelial system
rpm	rounds per minute
RT	room temperature
SDP	size distribution processor
σ	standard deviation
t	time
<i>t</i> -	<i>tert</i> -
T	temperature
T_1	longitudinal relaxation time
T_2	transverse relaxation time
TBTU	<i>O</i> -(benzotriazol-1-yl)- <i>N,N,N',N'</i> -tetramethyluronium tetrafluoroborate
TEOS	tetraethyl orthosilicate
TES	triethoxysilane
V	volume

1 Introduction

Magnetic resonance imaging (MRI) is an imaging technique which is applied in clinical diagnostics since the 1980s. MRI generates sectional images of the human body by means of magnetic fields and radio waves. It is particularly suitable to image soft tissues like the brain and internal organs and has revolutionised the diagnosis of tumors. MRI is based on the principles of nuclear magnetic resonance (NMR) spectroscopy and detects the ^1H NMR signal of the water protons, which are ubiquitous in the human body (the human body consists of more than 55% of water). However, the development of MRI towards one of the most powerful techniques in clinical diagnosis was only enabled by the development and use of paramagnetic contrast agents (CAs) to enhance imaging sensitivity. The effects of CAs are based on the change of relaxation times of the water protons in the presence of paramagnetic compounds with unpaired electrons. There are T_1 and T_2 CAs which generate contrast via longitudinal and transverse relaxation processes, respectively. The major advantage of T_1 CAs is a positive signal enhancement, which leads to brighter regions in MR images. Most of the currently applied CAs for enhanced T_1 -contrast are based on gadolinium(III) chelate complexes and are mainly extracellular agents, which only distribute non-specifically throughout the circulatory system and interstitial spaces.¹⁻⁵ Since those agents are excreted easily and quite fast from the body, they are suitable for routine examinations, but not for long-term tracking applications,⁶ which are currently developed to not only diagnose but also treat diseases on a molecular level (theranostics). Therefore, nano-sized materials with longer blood circulation half-life times were developed and they are gaining increasing importance in medical diagnosis and treatments. By tailoring hybrid nanomaterials, consisting of an inorganic matrix and functional organic moieties, materials with special properties can be made for various purposes, such as carriers of drugs or for imaging techniques.⁷⁻¹² CA-loaded materials combined with smart or targeting units, which respond to physiological changes (e.g. in pH or ion concentrations) and track special kinds of tissues or cells, promise to identify diseases on a molecular level and thus, in an early stage.¹³⁻¹⁷

Silica nanoparticles (NPs) can serve as such an inorganic matrix and bring several advantages. They are promising carriers with a great surface modification capability and good biocompatibility. By coupling Gd(III) complexes to the particle surface, large payloads of CA molecules can be obtained in a minimum of space. Thus, because of the high local concentration of CA molecules nano-sized materials can act as contrast amplifiers and result

in an improved resolution and sensitivity. Furthermore, due to various functionalisation opportunities, silicas can serve as matrices not only for CA molecules, but also for targeting or smart units, as well as biocompatible moieties, such as polyethylene glycol (PEG), and biomolecules, such as peptides and antibodies. This makes them ideal candidates to serve as matrix in the synthesis of multimodal CAs.^{13,14,17-21}

2 Aim of this Work

The aim of the present work is the preparation of multifunctional CAs for MRI and optical imaging (OI), based on non porous silica NPs with diameters of 50-100 nm. Gadolinium(III) ions embedded in a macrocyclic ligand system will be covalently attached to the surface of the NPs with different spacers and by different ways of functionalisation of the matrix. Therefore, the DOTA ligand of the established contrast agent DotaremTM (Figure 2.1) has to be modified with further functional groups to allow coupling of the Gd(III) complex to the surface of the matrix.

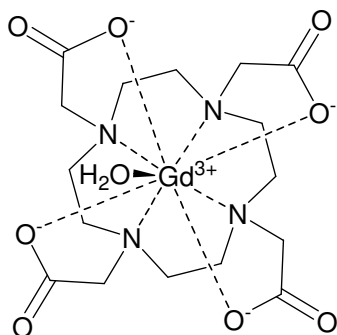
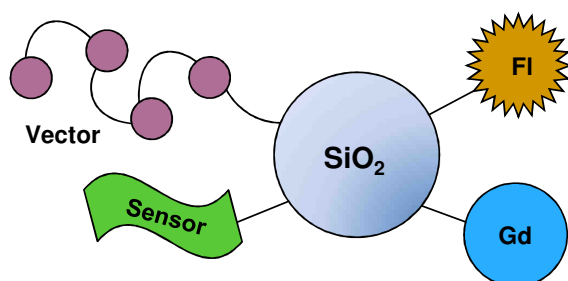


Figure 2.1 The clinical CA DotaremTM (Guerbet GmbH).

The silica particles serve as carrier to maximise the concentration of CA molecules in a minimum of space. Besides Gd(III) functionalised NPs for MRI, multimodal materials will be synthesised by additionally coupling fluorophores for OI applications.



Vector: tissue/cell uptake enhancer (e.g. cell penetrating peptide) improvement of biocompatibility (peptide, PEG)
Sensor: targeting unit (e.g. antibody or peptide)
FI: fluorophore (e.g. FITC, Cy 5.5)
Gd: MR-detectable Gd(III)chelate

Figure 2.2 Multimodal silica nanoparticle.

Coupling of peptides, and antibodies to the NP surface allows molecular imaging (Figure 2.2). The materials will be fully characterised after each synthetic step to carefully determine the extent of surface modification and to examine the properties of the nanoparticles. The stability of the new CAs will be tested under physiological conditions with respect to leaching of the complexes from the surface as well as to the release of gadolinium from the macrocyclic ligands. Finally, the suitability of Gd(III) containing materials as CAs will be investigated with a 3T MRI human whole body scanner. Additionally the cellular uptake *in vitro* and the biodistribution *in vivo* of the particles will be examined by fluorescence microscopy.

3 General Basics

3.1 Stöber Particles

3.1.1 Sol-Gel Processing of Aqueous Silicates²²⁻²⁴

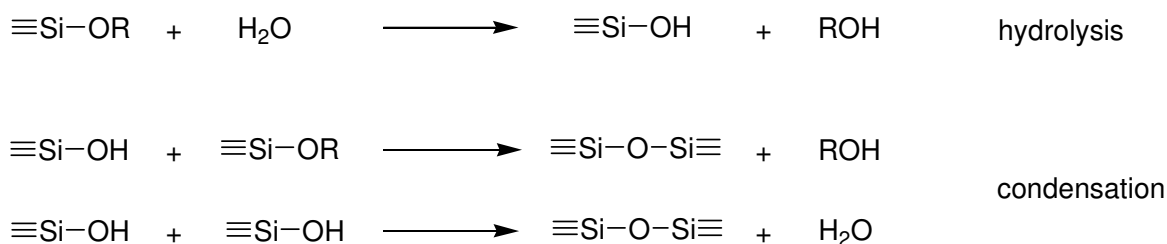
Sol-Gel processing provides a pathway to making solids not by crystallisation or precipitating like in conventional reactions, but by gelation. In polycondensation reactions of precursor molecules, oxidic networks are formed in solution. Typical precursors are the alkoxides of silicon, aluminium, titanium, and zirconium. A sol is a colloidal suspension of solid particles or polymers in a liquid phase, in which the particles may be amorphous or crystalline, but do not precipitate. A gel consists of a porous, three-dimensional, continuous, solid network, which encloses a liquid. In most of the sol-gel processes gelation is caused by the formation of covalent bonds. Starting from a sol, various kinds of materials can be made, such as fibres, powders, thin films, non porous glasses and ceramics, porous solids, as well as non porous nanoparticles. Sol-Gel derived materials are widely applicable, e.g., as coatings, matrices for catalysts, ceramic fibres and powders, heat insulations, glasses, etc.

Below, principle basics of silicon-based sol-gel processing are defined. The process can be divided into five main sub-steps.

1. Hydrolysis
2. Condensation
3. Gelation
4. Ageing
5. Drying

Hydrolysis and Condensation

Hydrolysis and condensation reactions can basically be described by the following three reaction equations (Scheme 3.1):



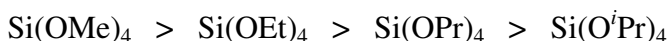
Scheme 3.1 Hydrolysis and condensation.

Hydrolysis and condensation run simultaneously as competitive reactions. Sol-particles with diameters of 1-1000 nm are formed.

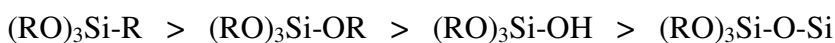
In the “top-down-synthesis”, aqueous solutions of sodium-silicates (“ Na_2SiO_3 ”, waterglass) are used as precursors. In contrast, the “bottom-up-synthesis” starts from monomeric tetra-alkyl silicates, like $\text{Si}(\text{OMe})_4$ or $\text{Si}(\text{OEt})_4$ and works in organic solvents. There are various parameters, which influence the hydrolysis- and condensation reactions in the bottom-up-synthesis. These parameters provide the opportunity to influence and even control the reactions and therefore, the materials formed in a process. Below, these parameters are described.

- The Nature of the Precursor

The reaction rate decreases with increasing size of the substituents of the precursor, because of sterical hindrance:

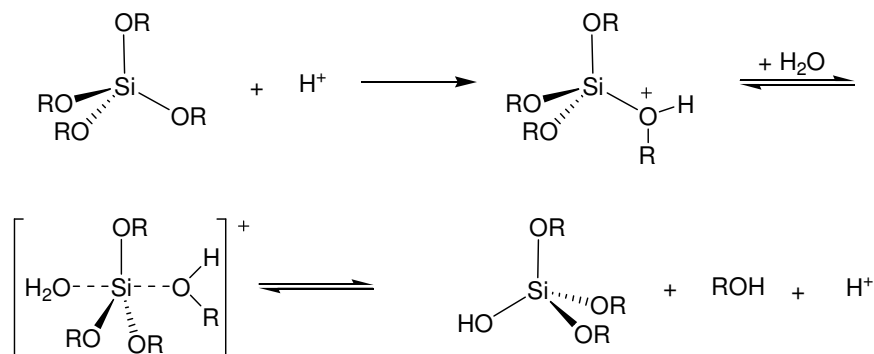


Inductive effects of the substituents of the precursor also play a decisive role, as they can stabilise or destabilise transition states. The electron density at the silicon atom decreases in the following order:



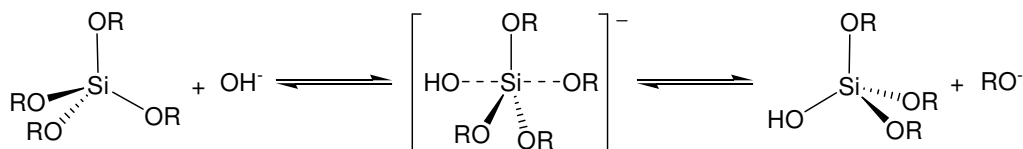
- The pH Value

Under acidic conditions, a proton attacks an oxygen atom of one of the alkoxy moieties, followed by water attacking the silicon atom, yielding a five-coordinated positively charged transition state, which is stabilised by the inductive effects of the residual alkoxy moieties (Scheme 3.2). At the beginning, there are three alkoxy moieties left, so the first step is the most rapid, and following attacks of protons run more slowly, allowing condensation reactions to follow directly. Thus, under acidic conditions, a high electron density at the silicon atom and therefore, the reaction at a terminal silicon, are favourable at the beginning, preferentially leading to chain-like networks and non porous materials with high densities.



Scheme 3.2 Acidic catalysis of the hydrolysis in sol-gel processes.

Under alkaline conditions, a hydroxide anion attacks the silicon atom, yielding a five-coordinated negatively charged transition state, which is destabilised by the residual alkoxy moieties (Scheme 3.3). Thus, here the first attack runs more slowly than the following ones. In contrast to the acidic catalysis, condensation reactions run more slowly. So, at the beginning, a low electron density at the silicon atom is favourable, central silicon atoms are preferably attacked, leading to branched networks and big particles with big pores.



Scheme 3.3 Alkaline catalysis of the hydrolysis in sol-gel processes.

- The Water Value R_w and the Relative Concentrations

The Water Value R_w is defined as the relation of the amount of alkoxy groups to the amount of water.

$$R_w = \frac{RO^-}{H_2O} \quad \text{Eq. 3.1}$$

For $R_w \gg 2$ (little amount of water) condensation reactions dominate hydrolysis reactions.

For $R_w \ll 2$ (big amount of water) hydrolysis reactions dominate condensation reactions.

- The Solvent

The nature of the solvent can influence the state of the equilibrium. When using $\text{Si}(\text{OEt})_4$ and ethanol, for example, the equilibrium state is shifted to the left side of Eq. 3.1. Besides, polarity, dipole moment, viscosity, and the fact if the solvent is protic or not have a strong influence on the development of the materials, as different solvent properties can stabilise different transition states in the system. Thus, the solvent influences the reaction rate.

- The Temperature

Temperature mainly affects the reaction rate.

Gelation

The sol-particles condense, giving macroscopic structures, and a gel is formed. The volume of the system does not change in this step, but viscosity increases, and the liquid present is entrapped.

Ageing

After gelation, there are sol-particles left in the solvent, which is entrapped in the pores of the gel. Thus, inside the pores the sol-particles can further condense and decrease the size of the pores. As a result, the solvent is pressed out of the pores, and the volume of the gel decreases. So, in this sub-step, the volume of the material as well as the volume of the pores, are reduced.

Drying

By removing the solvent without damaging the pores of the material, an aerogel is formed. This can be achieved by extraction with supercritical carbon dioxide, or lyophilising. By simply heating the material, most often the pores are destroyed, yielding a dense xerogel.

Nomenclature

According to which moieties are bound to the silicon atom, a classification is made into Q-, T-, D-, and M-groups (Figure 3.1). Q-groups allow the formation of four siloxane bonds ($\text{Si}-\text{O}-\text{Si}$) and therefore, of three-dimensional network structures. With T-groups three siloxane bonds can be formed, and two-dimensional layer structures are built. D-groups lead to the formation of chains and rings, as only two siloxane bonds can be formed, whereas M-groups

only allow the formation of one siloxane bond and thus, of dimers. Superscript numbers give the number of siloxane bonds (Figure 3.1). ^{29}Si solid state NMR spectroscopy can differentiate between the groups. Reference values for the chemical shifts are -100 ppm for Q-groups, -60 ppm for T-groups, and -20 ppm for D-groups.²⁵

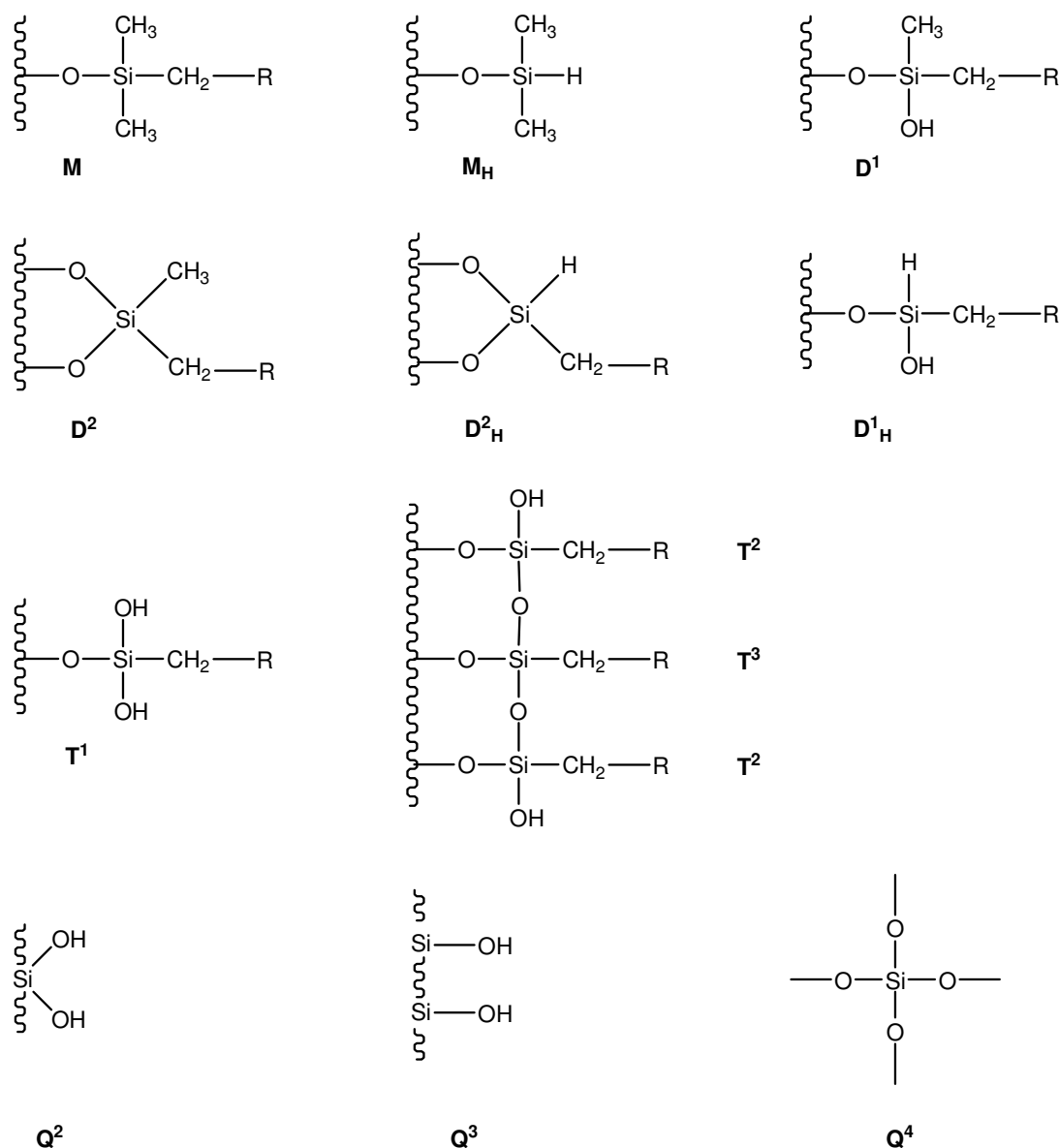


Figure 3.1 Nomenclature of siloxane species.

3.1.2 The Stöber Process

The Stöber Process enables the controlled synthesis of spherical, monodisperse silica nanoparticles with diameters of 50-2000 nm.²⁶ Tetraalkyl siloxanes (methyl-, ethyl-, *n*-propyl,

n-butyl, *n*-pentyl-) as precursors are hydrolysed and condensed in alcohols (methanol, ethanol, *n*-propanol, *n*-butanol) as solvent in the presence of water and ammonia as catalyst. The size of the particles can be controlled by the following parameters.^{27,28}

- The Concentration of Ammonia and Water

With increasing concentrations of ammonia and water, the reaction rate and therefore, the diameter *d* of the particles are increased as well. Yet, a too big amount of water leads to a stagnation of particle growth.

- The Concentration of the Silicate

If the concentration of the precursor silicate exceeds a critical value of about 0.2 mol L⁻¹, the particle diameter *d* decreases, and silica gels are formed.

- The Chain Length of the Solvent and the Alkoxy Moieties at the Silicon

With increasing chain length and degree of branching, *d* is increasing as well.

- The Temperature

The diameter *d* of the particles decreases with increasing temperature.

The silicates do not completely hydrolyse during the Stöber Process, so there are ≡Si-OR moieties left inside and at the surface of the particles, which can be shown by IR and NMR spectroscopy. These alkoxy moieties can be removed by tempering the materials at 600 °C, at which the density of the particles is increased simultaneously.

The spectra of the Stöber particles show an amount of Q⁴-groups of about 60-65 % and an amount of Q³-groups of about 30-35 %.

3.2 Functionalisation of Silicas

3.2.1 Silanisation

The functionalisation of silica gels or silica (nano)particles is well investigated, and various functional groups can be attached to the surface of the silicas. The most common surface modification involves condensation of surface silanol groups with functionalised alkoxy silanes (silanisation).^{25,29-32} In this reaction, one or two siloxane bonds are formed, which are linked to the particle surface, and possibly crosslinking with other coupled silanes occurs. The disadvantage of this method is that these siloxane bonds are prone to hydrolysis in aqueous

medium due to incomplete condensation reactions, and thus, leaching of the coupled silanes can take place.

3.2.2 Hydrosilylation

An alternative approach of surface functionalisation of silica is the formation of Si-C bonds. In contrast to siloxane bonds, Si-C bonds are non polar, stable, and chemically inert.³¹ Hydrosilylation is an important method for the formation of Si-C bonds. In general, organic or inorganic silicon hydrides are added to multiple bonds, in particular to C=C or C=X double bonds (where X = O, N), as well as to heteroatom-heteroatom double bonds (N=N, N=O). Here, the addition of a Si-H bond of a silane on the particle surface to the C=C double bond of an olefin, are considered. Substituted olefins preferentially yield the anti-Markovnikov product, and terminal silyl groups are formed. Hydrosilylation reactions do not run spontaneously, they require activation by catalysts, or by radical initiators. Commonly used Pt based catalysts, like Speier's and Karstedt's catalysts (chloroplatinic acid H_2PtCl_6 and divinyl disiloxanes) lead to metal contaminations on the silica surface. The use of radical initiators, like benzoyl peroxide, or 2,2'-azobis(2-methylpropionitrile) can also lead to impurities on the silica surface, when the organic compounds react with the surface.³³⁻³⁵ Alternative ways to catalyse hydrosilylation reactions are provided by thermal and photochemical initiation, respectively. As there is no need for the use of reagents, impurities on the particle surface can be completely avoided, which is an advantage of those methods. Thus, in the present work, hydrosilylation reactions were photochemically induced.

3.2.3 Photochemical Hydrosilylation

UV radiation enables the formation of Si-C bonds in photochemical hydrosilylation reactions at room temperature, and without the use of further reagents. This method is widely investigated for the functionalisation of Si-H modified silicon surfaces while mechanistic aspects of the reaction are still controversially discussed.³⁶⁻⁴⁰

3.3 Characterisation

3.3.1 Physisorption Isotherms

3.3.1.1 Specific Surface Area

The specific surface area A of (porous) materials can be determined from adsorption isotherms. The measuring principles are based on the adsorption, that is, the adhesion of gases to a solid surface.

If a solid (with the mass m) and a gas (with the pressure p) are enclosed in a vessel (with a known volume V) the gas molecules will be adsorbed to the surface of the solid, which leads to an increase of the mass m and a decrease of the gas pressure p . The amount of gas, adsorbed to the surface, can be determined from the increase in mass or the decrease in gas pressure, respectively. The adsorbed gas is called adsorbate, the solid is the adsorbent in such a system. The adsorbate can be bound to the surface either chemically (chemisorption) or physically (physisorption). In the case of chemisorption, molecules are bound to the surface by a chemical bond (e.g., H_2 to palladium), so they can decompose. Adsorption enthalpies lie within the range of reaction enthalpies (about 200 kJ mol^{-1}). In the case of physisorption (e.g., inert gases at low temperatures), there are van der Waals forces between solid and gas molecules, and adsorption enthalpies lie in the range of about 20 kJ mol^{-1} .

There is a dynamic equilibrium between free and adsorbed gas molecules, and the distribution of the molecules on the material surface depends on the partial pressure of the free gas.

Adsorption is described through isotherms, that is, the amount of adsorbate on the adsorbent as a function of its pressure at a constant temperature. The shape of the isotherm is defined by the characteristics of the adsorbent.^{41,42}

Langmuir Isotherm⁴³

The simplest shape of an adsorption isotherm is obtained under the assumption, that only a monolayer of adsorbate molecules is formed, and that the adsorption enthalpy is independent of the extent of coverage. The Langmuir equation relates the adsorption of gas molecules on a solid surface to the gas pressure of the medium above the solid surface at a constant temperature. At the beginning, surface coverage increases proportional to the pressure and then converges asymptotical on the value of the monomolecular coverage N_m (Figure 3.2).

BET Isotherm⁴⁴

Frequently, particularly in the case of physisorption, adsorption in multiple layers is observed. Due to the formation of multiple layers, the adsorption isotherms show a different shape. At the beginning, the extent of coverage increases proportional to the gas pressure and converges on a limiting value, but then coverage further increases. So there is a point of inflexion in the isotherm (Figure 3.3). Brunauer, Emmett und Teller first developed a model to describe this behavior, so the BET theory was named after their initials.

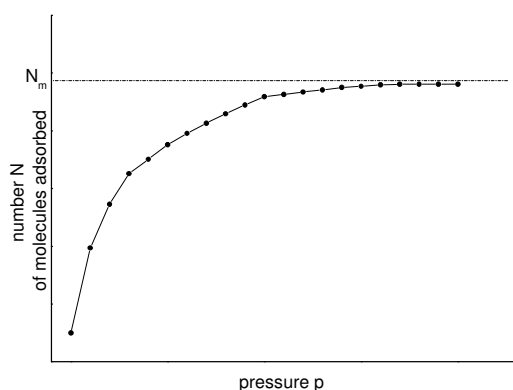


Figure 3.2 Langmuir adsorption isotherm.

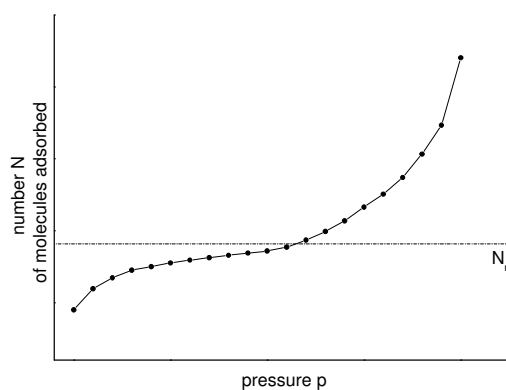


Figure 3.3 BET isotherm for the system N_2 /Stöber particles at 77.35 K.

3.3.1.2 Porosity

Beside the specific surface area, the porosity of materials can also be determined from sorption isotherms, as the pores and the pore size, respectively, influence the shape of the isotherms. Pores of widths < 2 nm are defined as micropores, between 2 - 50 nm as mesopores and > 50 nm as macropores. Six different types of BET-isotherms can be classified. The ideal shape, as depicted in Figure 3.3 (type II), occurs for nonporous solids. If mesopores are present, a hysteresis loop is generated by capillary condensation inside the pores (type IV).⁴⁵

The specific surface area of the particles and pore sizes of the materials in this work were determined by means of BET-measurements. Nitrogen was used as adsorbate on the particle surface and the relative pressure was plotted against the adsorbed volume of nitrogen. In the present system N_2 /Stöber particles physisorption takes place, so van der Waals forces occur between surface and adsorbate.

3.3.2 Dynamic Light Scattering (DLS)

The hydrodynamic diameters of particles in suspension can be determined by measuring their diffusion rate by means of dynamic light scattering (DLS). The diffusion rate depends on the temperature and the viscosity of the liquid and on the size of the particles. With known temperature and viscosity of the liquid, the diffusion rate, and thus the hydrodynamic diameter, of the particles can be determined. The measuring principles are based on Brownian motion and photon correlation spectroscopy (PCS).^{46,47}

Brownian Motion

The random drifting of particles suspended in a liquid is called Brownian motion. The diffusion coefficient of the particles at given temperature and viscosity of the fluid is inversely proportional to the hydrodynamic diameter d_{DLS} . This relation is given by the Stokes-Einstein equation:

$$D = \frac{k_B T}{3\pi\eta d_{DLS}} \quad \text{Eq. 3.2}$$

k_B : Boltzmann constant

T: temperature

η : viscosity of the fluid

d_{DLS} : hydrodynamic diameter

Photon Correlation Spectroscopy (PCS)

The particles suspended are irradiated with a laser, and the scattered light is measured in a photomultiplier tube. The light scattered by the particles generates an interference pattern at any point of time. The detected intensity of light scattered depends on the interference pattern, which itself depends on the particles in the laser beam. As the particles randomly move in the fluid and change their relative positions, the interference pattern persistently changes, and thus, the intensity detected also changes persistently. These fluctuations occur on a time scale of micro- to milliseconds. Big particles move slowly and cause slow fluctuations at the detector, whereas smaller particles move faster and cause quick fluctuations. PCS determines the exact time unit of the fluctuations of the scattered light and hence the particle size.

Autocorrelation Function

To calculate the diffusion coefficient D , the signal has to be transformed mathematically. The result of that transformation is an autocorrelation function (Eq. 3.3), which is related to D by Eq. 3.4:

$$G(\tau) = \langle I(t) \times I(t + \tau) \rangle \quad \text{Eq. 3.3}$$

$G(\tau)$: autocorrelation function

$I(t)$: detected intensity at the time t

$I(t + \tau)$: detected intensity at the time $t + \tau$

τ : delay

$$G(\tau) \propto e^{-2DK^2\tau} \quad \text{Eq. 3.4}$$

D : diffusion coefficient

K : scattering vector (Eq. 3.5)

$$K = \frac{4\pi n}{\lambda} \sin\left(\frac{\Theta}{2}\right) \quad \text{Eq. 3.5}$$

n : refraction index of the fluid

λ : wave length of the laser

Θ : scattering angle

Size Distribution Processor (SDP) Analysis

The SDP analysis provides the size distribution of the particles and its standard deviation from the autocorrelation function.

3.3.3 Diffuse Reflectance Infrared Fourier Transform Spectroscopy (DRIFTS)⁴⁸

Infrared spectroscopy is mostly measured in transmission, but surfaces or strongly scattering samples can only be measured in reflection with a special setup.

In diffuse reflectance experiments, powdery samples can be directly measured, which simplifies the sample preparation. Absorption, refraction and reflexion take place simultaneously at the sample's surface. In the present work, samples were mixed with KBr to reduce absorption by the silica particles. This method is particularly suitable for the characterisation of surfaces.

3.3.4 Scanning Electron Microscopy (SEM)

The topography of surfaces can be depicted by means of scanning electron microscopy (SEM). Therefore, an electron beam is generated by an electron-optical system of electromagnetic and electrostatic refractors, and the surface of an object is examined by line-by-line scanning with the electron beam. Acceleration voltages of 5 - 30 kV are applied. Images can be generated by detecting the secondary electrons emitted by the object (SE image) or by detecting backscattered electrons (BSE image). Secondary electrons possess kinetic energies of < 50 eV, backscattered electrons of > 50 eV. A combination of a scintillator and a photomultiplier serves as detector and is positioned angular above the sample, which lets the object appear three-dimensional. Samples should be conducting, if they are not, they can be made conducting by thin-film deposition (sputtering) of a metal (e.g., Au, Pd, Pt). For SE images, as taken in this work, a resolution limit of 2 - 20 nm can be reached.^{49,50}

3.4 Magnetic Resonance Imaging (MRI)

Magnetic resonance imaging (MRI) is an imaging technique widely used in clinical diagnosis to image the soft tissues inside the human body. The measuring principles are based on nuclear magnetic resonance (NMR) spectroscopy and the ^1H NMR signals of the water protons in the body are detected. To obtain images from the NMR measurements, the ^1H NMR signals have to be depicted location-dependent. This is enabled by the application of time-dependent, linear magnetic field gradients along the three directions in space, which change the magnetic field strength G at a location $(x|y|z)$ linearly with the time t (Eq. 3.6; given only for x-direction):

$$B(x, t) = B_0 + G_x(t)x \quad \text{Eq. 3.6}$$

B_0 : external magnetic field

x : spatial coordinate in x-direction

$G_x(t)$: gradient strength

Thus, the resulting Larmor frequency ω depends on the location r and the time t (Eq. 3.7):

$$\omega(r, t) = -\gamma B(r, t) \quad \text{Eq. 3.7}$$

r : location in space $r = (x|y|z)$

γ : gyromagnetic ratio

As the resonance frequency of the water protons depends on the magnetic field strength, the frequency also is location-dependent and it is possible to excite only protons at a certain location in the body. The application of the field strength gradients enables the assignment of the signal intensity to a definite spatial volume element (voxel).

The signal intensity mainly depends on three factors, which depend on their chemical environment: the spin density ρ , the longitudinal relaxation time T_1 , and the transverse relaxation time T_2 . By the application of different pulse sequences, it is possible to create a dependency of the signal intensities on ρ , T_1 , or T_2 . The final MR image is created by converting the signal intensity of each voxel into the brightness of a grey-level value.¹

3.4.1 MRI Contrast Agents

Contrast agents influence the signal intensity of the protons in the surrounding tissue by shortening the longitudinal and/or the transverse relaxation time, T_1 and T_2 , respectively. Paramagnetic compounds with unpaired electron spins can shorten the relaxation times significantly and therefore, are used as contrast agents for MRI. In T_1 -weighted images, a shorter T_1 leads to a signal enhancement in terms of an increase in brightness. Shortening of T_2 in T_2 -weighted images leads to a decrease in brightness, which is not as well detectable. Therefore, T_1 agents are mostly preferable. An effective contrast agent should possess as many unpaired electrons as possible, and its electron spin relaxation time must correlate well with the Larmor frequency of the influenced protons. Fe^{3+} , Mn^{2+} , and Gd^{3+} ions fulfill these conditions at best.^{1,3}

Currently applied T_2 agents typically are iron oxide (Fe_3O_4) nanoparticles, whereas most T_1 agents are based on gadolinium complexes. Gd(III) possesses seven unpaired electrons and a good electron spin relaxation rate, so it has a strong influence on the longitudinal relaxation time of the water protons. Besides, the exchange rate of water molecules in the gadolinium aqua complex is quite high, which leads to a strong influence of the surrounding bulk water molecules. The major drawback of gadolinium based CAs is the toxicity of the free Gd(III) ion to the human body. Due to its ionic radius, which is close to that of Ca(II) , calcium regulated processes within the body are disturbed. Thus, chelating ligands are used to form stable and inert complexes, which can be applied as CAs.⁵¹⁻⁵³

To diminish the dissociation of the Gd(III) complexes in the body, multidentate ligands are used, where not all coordination sites may be occupied, to allow interactions of the Gd(III) ion with water molecules. The relaxation rate observed under the influence of paramagnetic compounds ($1/T_{1,2o}$) consists of a diamagnetic ($1/T_{1,2d}$) and a paramagnetic ($1/T_{1,2p}$) term (Eq. 3.8):

$$\frac{1}{T_{1,2o}} = \frac{1}{T_{1,2d}} + \frac{1}{T_{1,2p}} \quad \text{Eq. 3.8}$$

The paramagnetic term is proportional to the concentration of the paramagnetic compound, for example Gd^{3+} ($[\text{Gd}]$) and is given in mmol L^{-1} :

$$\frac{1}{T_{1,2o}} = \frac{1}{T_{1,2d}} + r_{1,2} \cdot [\text{Gd}] \quad \text{Eq. 3.9}$$

The relaxivity $r_{1,2}$ [$\text{mM}^{-1} \text{s}^{-1}$] is a direct measure for the efficiency of a complex as contrast agent. The origin for the enhancement of the relaxation rates by paramagnetic compounds can be classified into three different contributions: relaxation in the inner sphere (water molecules coordinated to the metal), the second sphere (water molecules bound to the ligand) and the outer sphere (bulk water molecules) (Figure 3.4). The contribution of the inner sphere is based on the interactions of the electron spins of the Gd^{3+} ion with the protons of the coordinated water molecules. By the exchange of the inner sphere water molecules with bulk water molecules this contribution is transferred into the bulk volume. Water molecules diffusing around the complex also are influenced by the paramagnetism resulting in the relaxation in the outer sphere. These contributions are additive and the share of the inner sphere effect is about 60%, the share of the second and outer sphere effect about 40%.¹⁻⁴

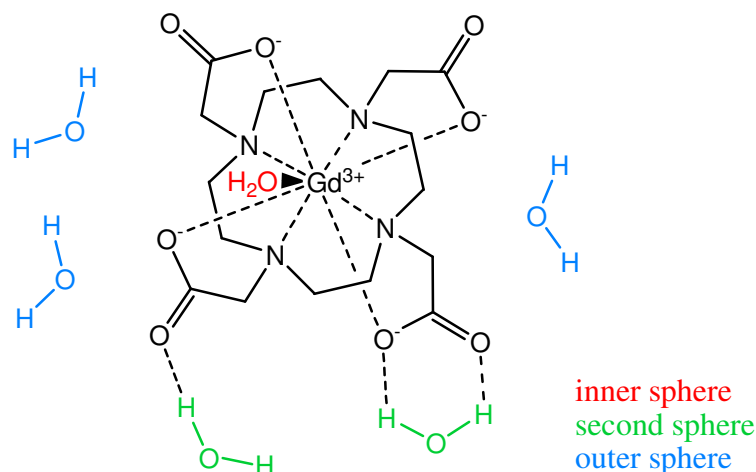


Figure 3.4 Interactions of water molecules with Gd(III) based contrast agents.

3.5 Nanoparticulate Contrast Agents

Since molecular agents are released easily and quite fast from the body, they are not suitable for long-term tracking applications.⁶

Therefore, nano-sized materials are developed and are gaining increased importance in medical diagnosis and treatments. By tailoring hybrid nanomaterials, consisting of an inorganic matrix and functional organic moieties, materials with special properties can be made for various purposes, such as carriers of drugs or for imaging techniques.⁷⁻¹² Combined with targeting units, they promise to identify diseases on a molecular level and thus, in an early stage.¹³⁻¹⁷ Most of the currently used nanoparticulate CAs are T₂ agents based on iron oxide NPs.⁵⁴ In spite of many applications, T₂ agents have several disadvantages. They are negative imaging agents, which result in signal decreases. Moreover, their high susceptibility induces distortions of the magnetic field on nearby tissues. This leads to a loss of contrast between lesions and background.⁵⁵⁻⁵⁷ Nanoparticulate silica based matrices, functionalised with gadolinium chelates, which serve as T₁ agents are rare.^{13,14,17-20} Silica particles bring several advantages. In a minimum of space, large payloads of CA molecules can be obtained. Thus, because of the high local concentration of CA molecules, nano-sized materials can act as contrast amplifiers and result in an overall high relaxivity, as well as improved resolution and sensitivity. Furthermore, they can serve as matrices not only for CA molecules, but also for targeting or 'smart' units, which respond to physiological changes (e.g. in pH or ion concentrations), as well as fluorophores and biocompatible moieties, such as polyethylene glycol (PEG).^{13,14,17,21} Nonporous nanoparticles ensure that the molecules are only bound to the surface. In the case of gadolinium chelate based CAs, this allows unhindered interactions of water with all gadolinium sites, which is mandatory for a good contrast. Another advantage of immobilising CA molecules on NPs is a decreased rotational tumbling. According to the Solomon-Bloembergen-Morgan theory of paramagnetic relaxivity a higher rotational correlation time τ_R leads to an enhancement in relaxivity.^{3,58}

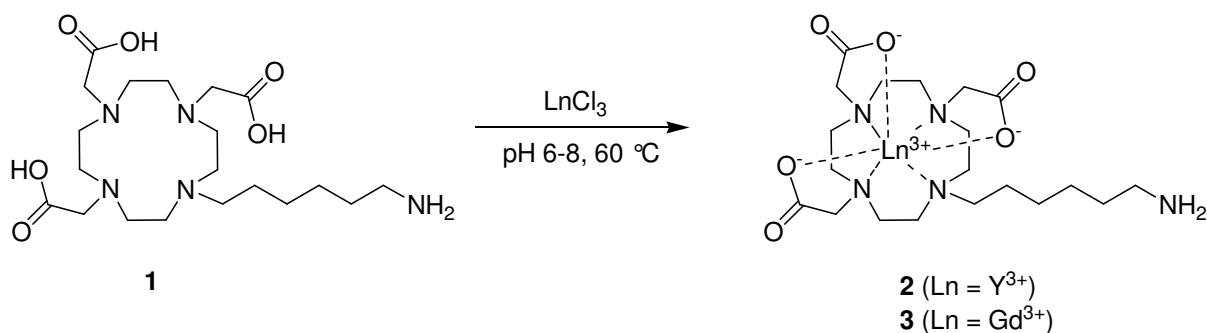
4 Results and Discussion

4.1 Syntheses of LnDOTA- and LnDO3A-Derivatives

To couple DOTA- and DO3A-like gadolinium chelate complexes to a matrix, an additional functional group is required, which allows coupling of the Gd(III) complex to the surface of the matrix. In this work, this is realised by the introduction of carboxylic acid and amino groups, respectively, thus allowing to build peptide bonds between complexes and matrix.

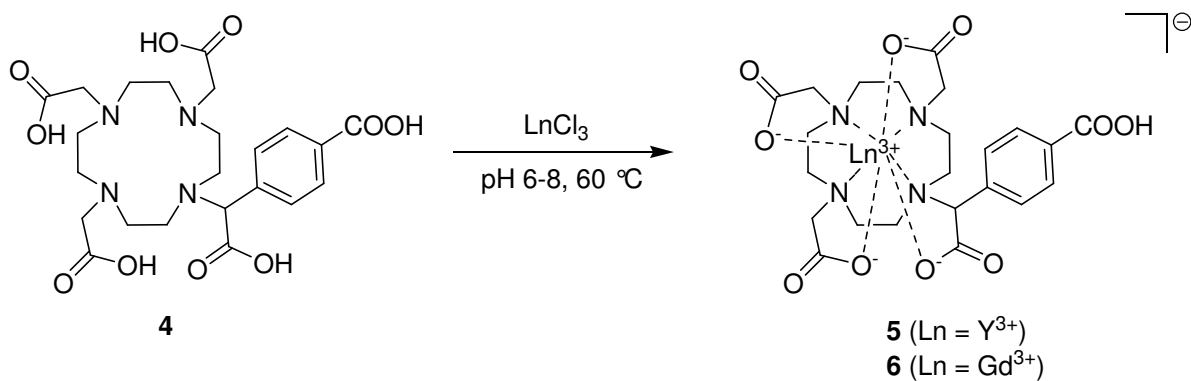
Next to Gd³⁺ derivatives, which serve as CAs, the Y³⁺ analogues were synthesised to enable NMR spectroscopic investigations. In the following, the expression ‘lanthanides’ and the abbreviation ‘Ln’ are used with respect to Gd and Y.

To couple Ln(III) complexes to carboxylic acid functionalised matrices, the amino-terminated DO3A-hexylamine ligand **1**⁵⁹ was used and loaded with Y³⁺ and Gd³⁺, to give complex **2** and **3**, respectively (Scheme 4.1).

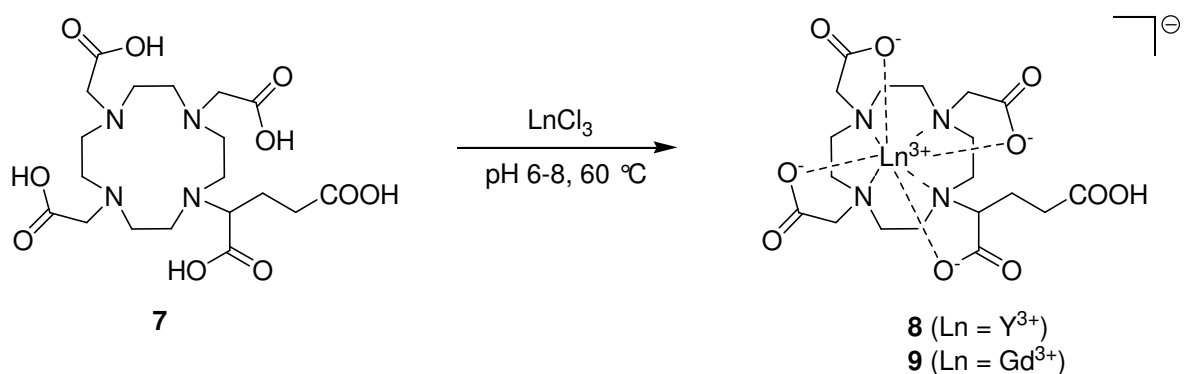


Scheme 4.1 Syntheses of Ln[DO3A-hexylamine] derivatives.

For coupling Ln(III) complexes to amino-terminated matrices, the carboxylic acid functionalised DOTA-derivatives DOTA-BA **4** and DOTA-GA **7** were synthesised according to ref. 60 and loaded with Y³⁺ and Gd³⁺, respectively, to give the Ln[DOTA-BA] complexes **5** and **6** (Scheme 4.2) as well as the Ln[DOTA-GA] complexes **8** and **9** (Scheme 4.3). As the DOTA derivatives are charged complexes, the tetrabutyl ammonium ion (*n*-Bu₄N⁺) was introduced as counterion to improve the solubility of the complexes in DMSO.

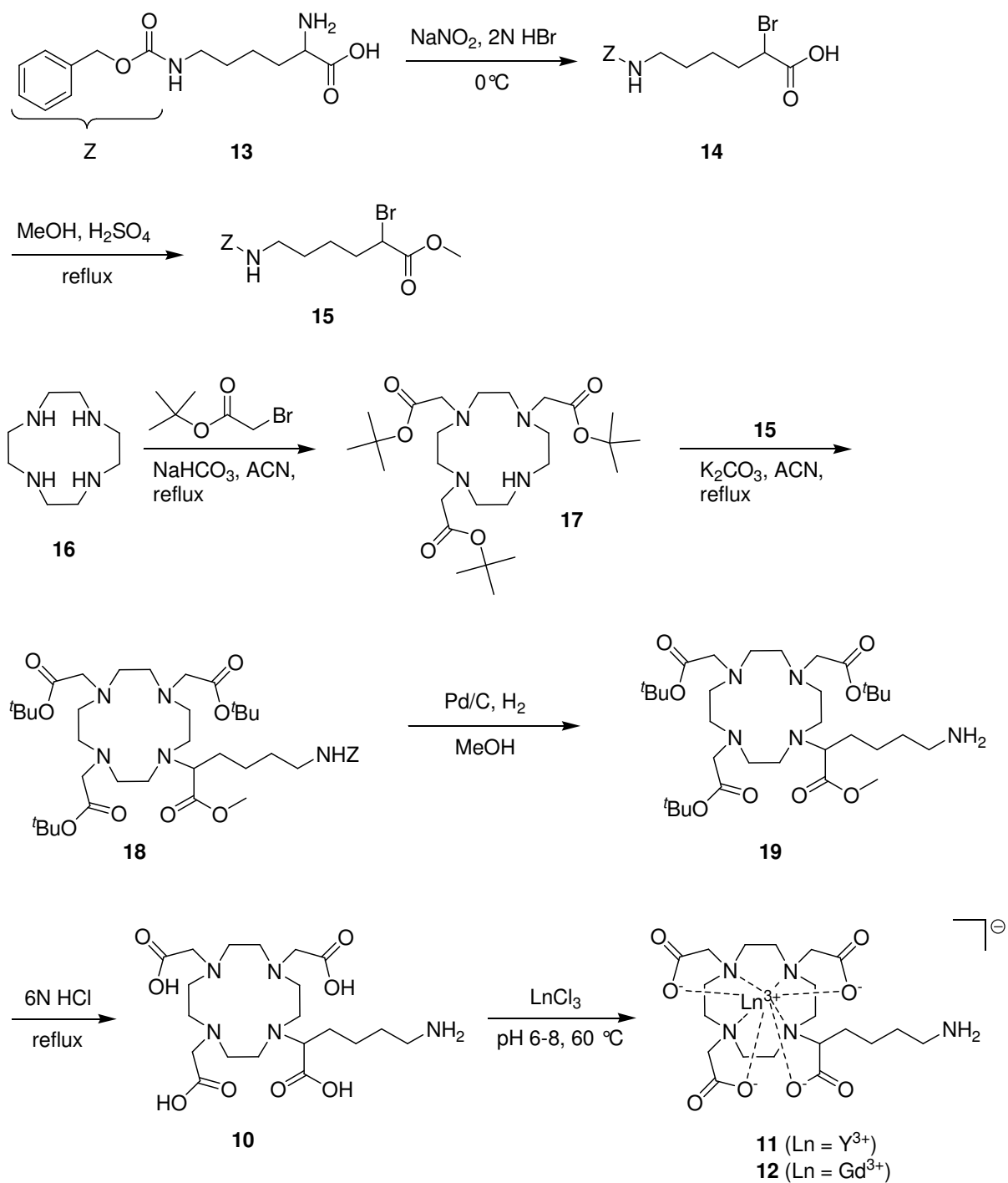


Scheme 4.2 Syntheses of Ln[DOTA-BA] derivatives.



Scheme 4.3 Syntheses of Ln[DOTA-GA] derivatives.

Finally another amino-terminated DOTA-compound, DOTA-ButAm⁶¹ **10** was synthesised to allow coupling of the Ln(III) complexes **11** and **12** to carboxylic acid groups. Therefore, a new route for the synthesis of **10** was developed (Scheme 4.4). In the first step N_ω-Z-L-lysine (**13**) was brominated with hydrobromic acid and sodium nitrite. The carboxylic acid group of the resulting bromolysine (**14**) was protected with a methyl group under acidic conditions. The resulting lysine derivative **15** was reacted with DO3A(^tBu)₃ (**17**) in a nucleophilic substitution reaction in acetonitrile with potassium carbonate to give the protected DOTA like ligand **18**. The Z protecting group was removed by hydrogenolysis under Pd/C catalysis. Finally, the acid protecting groups were removed by refluxing compound **19** in 6 N hydrochloric acid to give DOTA-ButAm **10** (Scheme 4.4). The complex **11** was synthesised with Na⁺ as counterion. The compounds were characterised by ¹H and ¹³C{¹H} NMR spectroscopy and mass spectrometry.



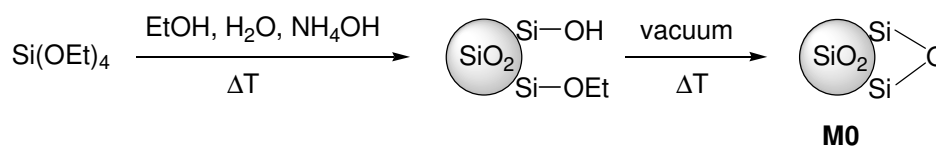
Scheme 4.4 Synthesis of Ln[DOTA-ButAm].

4.2 Syntheses and Characterisation of Stöber Particles

Stöber silica particles are generally described as nonporous and monodisperse spheres with diameters in the colloidal range.²⁶ In previous work,⁶²⁻⁶⁴ the synthesis of Stöber silica particles was optimised to obtain materials as close as possible to ideality with respect to nonporosity, monodispersity and spherical shape, while controlling the particle diameter. Furthermore, as an additional criterion, the particles have to be isolated from their suspensions without structural degradation, such as aggregation, since chemical modifications are performed after the synthesis. The materials are thoroughly characterised to precisely define any deviation from ideality and to carefully determine the extent of surface modifications. The characterisation includes surface chemical properties, which are important for reactions to immobilise molecules on the surface.

4.2.1 Synthesis of Stöber Particles

The formation of Stöber particles relies on a balance between the relative rates of the condensation and hydrolysis reactions. The experimental parameters (concentrations, temperature, chemical identity of the precursor, catalyst, and solvent) define the extent and rate of each step, and therefore, the final particle properties, like shape, size, size distribution and porosity. As there are various parameters controlling the final particle size (temperature, type of solvent, concentrations of TEOS, water and ammonia), and as some parameters influence both, the reaction kinetics and the colloidal stability (thermodynamic effects), it is difficult to predict the final particle size that will result from a given set of experimental conditions.



Scheme 4.5 Synthesis of bare Stöber particles **M0**.

The aim of this work was the synthesis of nonporous particles with a diameter of 100 and 50 nm, respectively. Therefore, based on previous work,⁶²⁻⁶⁴ different concentrations of the starting compounds and a variation of the reaction temperature were used in this work. The reaction conditions are listed in Table 4.1. A mixture of ethanol and water was heated to the desired reaction temperature. After the temperature of the mixture was equilibrated for at least 15 min, aqueous ammonia and TEOS were quickly added under strong stirring. After 2 h

under continued strong stirring, the resulting particles **M0** were separated by centrifugation and washed with water and ethanol using ultrasonication and centrifugation after each step. The materials were dried *in vacuo* at 100 °C for at least 15 h (Scheme 4.5).

Independent of the degree of hydrolysis, mesopores are absent in materials resulting from the Stöber process. However, the silica particles are not fully condensed and contain micropores.²⁷ Therefore, the materials (except **M0₅₀** and **M0b₁₀₀**) were calcinated at 600 °C *in vacuo* for at least 15 h in order to further reduce the microporosity. **M0₅₀** was not calcinated to avoid aggregation, which is likely for particles with small diameters. Calcination is expected to condense the internal silanol groups into siloxane bonds yielding a more condensed matrix (Scheme 4.5, 2nd reaction step). The thermal treatment also induces the loss of surface silanol groups and is expected to eliminate any remaining solvent and ammonia molecules from the silica matrix.^{65,66}

Table 4.1 Reaction conditions for the syntheses of **M0** materials.

material	reaction conditions				
	V(EtOH) / mL	V(TEOS) / mL	V(NH ₄ OH) / mL	V(H ₂ O) / mL	T / °C
M0₁₃₀	400	30	20	72	75
M0a₁₀₀	400	30	20	72	75
M0b₁₀₀	100	7.50	5	18	75
M0₅₀	300	11.00	7.57	-	35

subscript numbers are average diameters
(**M0b** only dried at 100 °C, **M0a** calcinated at 600 °C)

4.2.2 Characterisation of Stöber Particles

4.2.2.1 Size and Shape

Size. The size of the Stöber particles was determined by evaluation of images, obtained by scanning electron microscopy (SEM) and by dynamic light scattering (DLS) measurements. The results are given in Table 4.2. Silica nanoparticles with diameters of about 50, 100 and 130 nm were obtained.

The average diameters d_{SEM} from SEM were determined by sizing a number n of particles from each batch in the scanning electron micrographs. Beside diameters and standard deviations σ of the particles, the statistical analysis also provides information about the size

distribution. The size distributions of the **M0** materials closely follow Gaussian distributions. The evaluation of the Gaussian curves, fitted to the size distributions, results similar values for $d_{SEM} \pm \sigma$. Differences lie within the range of the standard deviations.

The hydrodynamic diameters d_{DLS} of the particles in dilute suspensions were determined from measurements of their diffusion coefficients by DLS in water. The diameters and the polydispersity indices (PDI) of the DLS measurements are listed in Table 4.2. The diameters correlate well with those obtained from the scanning electron micrographs. This demonstrates that the particles exist as single units suspended in water. The diameter of **M0₅₀** could not be determined by DLS owing to strong agglomeration phenomena. As DLS determines the hydrodynamic diameter d_{DLS} of suspended particles, diameters measured by this technique are bigger than those determined from SEM images.

In previous work⁶²⁻⁶⁴ it was shown, that the Stöber process yields reproducible diameters, if the reaction conditions are controlled carefully. However, small changes in the experimental conditions, including unintentional variations, can have dramatic effects on the particle diameter. The conditions for **M0₁₀₀** and for **M0₁₃₀** were the same, but the particles were synthesised from a different batch of TEOS, which might be the reason for the difference in the particle diameter.

Table 4.2 Size characterisation of the **M0** materials.

material	d_{DLS} / nm	PDI	d_{SEM} / nm
M0₁₃₀	164 ± 64	0.441	131 ± 11
M0a₁₀₀	118 ± 66	0.247	103 ± 10
M0b₁₀₀	127 ± 37	0.143	110 ± 9
M0₅₀	-	-	51 ± 5

subscript numbers are average diameters
(**M0b** only dried at 100 °C, **M0a** calcinated at 600 °C)

Shape. Beside the size of the particles, SEM-images show the shape and behaviour of the particles. Bigger particles form perfect spheres, whereas the smaller 50 nm particles show deviations from a perfect spherical shape (Figure 4.1). Bare particles **M0** do not agglomerate and arrange in close-packing of spheres.

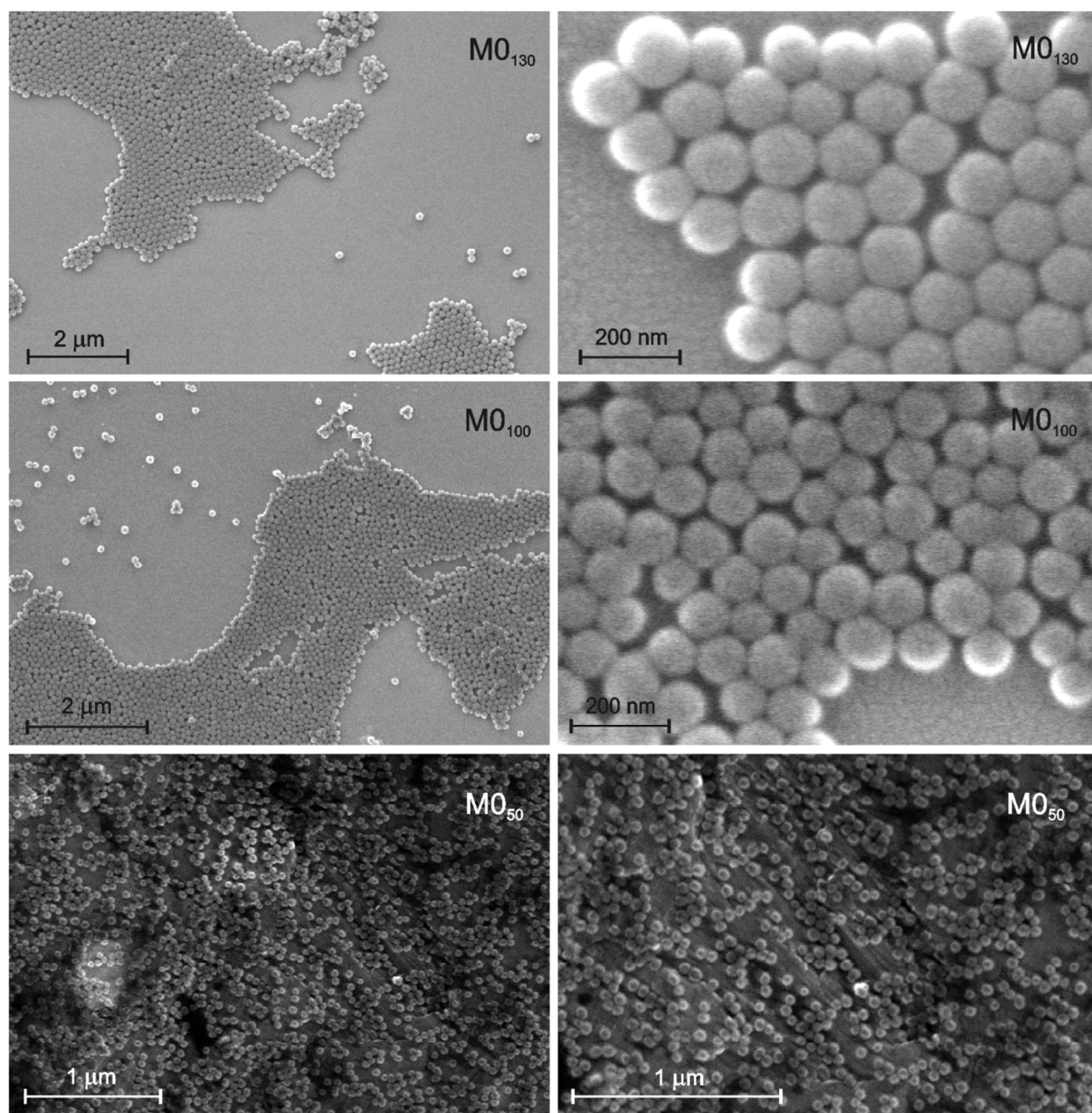


Figure 4.1 Scanning electron micrographs of MO_{130} , MO_{100} , and MO_{50} .

4.2.2.2 Spectroscopic Investigations

On the surface of silica particles, there are different species of OH groups. Next to free isolated silanol groups $\equiv\text{Si-OH}$ (Figure 4.2 a), hydrogen bonded silanol groups (Figure 4.2 b) and surface siloxane groups $\equiv\text{Si-O-Si}\equiv$ (Figure 4.2 c) are present. Subject to the temperature pretreatment of the material, different amounts of adsorbed water can be observed on the surface (Figure 4.2 d, grey).⁶⁵ Depending on the synthesis based on TEOS, there are also a few $\equiv\text{Si-O-Et}$ groups left on the surface.

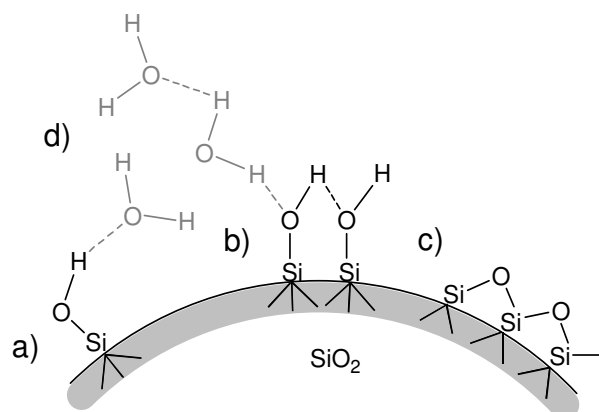


Figure 4.2 Model of the silica surface: a) isolated silanol groups, b) hydrogen bonded silanol groups, c) siloxane groups, d) adsorbed water molecules.

Surface chemical properties of the Stöber particles were examined by diffuse reflectance (DRIFT) IR-FT spectroscopy and ²⁹Si HPDEC/MAS NMR spectroscopy.

DRIFT Spectroscopy. The DRIFT spectra of the bare particles **M0** (Figure 4.3) show the vibrations of free, isolated silanol groups (ν_{SiOH}) at 3746 cm^{-1} , different hydrogen bonded -OH groups (ν_{OH}) from 3732 to 3012 cm^{-1} and surface bound water at 1630 cm^{-1} , as well as vibrations of the interior siloxane bonds ($\nu_{\text{Si-O-Si}}$) at 1980 , 1866 , and 1362 to 1003 cm^{-1} . Vibrations of CH_x groups (ν_{CH_x}) are very weak at 2985 and 2904 cm^{-1} and belong to residual Si-OEt moieties. After calcination of the particles at $600\text{ }^\circ\text{C}$, the vibrations of the CH_x and -OH groups disappear. Another indication of the change in the particle structure by calcination is the disappearance of the stretching vibration of Si-OH groups at 945 cm^{-1} .²³

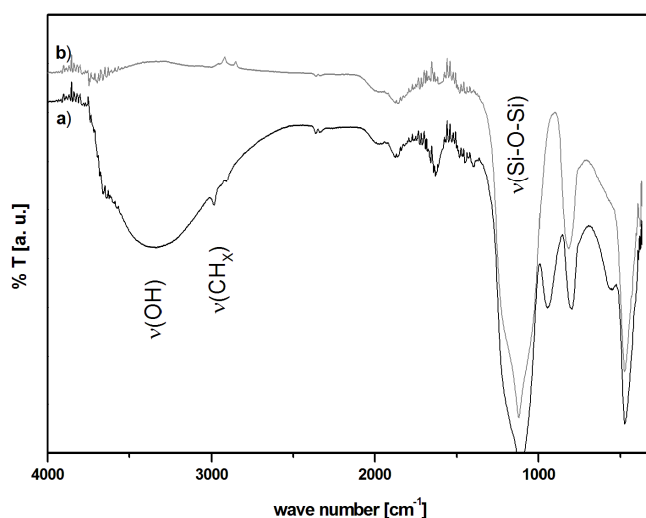


Figure 4.3 DRIFT spectra of **M0**₁₀₀. a) dried at 100 °C and b) calcinated at 600 °C.

Table 4.3 Assignments of IR vibrations of **M0**₁₀₀.

wave number / cm ⁻¹		assignment
M0b	M0a	
3746		isolated ν(Si-OH)
3732 - 3012		different ν (OH)
2985, 2904		ν (CH _x)
1980, 1866	1980, 1866	ν (Si-O-Si)
1630		H ₂ O
1362 - 1003	1380 - 908	ν _{as} (Si-O-Si) (skeleton)
945		ν (Si-OH)
798	818	} δ (O-Si-OH), ν _s (Si-O-Si), δ (O-Si-O)
555		
478	478	

(**M0b** only dried at 100 °C, **M0a** calcinated at 600 °C)

Solid state NMR spectroscopy. By ²⁹Si solid state NMR spectroscopy the nature of the silicon nuclei of the particles can be investigated. Corresponding to the DRIFT data, the ²⁹Si HPDEC/MAS NMR spectrum of **M0**, dried at 100 °C, shows signals of Q³ groups at -103 ppm (33%) and Q⁴ groups at -110 ppm (67%). After tempering **M0** at 600 °C, in the ²⁹Si

NMR spectrum only a broad signal for Q⁴ groups is left at -109 ppm, as residual Si-OEt and Si-OH groups condense, due to the high temperature treatment.

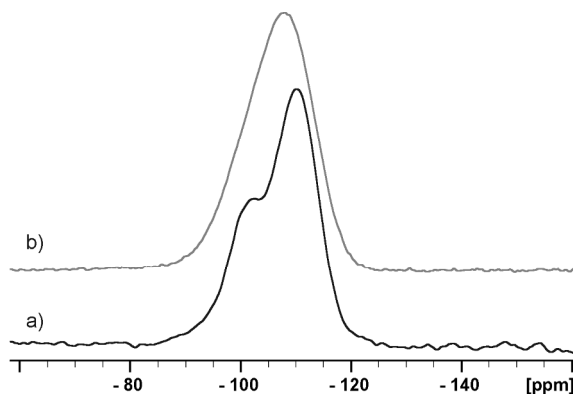


Figure 4.4 ²⁹Si HPDEC/MAS NMR spectra of **M0₁₀₀**. a) dried at 100 °C and b) calcinated at 600 °C.

4.2.2.3 Specific Surface Area and Porosity of the Stöber Particles

Specific surface areas A_{BET} and pore sizes d_{p} of the particles were determined from nitrogen sorption isotherms by means of the Brunauer-Emmett-Teller (BET) model, which applies to type II and type IV isotherms and determines the specific surface area including the surface area of micropores.^{44,66} The values are given in Table 4.4. The BET isotherms of the Stöber particles (Figure 4.5) show hysteresis loops, which is an indication for mesoporous materials. The extent of the hysteresis increases with decreasing particle diameter. Besides, pores with diameters of 13.4 to 27.2 nm are detected by the BET method. In fact, the mesopores determined, are the interstices between the single particles. When the particles get smaller, the interstices between single particles decrease as well, while the specific surface area A_{BET} increases significantly.

Table 4.4 Specific surface area and porosity of the Stöber particles.

material	$A_{\text{BET}} / \text{m}^2 \cdot \text{g}^{-1}$	d_{p} / nm
M0₁₃₀	30	27.2
M0a₁₀₀	43	25.2
M0b₁₀₀	49	24.5
M0₅₀	104	13.4

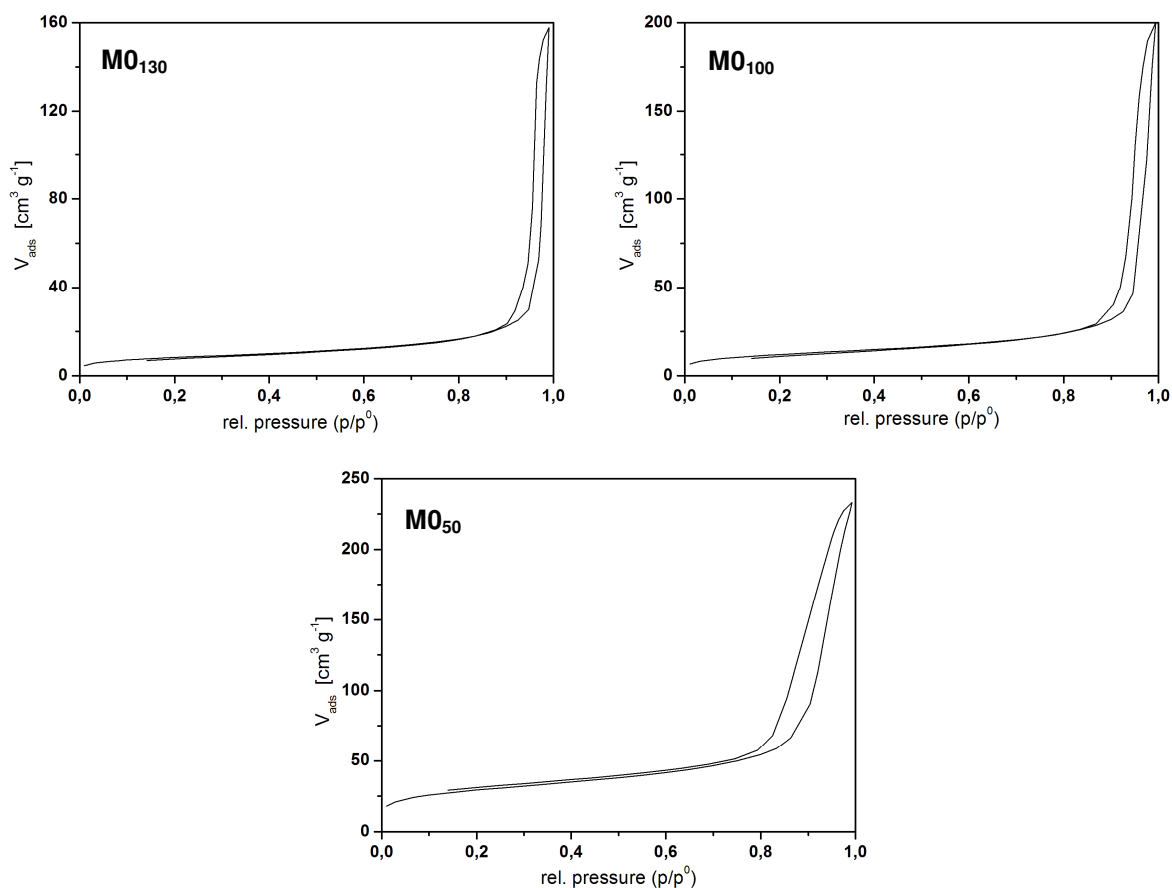


Figure 4.5 Nitrogen Sorption isotherms for **MO₁₃₀**, **MO₁₀₀**, and **MO₅₀**.

4.2.2.4 Specific Surface Concentration of $\equiv\text{Si-OH}$ Groups

According to the Zhuravlev model, which describes the surface chemistry of amorphous silica and determines the number of silanol groups α_{OH} on the surface, an average value of $\alpha_{\text{OH}} = 4.9$ OH nm⁻² (8.14 $\mu\text{mol m}^{-2}$) has been reported.⁶⁵ As the specific surface area of the particles is known, the number of silanol groups $\Gamma_{\text{Si-OH}}$ on the surface of the NPs can be estimated.

Table 4.5 Specific surface concentration of silanol groups.

material	$A_{\text{BET}} / \text{m}^2 \text{g}^{-1}$	$\Gamma_{\text{Si-OH}} / \mu\text{mol g}^{-1}$
MO₁₃₀	30	242
MOa₁₀₀	43	352
MOb₁₀₀	49	397
MO₅₀	104	849

Correlating with A_{BET} , the amount of Si-OH groups per gram on the particles' surface increases with decreasing particle diameter. While **M0**₁₃₀ contains 242 μmol silanol groups per gram, **M0**₅₀ already contains 849 μmol (Table 4.5.). These findings correlate well with geometrical considerations regarding volume and surface of a sphere.

4.3 Surface Modification of Stöber Particles

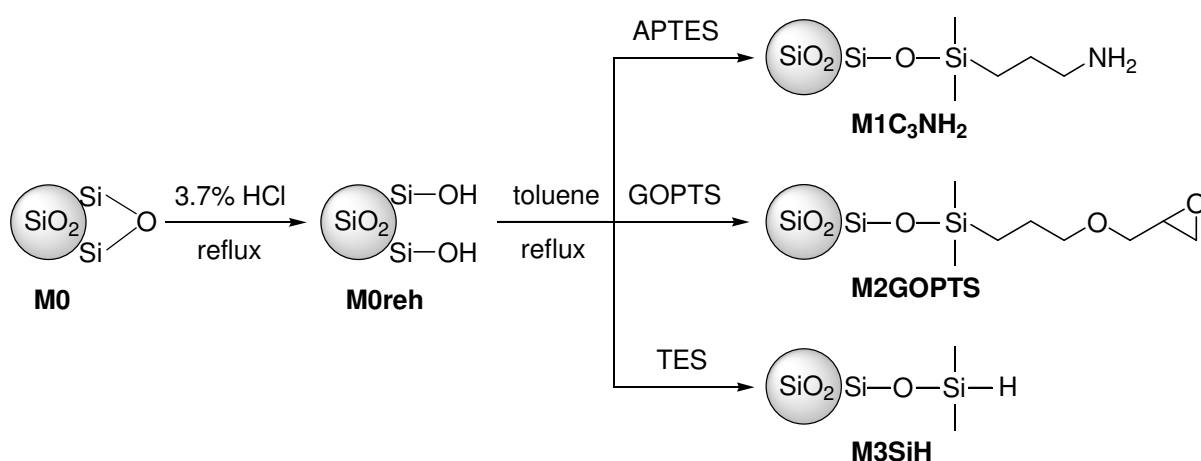
The characteristics of Stöber particles make them advantageous as solid and inert matrices for the immobilisation of molecules. Immobilisation of molecules on Stöber particles provides a unique core/shell system: all active centers (shell) are located within an almost identical environment owing to the high symmetry of the particle matrix (core). Although the possible loading of the surface is inferior to that of highly porous materials, such as used for example in chromatographic applications,⁶⁷ the binding sites are expected to be much more homogeneously distributed. This ensures homogenous interactions of water molecules with coupled CA complexes. Moreover, the absence of pores facilitates the diffusion of substrate (water) molecules to the active centers (CAs). Improved accessibility of active centers is expected, especially for large molecules.

To couple Gd(III) complexes and further moieties to the particles' surface, the introduction of functional groups on the surface is mandatory. Functionalisation of silica materials is well investigated and various functional organic groups can be attached to the surface of the silicas.^{25,29,30} By conventional organic coupling reactions, gadolinium complexes – or any desired moiety – can then be coupled to the surface functionalised silica matrices.⁶⁸⁻⁷⁰ The most common surface modification involves condensation of surface silanol groups with functionalised alkoxy silanes (silanisation). The disadvantage of this method is, that the siloxane bonds, formed that way, are prone to hydrolysis in aqueous medium due to incomplete condensation reactions. An alternative approach of surface functionalisation of silica is via chlorination-reduction. Here the surface silanol groups are converted into Si-H functions prior to further functionalisation.⁶⁷ A hydrosilylation reaction with carbon-carbon double bonds then produces Si-C linkage with good stability under a wide range of conditions.

The bare silica NPs **M0** were functionalised with amino groups, epoxy groups, and Si-H groups, respectively, to allow further functionalisation. The materials were fully characterised to precisely determine the extent of surface modifications.

4.3.1 Silanisation

Prior to silanisation, the surface of the calcinated silica particles was rehydroxylated to regenerate surface silanol groups, which can condense with functionalised alkoxy silanes to get a monolayer of coverage.^{65,71} The Stöber particles **M0**₁₃₀ were coated with (3-aminopropyl)triethoxysilane (APTES) and (3-glycidyloxypropyl)trimethoxysilane (GOPTS), giving the materials **M1C₃NH₂** and **M2GOPTS**, respectively. **M0**₁₀₀ and **M0**₅₀ were coated with triethoxysilane (TES), yielding **M3**₁₀₀**SiH** and **M3**₅₀**SiH** (Scheme 4.6).

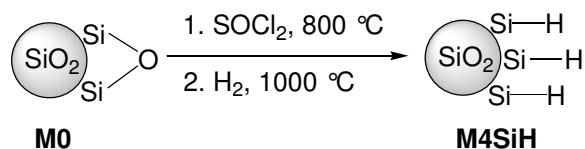


Scheme 4.6 Silanisation of Stöber Particles with APTES, GOPTS, and TES.

4.3.2 Chlorination-Reduction

In silanisation reactions, functionalised alkoxy silanes react with surface silanol groups, forming mainly one or two siloxane (Si-O-Si) bonds, while the binding of the silane via three siloxane bonds is rare. Under certain conditions (high or low pH), these siloxane bonds can be easily broken, which leads to leaching of the silanes from the surface.³¹ Therefore, another approach, a chlorination-reduction sequence, giving **M4SiH**, was used to generate Si-H functionalised materials from **M0a**₁₀₀ (Scheme 4.7).⁶⁷ This reaction requires high temperatures, but the advantage of the chlorination-reduction sequence is the formation of Si-H bonds with silicon atoms, which are embedded in the SiO₂ matrix by two to three siloxane bonds. Leaching processes are strongly reduced in this case.

After drying the particles for 6 h at 800 °C *in vacuo*, they were first reacted with thionylchloride at 800 °C to form Si-Cl bonds on the surface. Then the Si-Cl bonds were converted into Si-H bonds by treating the material with hydrogen at 1000 °C.⁶⁷



Scheme 4.7 Chlorination Reduction of Stöber Particles.

Comparable to the calcination step at 600 °C, after this reaction the mass of the particles as well as average diameters (compare 4.3.3.3 and 4.3.3.4) and the specific surface area (compare 4.3.3.5) are reduced due to the high temperature treatment.⁶²

4.3.3 Characterisation of Surface Modified Stöber Particles

4.3.3.1 Size and Shape

The diameters d_{SEM} of the surface functionalised materials determined from scanning electron micrographs do not differ significantly from those of the starting materials (compare Table 4.2 and Table 4.6). The shape of all surface modified materials does not differ from that of the starting material, either (Figure 4.6). Thus, it is assumed that only monolayers of coverage have been achieved by silanisation and that the high temperature treatment of the chlorination-reduction sequence did not disintegrate the spherical particles.

Table 4.6 Size characterisation of surface modified materials.

material	$d_{\text{DLS}} / \text{nm}$	PDI	$d_{\text{SEM}} / \text{nm}$
M1C₃NH₂	258 ± 98	0.362	131 ± 13
M2GOPTS	140 ± 46	0.195	137 ± 20
M3a₁₀₀SiH	131 ± 33	0.312	104 ± 10
M3b₁₀₀SiH	132 ± 20	0.071	116 ± 14
M3₅₀SiH	-	-	54 ± 5
M4SiH	125 ± 35	0.186	111 ± 10

subscript numbers are average diameters

(**M3a₁₀₀SiH** made of **M0a**, **M3b₁₀₀SiH** made of **M0b**)

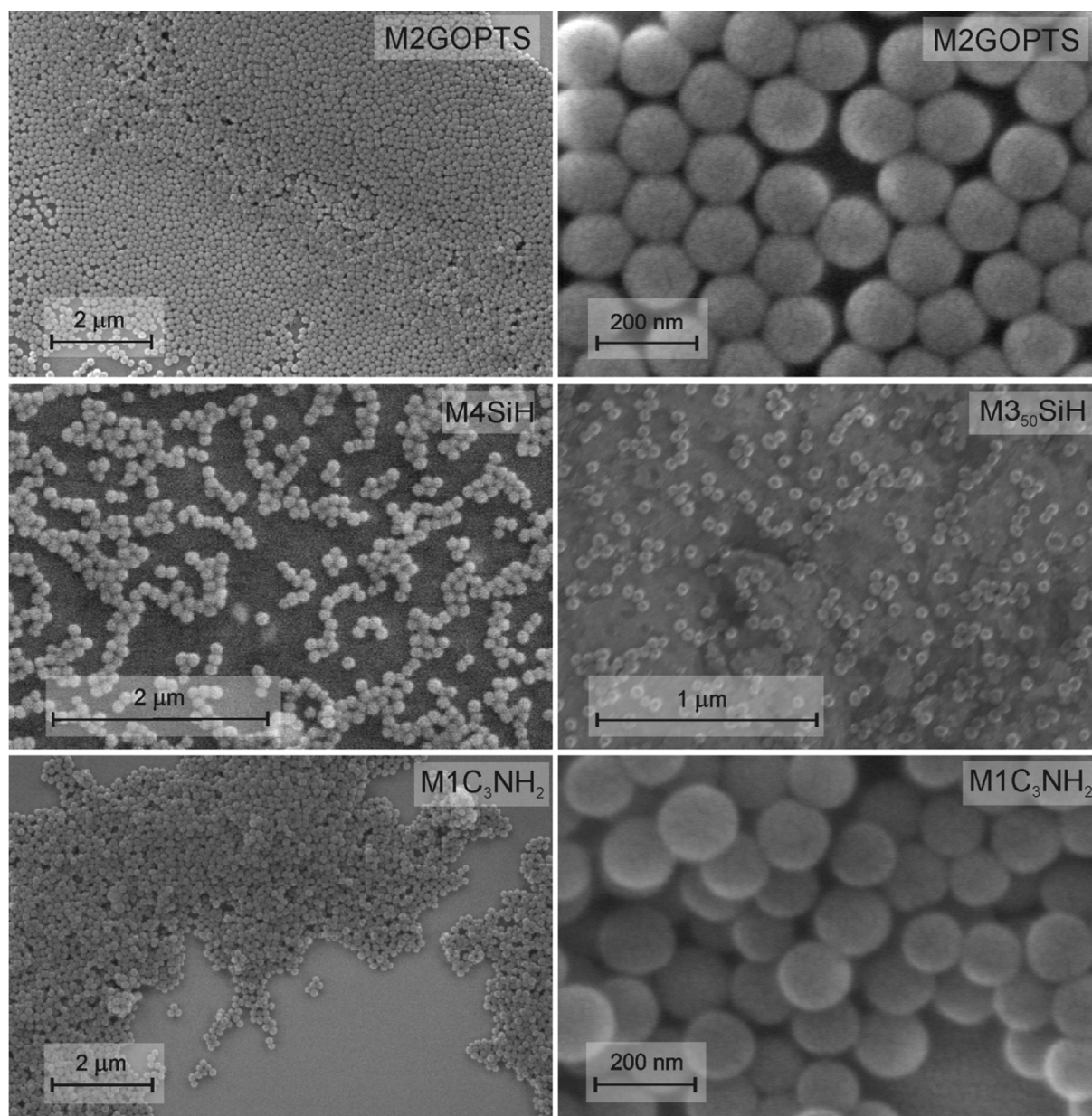


Figure 4.6 Scanning electron micrographs of $M1C_3NH_2$, $M2GOPTS$, $M4SiH$, and $M3_{50}SiH$.

4.3.3.2 Particle-Particle Interactions

Interactions between the particles were investigated by DLS, SEM and measurements of the zeta potential of the particles. Agglomeration of particles in solution can be observed by DLS and results in bigger average diameters as well as higher standard deviations and PDI values. The formation of three-dimensional agglomerates as well as repulsive interactions can also be seen in the SEM images (Figure 4.6). While bare particles **M0** and **M2GOPTS** do not agglomerate and arrange in close-packing of spheres (Figure 4.1, Figure 4.6), Si-H and amino functionalised particles behave differently. **M3SiH** and **M4SiH** do not agglomerate, either,

but additionally, electrostatic repulsion between single particles can be observed in the SEM pictures of both materials, silanised and hydrogenated particles (Figure 4.6). The average diameters d_{DLS} obtained by DLS in solution do not differ significantly from those of the starting materials (compare Table 4.2 and Table 4.6). The material **M3₅₀SiH** could not be resuspended to give stable suspensions, thus no reliable DLS values were obtained. SEM images of **M1C₃NH₂** show that the particles do not arrange in perfect sphere packing any more and DLS measurements result in significantly bigger average diameters than for the starting material ($d_{DLS} = 258 \pm 98$ for **M1C₃NH₂** and $d_{DLS} = 164 \pm 64$ **M0₁₃₀**), indicating that the particles of **M1C₃NH₂** agglomerate (see Table 4.6 and Figure 4.6).

Zetapotential. The zetapotential (ζ -potential) is one of the main forces which mediate interactions between particles in suspension. Particles with a high zeta potential (of positive or negative charge), repel each other (< -30 mV and $> +30$ mV are considered as high zeta potentials). For particles that are small enough, and whose density is low enough to remain in suspension, a high zeta potential confers stability, i.e. the particles in suspension resist aggregation.⁷²⁻⁷⁴

As the particles should be applied *in vitro* – or later on even *in vivo*, zetapotentials were determined in a phosphate buffered saline (PBS) and cell culture medium with 10% of serum, both at a physiological pH of 7.4. Serum containing cell culture medium (Dulbecco's Modified Eagle Medium (DMEM)) is used to mimic physiological conditions. The ζ -values of the unfunctionalised and surface modified materials (except **M1C₃NH₂** in PBS) (Table 4.7) are higher than -30 mV, i.e. the materials form stable suspensions and particles do not agglomerate under the conditions of the experiment (except **M3₅₀SiH**). Smaller ζ -values of about -30 to -10 mV were reported for unfunctionalised and Gd(III) chelate functionalised silica particles with smaller diameters of about 20 nm at pH 7.4.¹⁸

The ζ -values of the unfunctionalised particles in PBS decrease with the particle diameter and indicate that suspensions of **M0₁₃₀** and **M0₁₀₀** are more stable than suspensions of **M0₅₀** which is in accordance with the agglomeration behaviour observed during DLS measurements and with results reported in ref. 18. The highest ζ -potential of -56.3 mV in PBS was obtained for material **M4SiH**. The Si-H-bonds on the surface convert into Si-OH groups under the applied conditions, so a homogeneous hydrophilic surface is obtained which results in the ability to form stable suspensions and therefore a high ζ -potential. The value for **M3₁₀₀SiH** (-53.6 mV)

is lower because of additional -SiOEt moieties on the surface which have remained because of incomplete hydrolysis and condensation of TES. The ζ -potential of the smaller particles **M3₅₀SiH** (-45.4 mV) is smaller than the ζ -potential of the 100 nm particles. This coincides with the fact that no stable suspensions are obtained. The zeta potential of **M2GOPTS** in PBS is only slightly decreased in comparison to the starting material, here stable suspensions are obtained. The material **M1C₃NH₂** in PBS shows the only positive and the smallest ζ -value (23.9 mV). As already seen in SEM images and DLS measurements, particles of **M1C₃NH₂** agglomerate, which can be justified by their small zeta potential.

The ζ -potentials obtained in cell culture medium are all lower than those in PBS and do not differ significantly. Interestingly, interactions with proteins and other components of the medium seem to compensate differences between the materials. Values of the small 50 nm particles are comparable with those of the bigger NPs. Here the only exceptions are **M2GOPTS** with a remarkably high ζ -value of -48.5 mV and **M1C₃NH₂** with a very small, but negative ζ -value of -32.2 mV. So the components of the medium reverse the polarity of the positively charged amino modified surface of **M1C₃NH₂**.

Table 4.7 Zetapotentials of unfunctionalised and surface modified materials.

material	ζ -potential / mV	
	PBS	medium + 10% serum
M0₅₀	-46.3 ± 1.1	-39.0 ± 0.3
M0₁₀₀	-52.8 ± 1.0	-41.3 ± 1.5
M0₁₃₀	-55.7 ± 1.5	-45.3 ± 0.6
M1C₃NH₂	23.9 ± 0.8	-32.2 ± 0.4
M2GOPTS	-52.2 ± 0.6	-48.5 ± 0.9
M3₅₀SiH	-45.4 ± 1.0	-41.4 ± 0.9
M3₁₀₀SiH	-53.6 ± 0.5	-40.6 ± 0.8
M4SiH	-56.3 ± 0.8	-40.4 ± 0.5

Values represent mean ± SD.

4.3.3.3 Spectroscopic Investigations

Functionalisation of the particles was verified by DRIFT spectroscopy, ²⁹Si CP/MAS spectroscopy, and ¹³C CP/MAS NMR spectroscopy.

DRIFT Spectroscopy. In the DRIFT spectra of **M1C₃NH₂** (Figure 4.7 b) and **M2GOPTS** (Figure 4.7 c) it is difficult to demonstrate surface modification, as no additional significant vibrations in comparison to the starting material **M0reh** (Figure 4.7 a) occur. Only additional vibrations of CH_x groups (ν_{CH_x}) can be observed at 2942 and 2877 cm⁻¹.

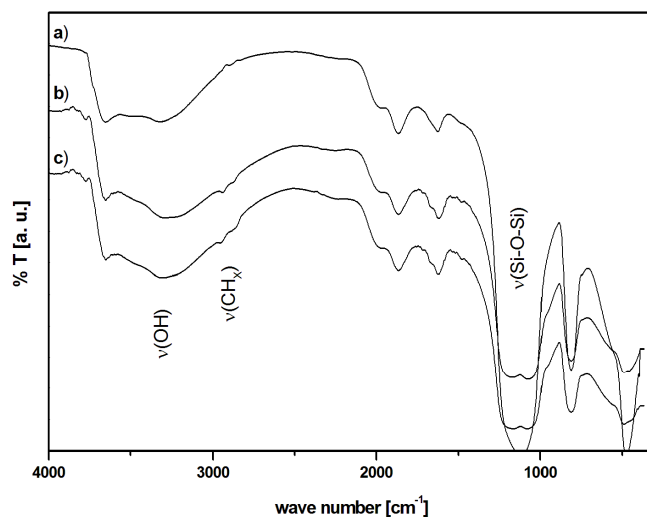


Figure 4.7 DRIFT spectra of a) **M0reh**, b) **M1C₃NH₂**, and c) **M2GOPTS**.

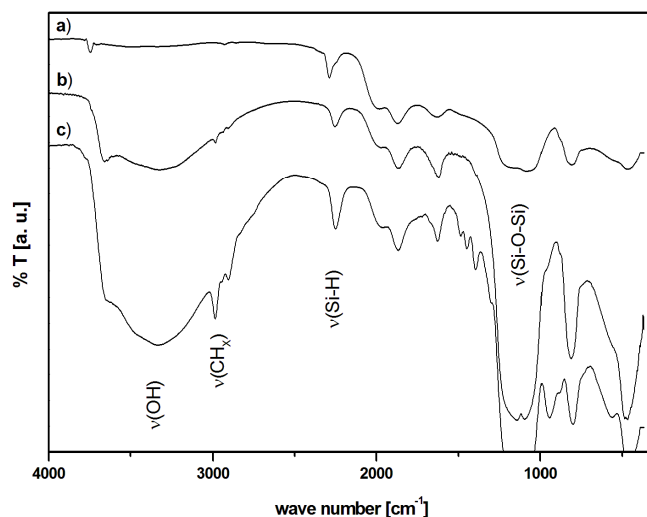


Figure 4.8 DRIFT spectra of a) **M4SiH**, b) **M3₁₀₀SiH**, and c) **M3₅₀SiH**.

DRIFT spectra of the Si-H modified NPs (Figure 4.8) show the characteristic Si-H vibrations (ν_{SiH}) for the materials **M3SiH** at 2256 cm⁻¹ and for **M4SiH** at 2287 cm⁻¹. Owing to the high temperature treatment, the vibrations of hydrogen bonded -OH groups disappear for **M4SiH**,

here only isolated silanol groups can be observed at 3748 cm^{-1} . For the smaller 50 nm particles, the ratio of surface groups to bulk is larger than for the 100 nm particles, thus in the spectrum of **M3₅₀SiH** the vibrations of -OH as well as Si-H groups are more intense than in the spectrum of **M3₁₀₀SiH**. The relatively intense vibrations of CH_x groups in the spectrum of **M3₅₀SiH** indicate that there are more -OEt moieties left on the surface. Signals of -OEt groups are also observed in the ¹³C CP/MAS NMR spectra of **M3₅₀SiH** (not shown).

Table 4.8 Assignments of IR vibrations of **M1C₃NH₂**, **M2GOPTS**, **M3SiH**, and **M4SiH**.

wave number / cm^{-1}				assignment
M1C₃NH₂	M2GOPTS	M3SiH	M4SiH	
			3748	isolated v(Si-OH)
3758 - 2970	3758 - 2970	3760 - 3006		different v (OH)
2935, 2877	2957, 2889	2985, 2904		v (CH _x)
		2256	2287	v (Si-H)
1969, 1868	1969, 1868	1991, 1866	1991, 1866	v (Si-O-Si)
1619	1619	1620		H ₂ O
1306 - 891	1306 - 891	1350 - 907	1350 - 907	v _{as} (Si-O-Si)
		1350 - 993 ^{a)}		(skeleton)

^{a)} **M3₅₀SiH**

Solid State NMR Spectroscopy. By ²⁹Si HPDEC/MAS NMR spectroscopy it should be possible to get a quantitative estimation of all ²⁹Si signals of the nanoparticles. Thus, after functionalisation of the surface, signals of Q and T groups should be detectable. After Si-H functionalisation, the signal of the T³_H groups in the region of -60 to -90 ppm could not be detected within a reasonable period of time for neither **M3SiH** nor **M4SiH**, due to the low ratio of the surface T³_H to Q⁴ groups in the bulk material. Therefore, ²⁹Si CP/MAS NMR spectra of the materials were recorded to get the qualitative information of the chemical shifts of the different Si species. Note, that with CP/MAS NMR measurements it is not possible to get a quantitative estimation of the Si signals. As cross polarisation of the protons to silicon nuclei will affect only those silicon nuclei which are within the distance of four bonds, only a small amount of silicon nuclei will produce an NMR signal. Therefore, the ratio of the intensities of Q³ and Q⁴ groups is reversed in comparison to the ratio of the signals in the HPDEC spectra of the **M0** materials.

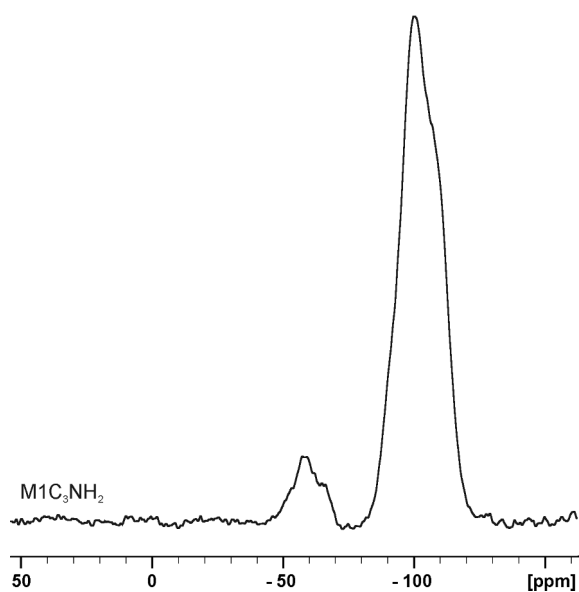


Figure 4.9 ^{29}Si CP/MAS NMR spectrum of $\text{M1C}_3\text{NH}_2$.

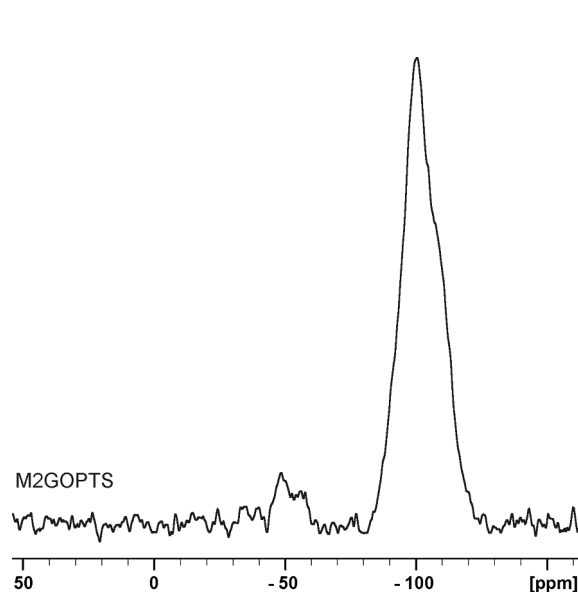


Figure 4.10 ^{29}Si CP/MAS NMR spectrum of M2GOPTS .

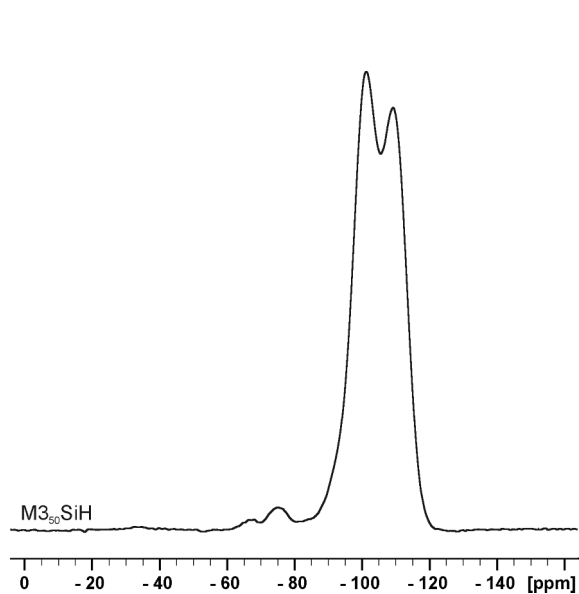


Figure 4.11 ^{29}Si CP/MAS NMR spectrum of $\text{M3}_{50}\text{SiH}$.

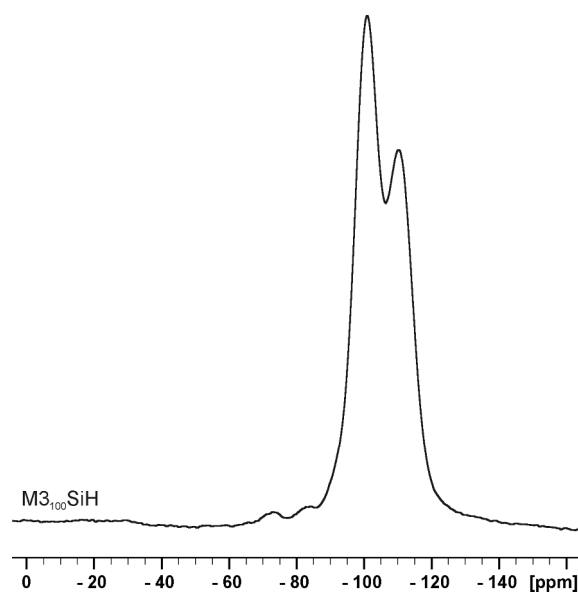


Figure 4.12 ^{29}Si CP/MAS NMR spectrum of $\text{M3}_{100}\text{SiH}$.

In the ^{29}Si CP/MAS NMR spectrum of $\text{M1C}_3\text{NH}_2$ signals of T^2 and T^3 groups are observed at -43 to -72 ppm and peaks of Q^3 and Q^4 groups at -82 to -124 ppm (Figure 4.9). In the spectrum of M2GOPTS the resonances of T^2 and T^3 groups are observed at -43 to -62 ppm and the signals of Q^3 and Q^4 groups at -82 to -124 ppm (Figure 4.10). The resonances of T^2_{H} and T^3_{H} groups of the M3SiH materials are weak, but observable at -67 and -75 ppm for

M3₅₀SiH and at -73 and -83 ppm for **M3₁₀₀SiH**. Q³ and Q⁴ groups are observed at -87 to -130 ppm (Figure 4.11, Figure 4.12). The ²⁹Si CP/MAS NMR spectrum of **M4SiH** (not depicted) only shows a broad signal from -80 to -120 ppm.

The ¹³C CP/MAS NMR spectra of **M1C₃NH₂** and **M2GOPTS** give evidence for the successful surface modification by silanisation. The spectrum of **M1C₃NH₂** (Figure 4.13) shows the signals of the propyl chain and -OEt moieties (indicated with *) and in the spectrum of **M2GOPTS** (Figure 4.14) the signals of the glycidyloxypropyl chain can be observed.

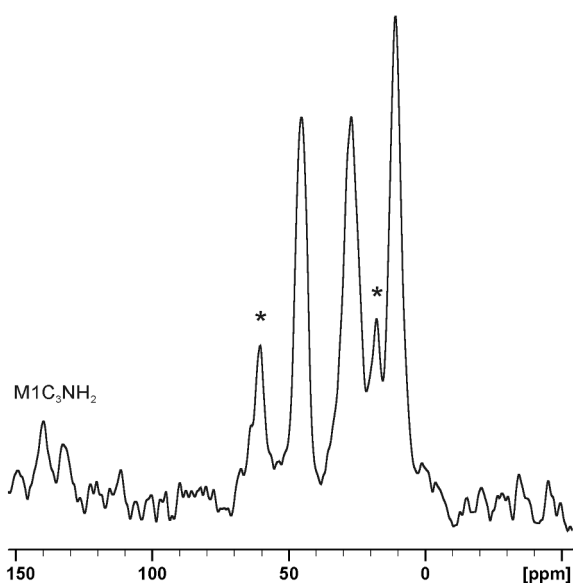


Figure 4.13 ¹³C CP/MAS NMR spectrum of **M1C₃NH₂**.

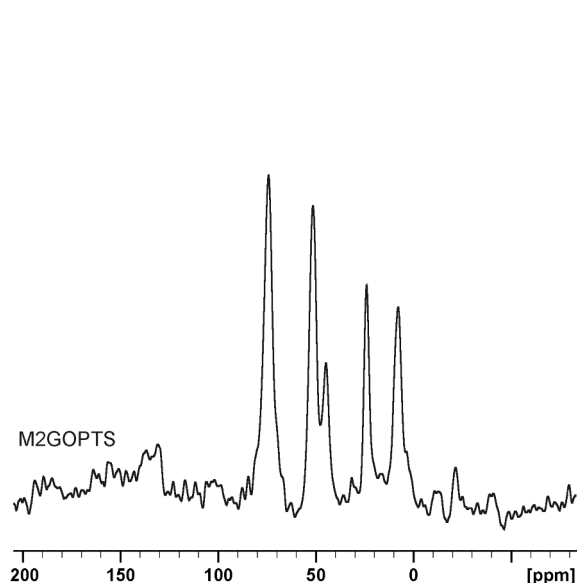


Figure 4.14 ¹³C CP/MAS NMR spectrum of **M2GOPTS**.

4.3.3.4 Specific Surface Area of the surface modified Stöber Particles

The specific surface areas A_{BET} of the surface modified materials (Table 4.9) are all decreased in comparison to A_{BET} of the respective starting materials. The clearest decrease of A_{BET} by 29% is observed in the case of **M4SiH** and can be explained by the high temperature treatment. Micropores in the material coalesce due to the formation of new siloxane bonds and water. Thus, the surface accessible for N₂ decreases. For the silanised materials A_{BET} is reduced by 13-16%. Due to the sol-gel process on the surface of the starting material **M0**, micropores get inaccessible for nitrogen and a smaller surface area is measured (compare Table 4.4).

Table 4.9 Specific surface areas of the surface modified materials.

material	$A_{\text{BET}} / \text{m}^2 \text{g}^{-1}$
M1C₃NH₂	26
M2GOPTS	26
M3a₁₀₀SiH	38
M3b₁₀₀SiH	40
M3₅₀SiH	91
M4SiH	31

4.3.3.5 Specific Surface Concentration of Functional Groups

The extent of surface functionalisation was quantified by means of elemental analysis (EA) for the materials **M1C₃NH₂** and **M2GOPTS**.

To determine the extent of surface modification, the number of silanol groups α_{OH} on the surface of the particles, to be functionalised, has to be known. An average value of $\alpha_{\text{OH}} = 4.9 \text{ OH nm}^{-2}$ has been reported.⁶⁵ The specific surface area A_{BET} of the starting materials **M0** was determined by nitrogen adsorption experiments, and evaluated according to the multipoint Brunauer-Emmet-Teller (BET) method (Table 4.4). The surface concentration $\Gamma_{(\text{ligand})}$ of any ligand, coupled to the surface, is calculated from the corrected percentage of carbon (%C), obtained from EA, by Eq. 4.1, where n_{c} is the number of carbon atoms in the ligand, and M_{c} is the molecular weight of carbon.

$$\Gamma_{(\text{ligand})} = \%C \cdot (100 \cdot n_{\text{c}} \cdot M_{\text{c}})^{-1} \left[\frac{\text{mol}}{\text{g}} \right] \quad \text{Eq. 4.1}$$

The number of coupled ligands per area $\alpha_{(\text{ligand})}$ is calculated by Eq. 4.2, where N_{A} is the Avogadro constant and A_{BET} the specific surface area of the particles.

$$\alpha_{(\text{ligand})} = \Gamma_{(\text{ligand})} \cdot N_{\text{A}} \cdot A_{\text{BET}}^{-1} \times 10^{-21} \left[\frac{\text{ligand}}{\text{nm}^2} \right] \quad \text{Eq. 4.2}$$

For **M1C₃NH₂** and **M2GOPTS** the ratio of $\alpha_{(\text{ligand})}/\alpha_{\text{OH}}$ is 0.53 and 0.30, respectively, which means that 53% and 30% of the silanol groups have reacted with a functionalised silane, assuming that each alkoxy silane only forms one siloxane bond with the particle surface (Table 4.10). In fact there can be formed one, most likely two or rarely even up to three siloxane bonds. If surface concentrations Γ are compared, it can be assumed that in the case of **M1C₃NH₂** $130 \mu\text{mol g}^{-1}$ and in the case of **M2GOPTS** $70 \mu\text{mol g}^{-1}$ of ligand were coupled to

the 242 $\mu\text{mol g}^{-1}$ silanol groups of **M0**₁₃₀. For **M1C**₃**NH**₂ this is an overestimation, as the ¹³C CP/MAS NMR spectrum shows, that ethanol moieties are left on the surface. Thus, the values given should be regarded as estimations rather than as precise numbers.

Table 4.10 Evaluation of elemental analyses based on % of carbon (%C).

	$A_{\text{BET}} / \text{m}^2 \text{g}^{-1}$	%C (EA)	corr %C (EA)	$\Gamma_{(\text{ligand})} / \text{mmol g}^{-1}$	$\alpha_{\text{ligand}} / \text{nm}^{-2}$	$\alpha_{(\text{ligand})} / \alpha_{\text{OH}}$
M0 ₁₃₀	30	0.08				
M1C ₃ NH ₂		0.54	0.46	0.13	2.59	0.53
M2GOPTS		0.61	0.53	0.07	1.49	0.30

To get an estimate of the surface concentration $\Gamma_{\text{Si-H}}$ of Si-H groups, it was assumed that every silanol group on the surface of the particles was converted into one Si-H group. The numbers given in Table 4.11 were calculated from the specific surface area A_{BET} of the Si-H modified materials, not from A_{BET} of the starting materials like in the case of **M1C**₃**NH**₂ and **M2GOPTS**. These values should be regarded as the maximum numbers of Si-H groups on the particles' surface which are theoretically possible.

Table 4.11 Specific surface concentration of Si-H groups.

material	$A_{\text{BET}} / \text{m}^2 \text{g}^{-1}$	$\Gamma_{\text{Si-H}} / \mu\text{mol g}^{-1 \text{ a)}$
M3a ₁₀₀ SiH	38	310
M3b ₁₀₀ SiH	40	326
M3 ₅₀ SiH	91	739
M4SiH	31	251

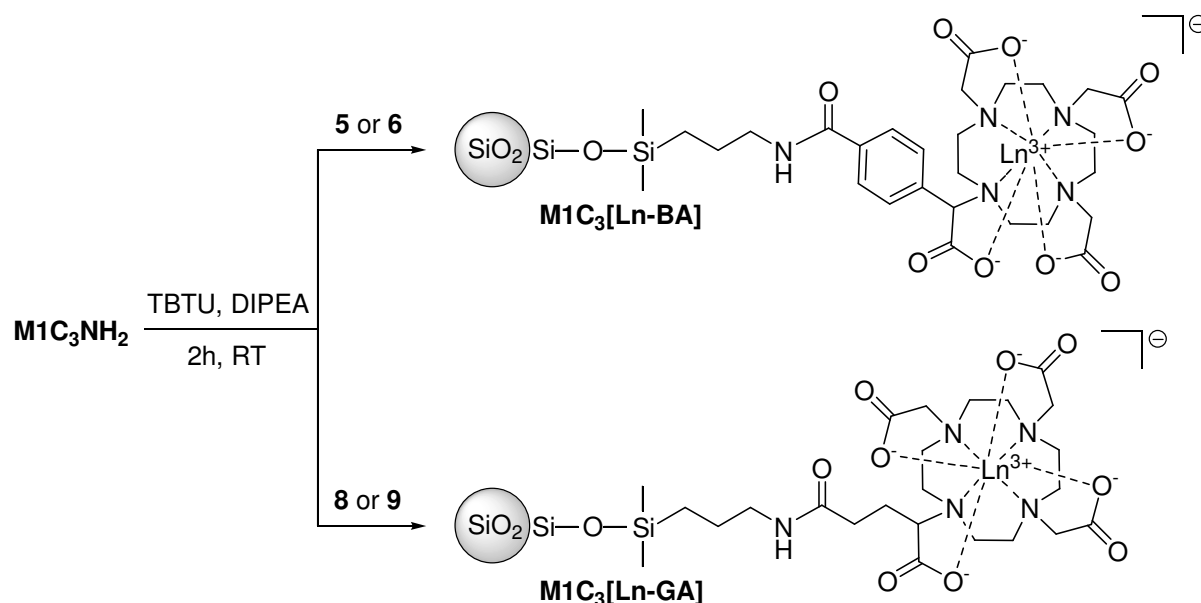
^{a)} calculated from A_{BET} and $\alpha_{\text{OH}} = 4.9 \text{ OH nm}^{-2}$

4.4 Coupling of Ln[DOTA] and Ln[DO3A] Derivatives to **M1C**₃**NH**₂ and **M2GOPTS**

4.4.1 Syntheses

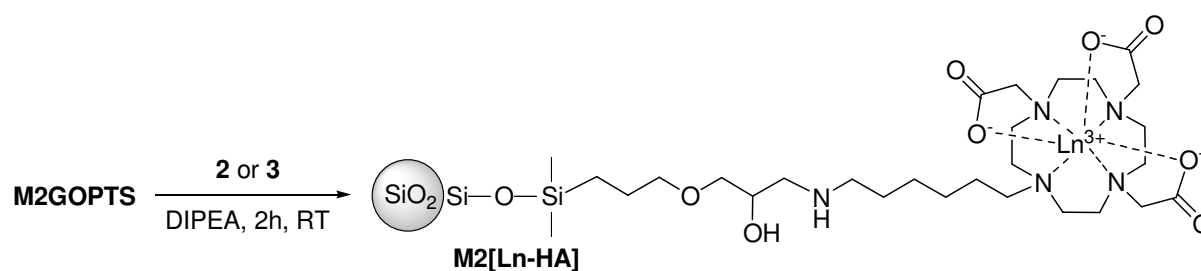
For all coupling reactions of amines with carboxylic acids in this work the classical peptide coupling agent *O*-(benzotriazol-1-yl)-*N,N,N',N'*-tetramethyluronium tetrafluoroborate (TBTU) and diisopropylethylamine (DIPEA) as base were applied.⁷⁵

The amino functionalised NPs $\text{M1C}_3\text{NH}_2$ were reacted with the carboxylic acid terminated DOTA derivatives $\text{Ln}[\text{DOTA-BA}]$ (**5**, **6**) and $\text{Ln}[\text{DOTA-GA}]$ (**8**, **9**). Therefore, the DOTA derivatives were activated with TBTU and DIPEA and added to a suspension of $\text{M1C}_3\text{NH}_2$ in DMSO, giving the new materials $\text{M1C}_3[\text{Ln-BA}]$ and $\text{M1C}_3[\text{Ln-GA}]$. As counterion $n\text{-Bu}_4\text{N}^+$ was used. In the case of $\text{M1C}_3[\text{Ln-BA}]$ one batch was synthesised with sodium as counterion. The behaviour of the two different $\text{M1C}_3[\text{Ln-BA}]$ materials was not changed to an observable extent and thus, is not further discussed.



Scheme 4.8 Syntheses of $\text{M1C}_3[\text{Ln-BA}]$ and $\text{M1C}_3[\text{Ln-GA}]$. Ln = Gd or Y.

To the epoxy functionalised NPs M2GOPTS , $\text{Ln}[\text{DO3A-HA}]$ (**2**, **3**) was coupled by stirring the reactants in DMSO with DIPEA, yielding $\text{M2}[\text{Ln-HA}]$.



Scheme 4.9 Synthesis of $\text{M2}[\text{Ln-HA}]$. Ln = Gd or Y.

4.4.2 Characterisation

4.4.2.1 Size and Shape

The size d_{SEM} and the shape of single particles of **M2[Gd-HA]** has not changed in comparison to the starting material **M2GOPTS**, which can be seen in Figure 4.15 and Table 4.12. There were no SEM investigations made for the Gd(III) modified **M1** materials.

Table 4.12 Size characterisation of [Gd] modified materials.

material	d_{DLS} / nm	PDI	d_{SEM} / nm
M1C₃[Gd-GA]	157 ± 50	0.166	-
M1C₃[Gd-BA]	151 ± 38	0.089	-
M2[Gd-HA]	149 ± 44	0.132	137 ± 11

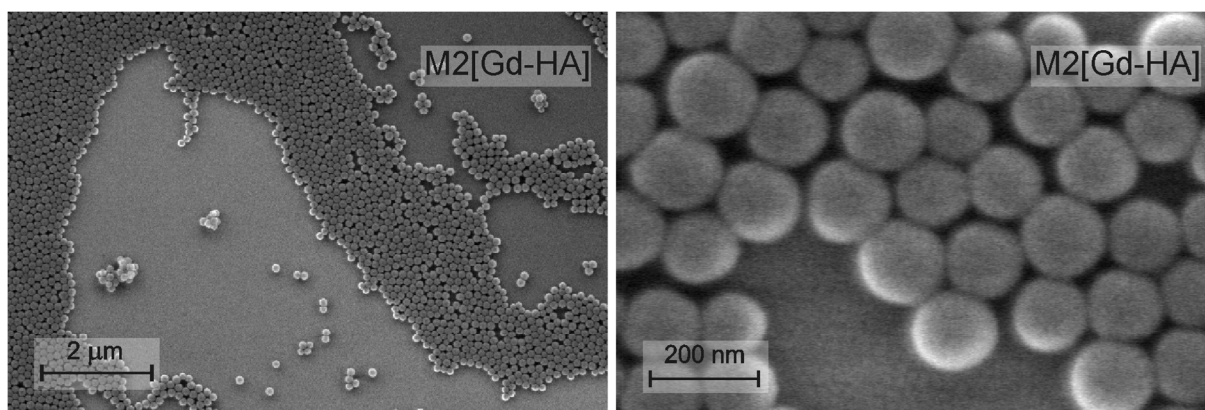


Figure 4.15 Scanning electron micrographs of **M2[Gd-HA]**.

4.4.2.2 Particle-Particle Interactions

After coupling Gd[DOTA-BA] or Gd[DOTA-GA] to **M1C₃NH₂**, d_{DLS} of the resulting materials **M1C₃[Gd-BA]** and **M1C₃[Gd-GA]** is significantly decreased from 258 ± 98 nm to 151 ± 38 nm and 157 ± 50 nm, respectively. This indicates, that the particles of **M1C₃[Gd-BA]** and **M1C₃[Gd-GA]** do not agglomerate in solution.

The hydrodynamic diameter and the SEM images of **M2[Gd-HA]** do not differ from d_{DLS} and the pictures of the starting material **M2GOPTS**, so coupling of Gd[DO3A-HA] did not change the surface properties of the particles to an observable extent.

In the case of the **M1** materials negatively charged complexes were coupled to the particles' surface. As desired, this prevents the agglomeration of the particles. However, coupling of

uncharged complexes to the **M2** material does not cause agglomeration. Thus, no significant role can be ascribed to the charge of the coupled complex regarding agglomeration of particles.

Zetapotential. After coupling the DOTA derivatives to **M1C₃NH₂**, the ζ -values of the resulting materials in PBS (Table 4.13) are negative and significantly higher, so the improved agglomeration behaviour correlates well with the zetapotential. According to previous observations, the zetapotential of **M2[Gd-HA]** does not differ significantly from the potential of the starting material **M2GOPTS**. In medium the obtained ζ -values are comparable with those of **M0₁₃₀** and **M2GOPTS** and higher than the values of 100 nm materials, so here the influence on the potential seems to be dominated by the particle size.

Table 4.13 Zetapotentials of [Ln] modified materials **M1** and **M2**.

material	ζ -potential / mV	
	PBS	medium + 10% serum
M1C₃[Gd-BA]	-51.3 ± 1.9	-45.7 ± 0.4
M1C₃[Gd-GA]	-55.0 ± 0.9	-48.6 ± 1.4
M2[Gd-HA]	-54.7 ± 0.5	-47.9 ± 0.3

Values represent mean ± SD.

4.4.2.3 Spectroscopic Investigations

In the DRIFT spectra of **M1C₃[Gd-GA]** and **M1C₃[Y-BA]** (Figure 4.16) coupling of the Ln[DOTA] derivatives can be verified by CH_x vibrations at 2960, 2926 and 2867 cm⁻¹ as well as intense carbonyl and amide vibrations at 1620 cm⁻¹. The higher intensity of the CH_x and amide vibrations in the spectrum of **M1C₃[Y-BA]** indicates, that the coupling efficacy is higher for Ln[DOTA-BA] as for Ln[DOTA-GA].

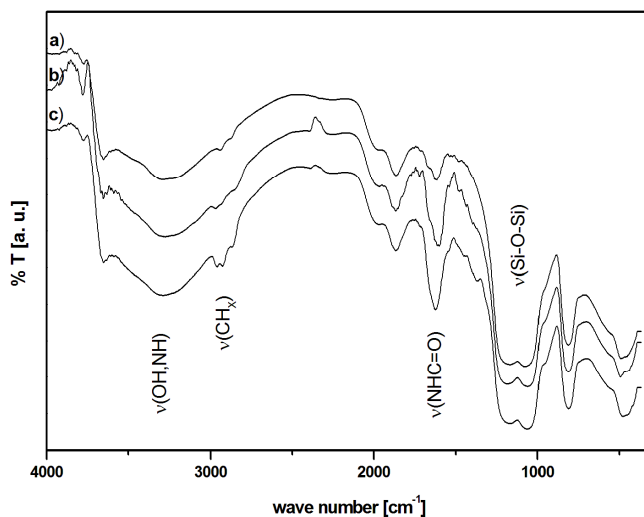


Figure 4.16 DRIFT spectra of a) $\text{M1C}_3\text{NH}_2$, b) $\text{M1C}_3[\text{Gd-GA}]$, and c) $\text{M1C}_3[\text{Y-BA}]$.

Coupling of $\text{Ln}[\text{DO3A-HA}]$ to M2GOPTS cannot clearly be verified by DRIFT spectroscopy, as the spectrum of $\text{M2}[\text{Gd-HA}]$ does not differ significantly from the spectrum of M2GOPTS (Figure 4.17). The intensity of the vibration at 1619 cm^{-1} , which can be assigned to H_2O in the spectrum of M2GOPTS , is only slightly increased. This indicates a less effective functionalisation of M2GOPTS with Gd(III) complexes.

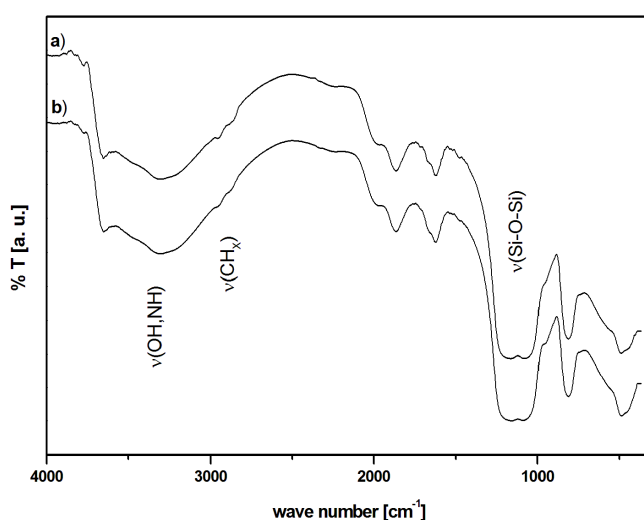


Figure 4.17 DRIFT spectra of a) M2GOPTS and b) $\text{M2}[\text{Gd-HA}]$.

Table 4.14 Assignments of IR vibrations of **M1C₃[Gd-GA]**, **M1C₃[Y-BA]**, and **M2[Gd-HA]**.

wave number / cm ⁻¹			assignment
M1C₃[Gd-GA]	M1C₃[Y-BA]	M2[Gd-HA]	
3758 - 3000	3758 - 3000	3758 - 2970	different ν (OH)
2969, 2851	2960, 2926, 2867	2957, 2889	ν (CH _x)
1969, 1868	1969, 1868	1969, 1868	ν (Si-O-Si)
1610	1620		ν (NHC=O)
		1619	H ₂ O
1290 - 880	1290 - 880	1306 - 891	ν_{as} (Si-O-Si) (skeleton)

4.4.2.4 Specific Surface Concentration of Gadolinium

Surface concentration $\Gamma_{\text{Gd(III)}}$ of Gd(III) was determined by measurements of the longitudinal relaxation time T_1 by inversion recovery experiments.

Gd(III) concentrations of **M1C₃[Gd-GA]** and **M1C₃[Gd-BA]** verify the higher coupling efficacy for Ln[DOTA-BA], already seen in the DRIFT spectra (Figure 4.16). Relating to the total amount of silanol groups available on the surface of **M0₁₃₀** a coverage of Gd(III) of 14% has been achieved for **M1C₃[Gd-BA]**, whereas the coverage for **M1C₃[Gd-GA]** and **M2[Gd-HA]** is only 5% (Table 4.15). A maximum coverage of 53% for the **M1** materials and of 30% for **M2** could have been achieved related to the extent of surface modification (compare Table 4.10).

Table 4.15 Gadolinium content $\Gamma_{\text{Gd(III)}}$ of [Gd] functionalised materials **M1** and **M2**.

material	$\Gamma_{\text{Gd(III)}} / \mu\text{mol g}^{-1}$	$\alpha_{\text{Gd}}/\alpha_{\text{OH}} / \%$	n_{Gd} per NP	$n_{\text{Gd}}/n_{\text{Gd,geo}} / \%$
M1C₃[Gd-BA]	34	14	46.434	62
M1C₃[Gd-GA]	11	5	15.023	20
M2[Gd-HA]	12	5	16.452	22

Geometrical considerations assuming ideal conditions show that the space available on the particles' surface is well exploited for the higher loaded material. The geometrical surface area A_{geo} of a particle of the **M1** and the **M2** materials (calculated from $d_{\text{SEM}} = 137$ nm) is 5.9×10^{-14} m². The hydrodynamic radius of the Gd(III) complexes is about 0.5 nm⁶⁰, so they

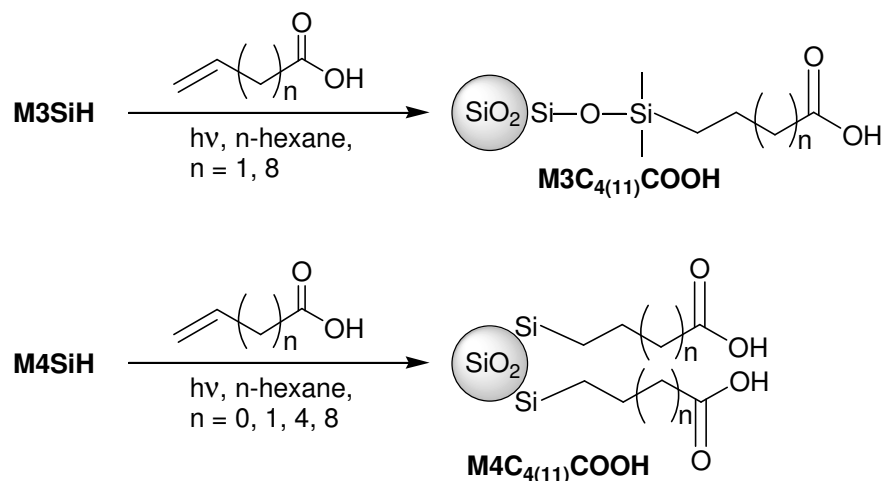
need an area of $7.9 \times 10^{-19} \text{ m}^2$ each. Thus, a maximum number $n_{\text{Gd,geo}}$ of 75.076 Gd(III) complexes has room around a single particle. In Table 4.15 the numbers n_{Gd} of Gd(III) per NP and their percentage of the possible number $n_{\text{Gd,geo}}$ are given. For **M1C₃[Gd-BA]** 62% of the maximum number are achieved, for **M1C₃[Gd-GA]** and **M2[Gd-HA]** only 20 and 22%.

4.5 Further Functionalisation of Si-H modified Materials **M3SiH** and **M4SiH**

4.5.1 Syntheses

4.5.1.1 Photochemical Hydrosilylation

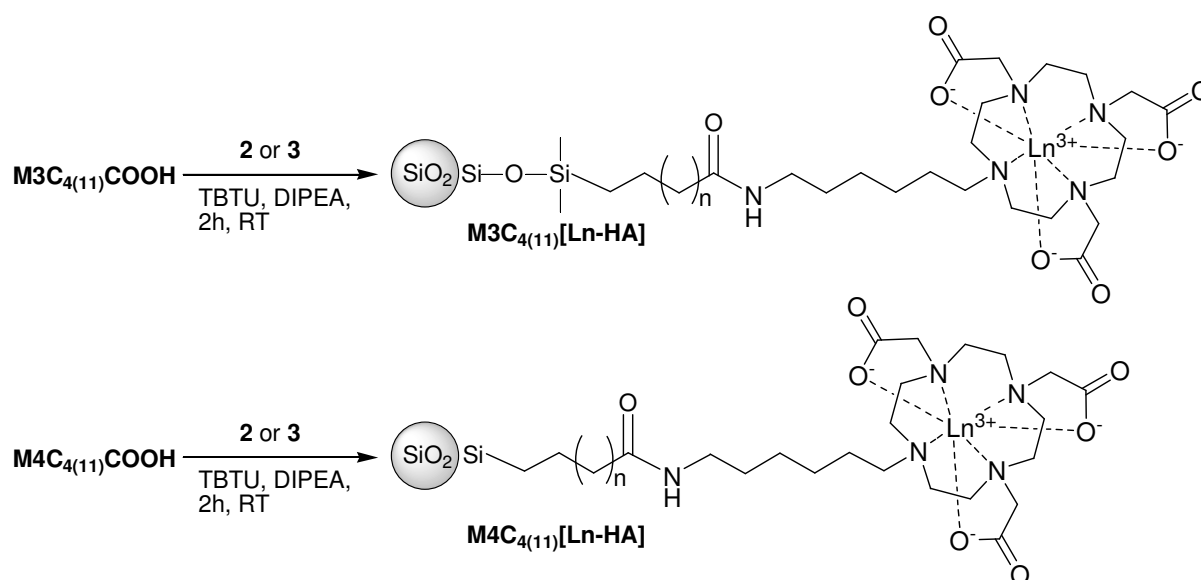
The Si-H modified materials were functionalised with carboxylic acid groups prior to coupling of amino terminated Ln(III) complexes. The carboxylic acid groups were introduced by a photochemically induced hydrosilylation reaction of terminal unsaturated carboxylic acids of different chain lengths. **M4SiH** was reacted with acrylic acid, 3-butenic acid, 6-heptenoic acid, and 10-undecylenic acid to determine the ideal chain length for an optimal degree of functionalisation. Acrylic acid could not be added to the Si-H bonds on the surface of the particles, as polymerisation of the molecules in solution takes place too fast. The most effective coupling could be reached with 3-butenic acid and the most cost-effective reactant is 10-undecylenic acid. Therefore, 3-butenic acid and 10-undecylenic acid were used to modify **M3SiH** and **M4SiH** and the properties of the resulting materials **M3C₄₍₁₁₎COOH** and **M4C₄₍₁₁₎COOH** (Scheme 4.10) were compared. The smaller particles **M3₅₀SiH** were only modified with 3-butenic acid, yielding **M3₅₀C₄COOH**. The photochemical hydrosilylation reaction was carried out under argon in carefully degassed *n*-hexane under irradiation with a 700 W medium pressure mercury lamp for 5 days.



Scheme 4.10 Carboxylic acid functionalisation of **M3SiH** and **M4SiH**.

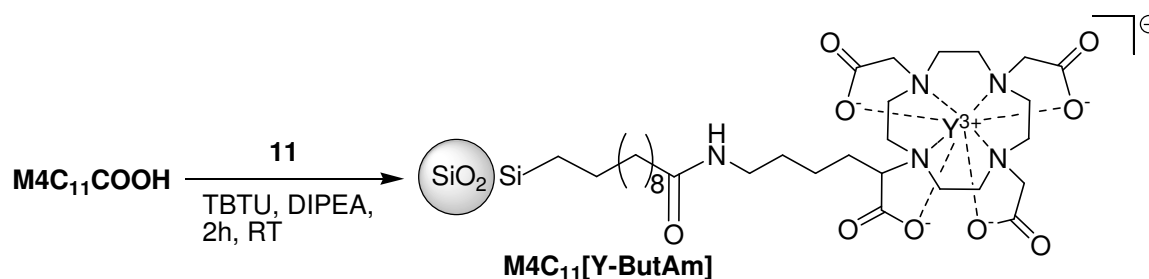
4.5.1.2 Coupling of Ln[DO3A-HA]

The acid functionalised NPs **M3C₄₍₁₁₎COOH** and **M4C₄₍₁₁₎COOH** were reacted with the amino terminated DO3A derivative Ln[DO3A-HA] (**2**, **3**). Therefore, the particles were suspended in DMSO, activated with TBTU and DIPEA and a solution of the Ln(III) complex in DMSO was added, yielding the new materials **M3C₄₍₁₁₎[Ln-HA]** and **M4C₄₍₁₁₎[Ln-HA]**.



Scheme 4.11 Coupling of Ln[DO3A-HA] to the acid modified materials.

4.5.1.3 Coupling of Y[DOTA-ButAm]

Scheme 4.12 Coupling of Ln[DOTA-ButAm] to M4C₁₁COOH.

To compare the agglomeration behaviour of the particles subject to the charge of the coupled complex, the charged Ln(III) complex Y[DOTA-ButAm] **11** with sodium as counterion was coupled to the surface of M4C₁₁COOH.

4.5.2 Characterisation and Examination

4.5.2.1 Size and Shape

The size d_{SEM} and the shape of single particles of the acid modified as well as the Ln(III) complex modified particles is not changed in comparison to their respective starting materials (d_{SEM} Table 4.16, Figure 4.18).

Table 4.16 Size characterisation of acid and [Ln] modified materials.

material	d_{DLS} / nm	PDI	d_{SEM} / nm
M4bC ₁₁ COOH	230 ± 88	0.353	104 ± 5
M3bC ₁₁ COOH	228 ± 84	0.296	117 ± 11
M4aC ₄ COOH	182 ± 64	0.243	112 ± 11
M3aC ₄ COOH	173 ± 71	0.496	106 ± 9
M3 ₅₀ C ₄ COOH	-	-	55 ± 5
M4bC ₁₁ [Y-HA]	290 ± 113	0.397	119 ± 12
M4bC ₁₁ [Gd-HA]	259 ± 162	0.504	120 ± 14
M3bC ₁₁ [Gd-HA]	140 ± 65	0.167	116 ± 11
M4aC ₄ [Gd-HA]	144 ± 56	0.537	107 ± 10
M3aC ₄ [Gd-HA]	168 ± 59	0.393	105 ± 9
M3 ₅₀ C ₄ [Gd-HA]	-	-	54 ± 4
M4bC ₁₁ [Y-ButAm]	-	-	-

4.5.2.2 Particle-Particle Interactions

In Table 4.16 the materials are arranged according to the spacer length, as this factor influences the agglomeration behaviour the most.

The Stöber particles formed large agglomerates when they were functionalised with 10-undecylenic acid (**M3C₁₁COOH**, **M4C₁₁COOH**), and even larger agglomerates, when the Ln(III) complexes were coupled to the C₁₁ spacer (**M3C₁₁[Ln-HA]**, **M4C₁₁[Ln-HA]**). In contrast, 3-butenic acid functionalised particles (**M3C₄COOH** and **M4C₄COOH**) and their corresponding materials with Ln(III) complexes (**M3C₄[Ln-HA]** and **M4C₄[Ln-HA]**) form only small agglomerates in solution, which can be shown by DLS as well as SEM (Table 4.16, Figure 4.18). The 50 nm materials **M3₅₀C₄COOH** and **M3₅₀C₄[Ln-HA]** do not give stable suspensions upon resuspending them in water and thus, DLS measurements give no reliable values.

Interestingly, Y[DOTA-ButAm] coupled particles **M4bC₁₁[Y-ButAm]** formed huge agglomerates and were hardly resuspendable in water after drying the material. SEM images (not depicted) show huge agglomerates and DLS measurements were not possible due to strong agglomeration phenomena.

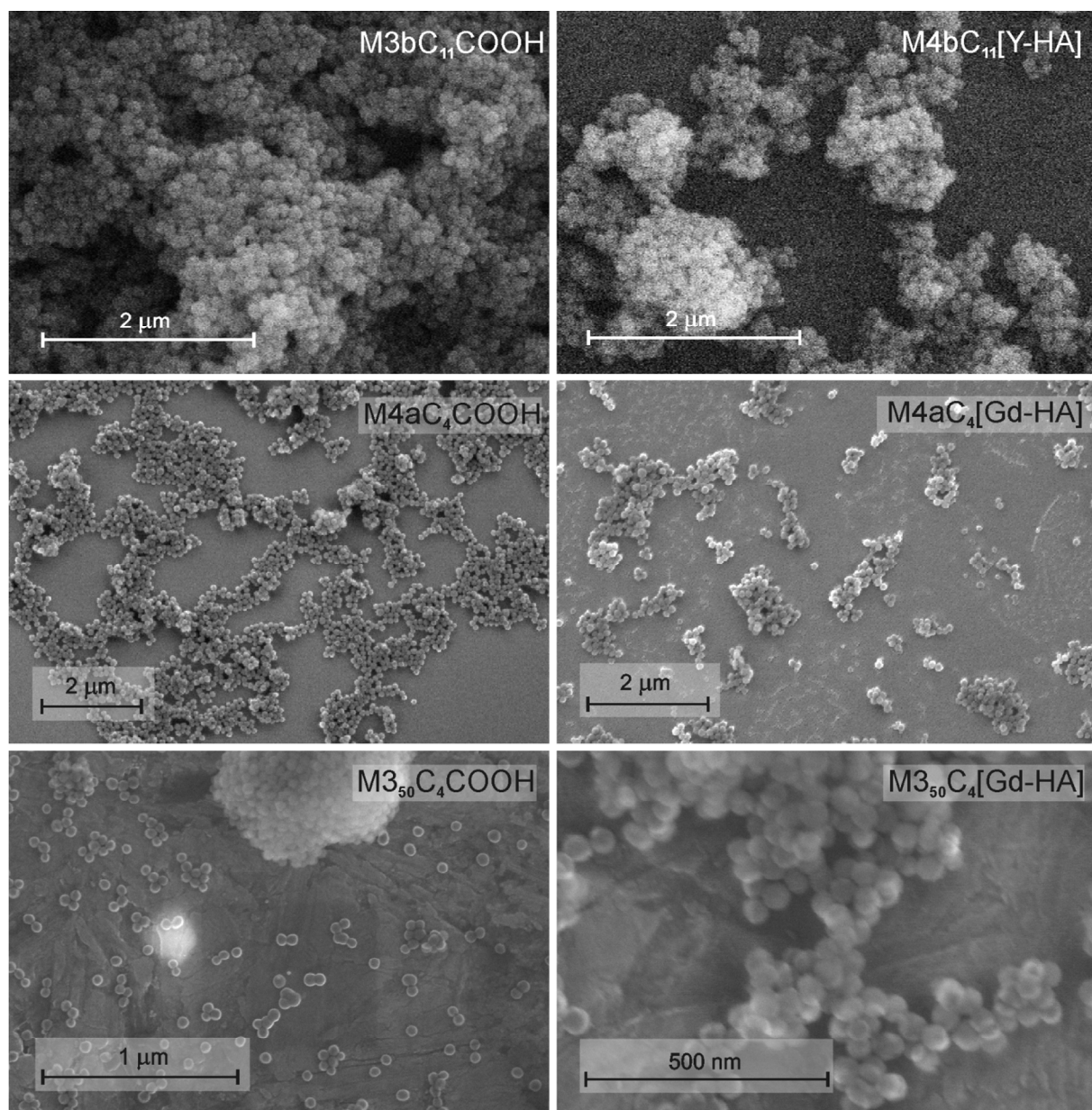


Figure 4.18 Scanning electron micrographs of **M3bC₁₁COOH**, **M4bC₁₁[Y-HA]**, **M4aC₄COOH**, **M4aC₄[Gd-HA]**, **M3₅₀C₄COOH**, and **M3₅₀C₄[Gd-HA]**.

Zetapotential. According to the observations above, the lowest zetapotential of the bigger particles in PBS is obtained for **M4C₁₁[Y-ButAm]** (-43.1 mV). The ζ -potentials of the acid and [Gd] modified materials in PBS are lower than those of the Si-H modified materials and do not differ significantly within the series **M3** and **M4**. ζ -potentials are higher for [Gd] modified materials with the C₄ spacer than with the C₁₁ spacer, which is coincident with the observation of agglomeration of the C₁₁ materials (compare DLS results, Table 4.16 and Figure 4.18). The ζ -values do not drastically change after coupling the Ln(III) complexes, as the chemical environment does not change very much. The chelating ligand contains three

carboxyl groups and not all of the carboxylic acid groups react with the Gd(III) complexes, so free carboxylic acid groups are left after coupling of the chelates.

The unreacted Si-OH groups on the surface of the **M4** materials are responsible that the ζ -potentials of the series **M4** are higher than those of the series **M3**.

The ζ -potential in PBS of the smaller particles **M3₅₀C₄COOH** is very low (-36.4 mV), whereas the potential of **M3₅₀C₄[Ln-HA]** is increased (-48.5 mV) and comparable with the potentials of the C₁₁ materials.

Table 4.17 Zetapotentials of acid and [Ln] modified materials **M3** and **M4**.

material	ζ -potential / mV	
	PBS	medium + 10% serum
M3₅₀C₄COOH	-36.4 ± 0.3	-39.0 ± 1.4
M3aC₄COOH	-52.5 ± 0.7	-41.4 ± 0.5
M3bC₁₁COOH	-51.0 ± 0.8	-46.0 ± 0.7
M4aC₄COOH	-54.0 ± 0.7	-41.9 ± 0.1
M4bC₁₁COOH	-55.2 ± 0.6	-43.2 ± 0.5
M3₅₀C₄[Gd-HA]	-48.5 ± 0.9	-44.2 ± 1.2
M3bC₁₁[Gd-HA]	-46.6 ± 0.4	-42.9 ± 0.9
M3aC₄[Gd-HA]	-50.7 ± 0.9	-43.7 ± 0.2
M4aC₄[Gd-HA]	-50.7 ± 0.9	-45.0 ± 0.4
M4bC₁₁[Gd-HA]	-49.9 ± 0.6	-42.9 ± 0.4
M4bC₁₁[Y-HA]	-50.5 ± 0.6	-40.5 ± 0.6
M4bC₁₁[Y-ButAm]	-43.1 ± 0.3	-42.9 ± 0.8

Values represent mean ± SD.

The ζ -potentials obtained in cell culture medium are again lower than those in PBS (except for **M3₅₀C₄COOH**) and do not differ significantly due to the interactions with proteins and other components of the medium, which compensate differences. However, the highest ζ -values in medium were obtained for the [Gd] functionalised particles, i.e. in medium they form the most stable suspensions, which can be important for their application.

4.5.2.3 Spectroscopic Investigations

DRIFT Spectroscopy. After hydrosilylation, the vibration of the carbonyl group ($\nu_{\text{C=O}}$) is found at 1714 and 1709 cm^{-1} , respectively, for **M4C₄₍₁₁₎COOH** and **M3C₄₍₁₁₎COOH**. Besides, the intensity of ν_{CH_x} has grown significantly. The addition of the C=C double bond of the spacer to the Si-H bonds on the surface is indicated by the absence of =C-H₂ vibrations above 3000 cm^{-1} . A remaining weak ν_{SiH} demonstrates, that this step of functionalisation does not run completely. The DRIFT spectra of **M4bC₁₁COOH** and **M4aC₄COOH** also show the different extent of surface modification. The carbonyl vibration $\nu_{\text{C=O}}$ at 1714 cm^{-1} is more intense for **M4aC₄COOH** than for **M4bC₁₁COOH** (Figure 4.19). Coupling of the Ln(III) complexes is verified by the amide vibrations ($\nu_{\text{NHC=O}}$ and δ_{NH}) observed at 1700 to 1560 cm^{-1} and a further increase of the intensity of ν_{CH_x} (Figure 4.20). As the Ln(III) complex contains C=O groups as well, DRIFT spectra do not provide the information, if the coupling reaction runs to completion.

Table 4.18 Assignments of IR vibrations of **M3/4C₄₍₁₁₎COOH** and **M3/4C₄₍₁₁₎[Ln-HA]**.

wave number / cm^{-1}				assignment
M4C₄₍₁₁₎COOH	M3C₄₍₁₁₎COOH	M4C₄₍₁₁₎ [Y-HA]	M3C₄₍₁₁₎ [Gd-HA]	
3740 - 3032	3760 - 3006	3745 - 3041	3753 - 3012	different ν (OH)
2939, 2871	2963, 2936, 2872	2928, 2857	2964, 2934, 2863	ν (CH _x)
2287 (w)	2256 (w)	2287 (w)	2256 (w)	ν (Si-H)
1991, 1866	1991, 1866	1991, 1866	1991, 1866	ν (Si-O-Si)
1714	1709		1728	ν (C=O)
		1680 - 1573	1682 - 1573	ν (NHC=O)
1350 - 907	1350 - 907 (1350 - 993) ^{a)}	1350 - 907	1350 - 907 (1350 - 993) ^{b)}	ν_{as} (Si-O-Si) (skeleton)

^{a)} **M3₅₀C₄COOH**, ^{b)} **M3₅₀C₄[Gd-HA]**

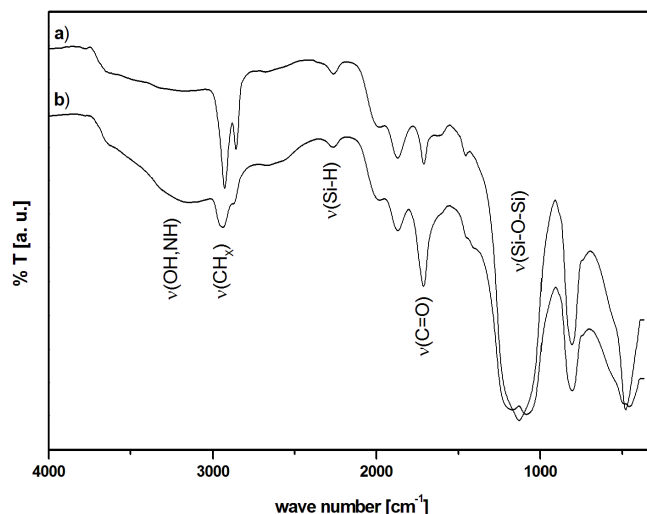


Figure 4.19 DRIFT spectra of a) M4bC₁₁COOH and b) M4aC₄COOH.

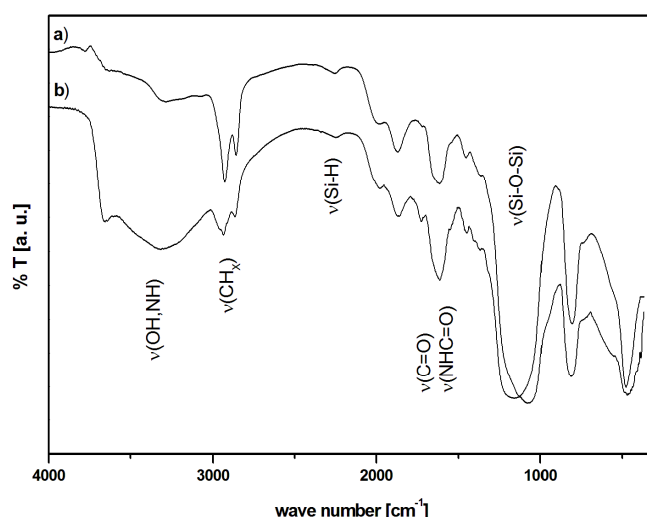


Figure 4.20 DRIFT spectra of a) M4bC₁₁[Y-HA] and b) M3aC₄[Gd-HA].

Solid State NMR Spectroscopy. The ¹³C CP/MAS NMR spectra verify that the coupling of the spacer to the surface and the Ln(III) complex to the spacer has been successful (Figure 4.21, Figure 4.22). Signals due to the alkyl chain and the carbonyl group of the spacer can be observed from 7 to 60 ppm and at 181 ppm, respectively, in the ¹³C NMR spectra of M4C₄₍₁₁₎COOH (Figure 4.21). As expected, the ratio of the signal intensities of the carbonyl resonance to the alkyl resonance is bigger for the C₄ acid than for the C₁₁ acid modified material. The ¹³C NMR spectra of M3C₄[Y-HA] and M4C₁₁[Y-HA] (Figure 4.22) give

evidence for the successful coupling by additional signals of the alkyl groups of the ligand at 57 and 69 ppm, respectively, as well as the carbonyl groups at 182 and the amide carbon at 191 ppm.

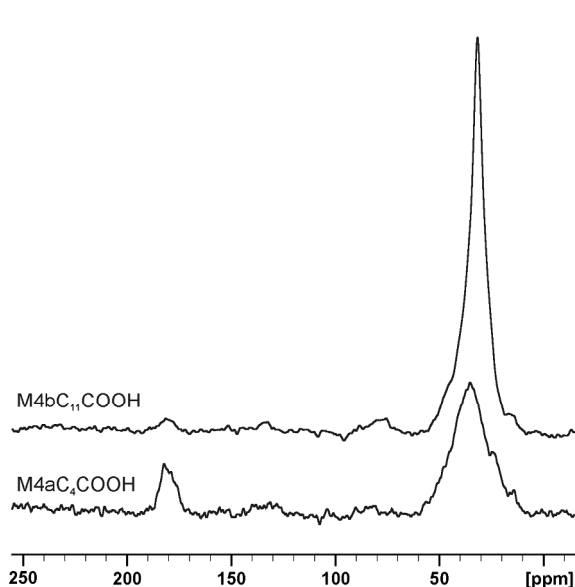


Figure 4.21 ^{13}C CP/MAS spectra of $\text{M4aC}_4\text{COOH}$ and $\text{M4bC}_{11}\text{COOH}$.

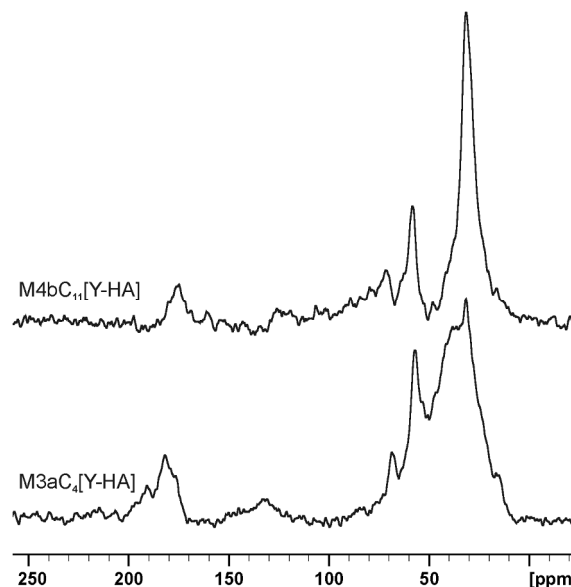


Figure 4.22 ^{13}C CP/MAS spectra of $\text{M3aC}_4[\text{Y-HA}]$ and $\text{M4bC}_{11}[\text{Y-HA}]$.

4.5.2.4 Specific Surface Concentration of Functional Groups

The extent of surface functionalisation of the acid and Gd(III) complex modified materials was quantified by means of elemental analysis (EA) and thermogravimetry (TG) experiments.

TG experiments. TG curves of **M0a** (Figure 4.23, light grey) and the **M3** materials (Figure 4.23, grey) indicate, that desorption of physically adsorbed water is completed at about 130 °C. For **M0a** the following broad region of weight loss is due to dehydroxylation processes, where water and ethanol are removed, and siloxane bonds are formed on the surface. The weight loss of the **M4** materials (Figure 4.23, black) in the low temperature region (up to 130 °C) is negligible, as **M4SiH** already has been treated at 1000 °C. From 130 °C to about 550-600 °C curves of all further functionalised materials show a significant weight loss, due to desorption of the organic moieties, which were coupled to the surface. While the weight loss of the **M4** materials is completed at 600 °C, the broad regions of weight loss from 600 to 1000 °C indicate the desorption of chemically adsorbed water for the **M3** materials.

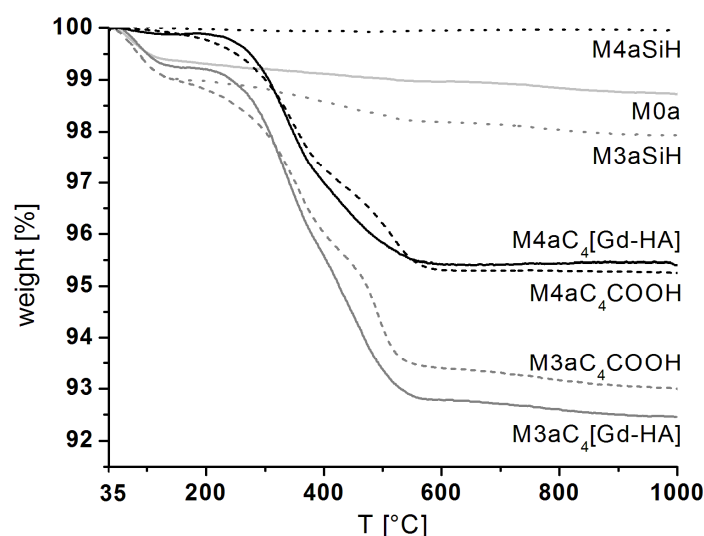


Figure 4.23 Thermogravimetric analyses of the materials: unfunctionalised (**M0a**, light grey), Si-H functionalised (dotted lines), COOH functionalised (dashed lines), and [Gd] functionalised (continuous lines), **M4** series black, **M3** series grey.

Table 4.19 Weight loss of the materials determined by TG measurements from 35 to 1000 °C.

	weight loss / mass-%	corrected weight loss / mass-%
M0a	1.3	
M4aSiH	0	
M4aC₄COOH	4.8	
M4aC₄[Gd-HA]	4.5	
M3aSiH	2.1	0.8 ^{a)}
M3aC₄COOH	6.9	4.8 ^{b)}
M3aC₄[Gd-HA]	7.6	5.5 ^{b)}

^{a)} Measured weight loss of **M3** materials corrected by the value of **M0**.

^{b)} Ratio of Si-H modification subtracted as well.

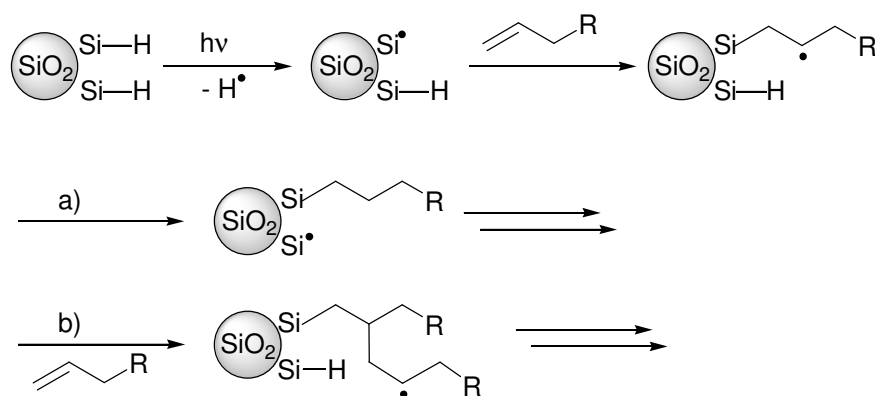
The values of weight loss, given in Table 4.19, directly correlate with the amount of surface modification for the **M4** materials. For the Gd(III) complex functionalised particles **M4aC₄[Gd-HA]**, the weight loss is lower than for the acid modified particles **M4aC₄COOH**, as gadolinium forms oxides and carbonates during the heating of the materials under air, which remain on the surface of the particles, and distort the measure of weight loss. The **M3** materials did not go through the high temperature process for Si-H functionalisation. Therefore, there are still water and ethanol moieties left on the surface, which originate from

M0. Thus, for the **M3** series the weight loss of **M0** has to be subtracted, to achieve the content of surface modification. To get the pure quantity of the spacer and the Gd(III)-complexes, the ratio of Si-H modification was also subtracted from the values, obtained for **M3aC₄COOH** and **M3aC₄[Gd]** (Table 4.19). For the above-mentioned reason, the weight loss for **M3aC₄[Gd-HA]** is only slightly higher than for **M3aC₄COOH**.

Elemental analyses. For the interpretation of the surface concentrations $\Gamma_{(\text{ligand})}$ of the acid modified materials, all values are referred to the surface concentrations $\Gamma_{\text{Si-H}}$ obtained from A_{BET} of the Si-H modified starting materials and given in Table 4.9.

For **M4aC₄COOH**, **M3aC₄COOH**, and **M3₅₀C₄COOH** the ratios of $\alpha_{(\text{ligand})}/\alpha_{\text{OH}}$ are with 2.54, 2.02, and 1.30, respectively, all bigger than 1 (Table 4.20), which means that there are more ligands coupled to the surface than Si-H bonds are available. This can be explained by looking at the possible mechanism of the photochemical hydrosilylation reaction (Scheme 4.13). In the first step, a C=C bond is added to the Si-H bond and yields a free radical center on the β -carbon of the addition product. This radical is expected to recombine with a hydrogen radical, generated from another Si-H bond (Scheme 4.13 a), but also can react with a second C=C bond of a free acid, to yield polymers of the acid molecules on the silica surface (telomerisation, Scheme 4.13 b).⁷⁶ However, in this way stable covalent Si-C and C-C bonds are formed which resist hydrolysis. For **M3bC₁₁COOH** the ratio of $\alpha_{(\text{ligand})}/\alpha_{\text{OH}} = 0.47$ confirms a lower extent of surface modification with the C₁₁ spacer. This is also seen in the DRIFT spectrum for **M4bC₁₁COOH** (Figure 4.19), so the telomerisation reaction is more in favor for the C₄ acid. As this reaction leads to a larger amount of functional groups on the particle surface, which can be further functionalised, the use of this shorter linker allows to increase the Gd(III) concentration per particle.

As the combustion of the Gd(III) complex functionalised materials is not complete, because of the formation of carbonates, the content of carbon could not be determined correctly by EA. Therefore, the data of the measurements of those materials cannot be further evaluated reasonably.



Scheme 4.13 Possible mechanism for radical based hydrosilylation on the silica surface, a) common reaction channel, b) side reaction (telomerisation).

Table 4.20 Evaluation of elemental analyses based on % of carbon (%C).

material	$A_{\text{BET}} / \text{m}^2 \text{g}^{-1}$	%C (EA)	corr %C (EA)	$\Gamma_{\text{(ligand)}} / \text{mmol g}^{-1}$	$\alpha_{\text{ligand}} / \text{nm}^{-2}$	$\alpha_{\text{(ligand)}} / \alpha_{\text{OH}}$
M0a	43	0.18				
M4aSiH	31	0.06				
M4aC₄COOH		3.12	3.06	0.64	12.45	2.54
M3aSiH	38	0.30	0.12			
M3aC₄COOH		3.31	3.01	0.63	9.9	2.02
M0₅₀	104	2.05 ^{a)}				
M3₅₀SiH	91	2.10	0.05			
M3₅₀C₄COOH		6.71	4.61	0.96	6.36	1.30
M0b	49	1.48 ^{a)}				
M3bSiH	40	2.14	0.66			
M3bC₁₁COOH		4.15	2.01	0.15	2.28	0.47

^{a)} higher percentage of carbon as **M0b** and **M0₅₀** were not dried at 600 °C.

4.5.2.5 Specific Surface Concentration of Gadolinium

Surface concentrations $\Gamma_{\text{Gd(III)}}$ of Gd(III) were determined by measurements of the longitudinal relaxation time T_1 by inversion recovery experiments, and confirmed by measurements with an ICP-atomic emission spectrometer (ICP-AES). The Obtained results from the two different methods do not differ significantly (Table 4.21). The highest total

amount of Gd(III) was achieved with the 50 nm particles **M3₅₀C₄[Gd-HA]** (83 $\mu\text{mol g}^{-1}$), followed by the C₄ spacer modified materials (45 and 50 $\mu\text{mol g}^{-1}$ for **M4aC₄[Gd-HA]** and **M3aC₄[Gd-HA]**, respectively). The C₁₁ acid modified material **M3bC₁₁[Gd-HA]** could be loaded with only 16 $\mu\text{mol g}^{-1}$ Gd(III). Related to the total amount of silanol groups available on the surface of **M0a** the highest extents of Gd(III) coverage of 13 and 14% have been achieved for **M4aC₄[Gd-HA]** and **M3aC₄[Gd-HA]**, where 254 and 202%, respectively, would have been possible due to surface coverage with acid groups. In comparison, for the C₁₁ modified NPs **M3bC₁₁[Gd-HA]** only 4% of Gd(III) modification have been achieved, but here just 47% would have been possible due to the acid groups available. For **M3₅₀C₄[Gd-HA]** 10% Gd(III) coverage have been obtained, where 130% could have been possible (compare Table 4.20).

Table 4.21 Gadolinium content $\Gamma_{\text{Gd(III)}}$ of [Gd] functionalised materials **M3** and **M4**.

material	$\Gamma_{\text{Gd(III)}} / \mu\text{mol g}^{-1}$		$\alpha_{\text{Gd}}/\alpha_{\text{OH}} / \% \text{ }^{\text{a}}$
	from ICP	from T ₁ -measurements	
M4aC₄[Gd-HA]	43	45	13
M3aC₄[Gd-HA]	48	50	14
M3₅₀C₄[Gd-HA]	-	83	10
M3bC₁₁[Gd-HA]	15	16	4

^{a)} α_{Gd} derived from T₁-measurements.

Steric considerations for the **M3** and **M4** materials show that the space available on the particles' surface is very well exploited for the C₄ modified materials (69 and 59%), followed by the small particles (43%), while only 20% of the room available is taken in the case of the poorly loaded C₁₁ material (Table 4.22).

Table 4.22 Number of gadolinium complexes per NP of **M3** and **M4** materials.

material	$A_{\text{geo}} / \text{m}^2 \text{ }^{\text{a}}$	$n_{\text{Gd,geo}}$ per NP	n_{Gd} per NP	$n_{\text{Gd}}/n_{\text{Gd,geo}} / \% \text{ }$
M4aC₄[Gd-HA]	3.6×10^{-14}	44.100	31.646	69
M3aC₄[Gd-HA]	3.5×10^{-14}	53.824	26.007	59
M3₅₀C₄[Gd-HA]	9.2×10^{-15}	11.664	5.043	43
M3bC₁₁[Gd-HA]	4.2×10^{-14}	45.796	10.691	20

^{a)} Calculated from d_{SEM} of the materials (Table 4.16).

4.5.2.6 Stability under Physiological Conditions

To test the stability of the [Gd] functionalised materials under physiological conditions, materials **M4aC₄[Gd-HA]**, **M3aC₄[Gd-HA]**, and **M3bC₁₁[Gd-HA]** were stirred in PBS at 37 °C for 12 days. Every 48 (144) hours samples were taken and tested for free Gd(III) by means of the xylenol-test⁷⁷ and the Gd(III) content of the materials was determined by T₁-measurements and ICP-AES. For all samples the xylenol-test was negative, i.e. no Gd(III) is released from the macrocyclic ligand under the applied conditions. For **M3bC₁₁[Gd-HA]** $\Gamma_{\text{Gd(III)}}$ is not decreasing to an observable extent, so the amide bonds between spacer and Gd(III)-complexes as well as the Si-C bonds and the siloxane bonds of the **M3** series on the particle surface are stable under the applied conditions for at least twelve days (Table 4.23). $\Gamma_{\text{Gd(III)}}$ of the higher loaded materials is decreasing by 16% for **M3aC₄[Gd-HA]** and 20% for **M4aC₄[Gd-HA]**. DRIFT spectra of those materials (not depicted) show that the intensity of the amide vibrations decreases as well after 144 h. However, no conclusion can be drawn which chemical bond is cleaved. These results indicate that a certain amount of the Gd(III) complexes is cleaved, but no Gd(III) is released from the macrocycle. Thus, these higher loaded materials can be used without any concerns about Gd-toxicity even *in vivo*, as small, cleaved off Gd(III) complexes would quickly undergo renal clearance. The C₄ materials still contain higher payloads of Gd(III), even after 12 days, and therefore are preferable to the C₁₁ materials.

Table 4.23 Gadolinium content $\Gamma_{\text{Gd(III)}}$ during the stability tests.

time of exposure / h	$\Gamma_{\text{Gd(III)}} / \mu\text{mol g}^{-1}$				
	0	48	96	144	288
M4aC₄[Gd-HA]	45	40	39	36	36
M3aC₄[Gd-HA]	50	47	47	46	42
M3bC₁₁[Gd-HA]	16	-	-	17	17

Values given are obtained from T₁-measurements and were confirmed by ICP-AES.

4.6 Magnetic Resonance Imaging of Gd(III) modified NP Containing Agar Phantoms

MRI experiments were performed in 1.5% agar to stabilise the dispersion of the material throughout the overnight measurement. For this purpose, various dilutions were prepared from a well dispersed stock of 10 mg mL⁻¹ in water and medium +10% serum, respectively. Serum containing cell culture medium (Dulbecco's Modified Eagle Medium (DMEM)) is

used to mimic physiological conditions. Samples were immediately mixed with 1.5% agar (1:1, v/v), gelled in ice, and afterwards pellets were overlaid with water or medium. These samples were measured in a clinical MR scanner at 123 MHz (3 T) and room temperature. Longitudinal and transverse relaxation rates were determined in axial slices of 1 mm thickness through the sample containing agar layer, as well as the supernatant. In addition, sagittal as well as axial T_1 -weighted MR images were made with a spatial resolution typical for *in vivo* experiments at 3 T.

Figure 4.24 displays the concentration-dependent increase of the longitudinal relaxation rate R_1 for **M4aC₄[Gd-HA]** and **M3aC₄[Gd-HA]** in the agar pellet (representative curves of a single experiment). The Gd concentration in the samples was calculated according to the values, given in Table 4.21 (T_1 measurements). The slopes of these curves (determined by linear regression) correspond to the longitudinal relaxivity r_1 (Table 4.24). The transverse relaxivity r_2 can be similarly calculated by fitting the relaxation rates R_2 . No significant change in relaxation rates could be observed in the supernatant slice, which confirms the stability of the materials.

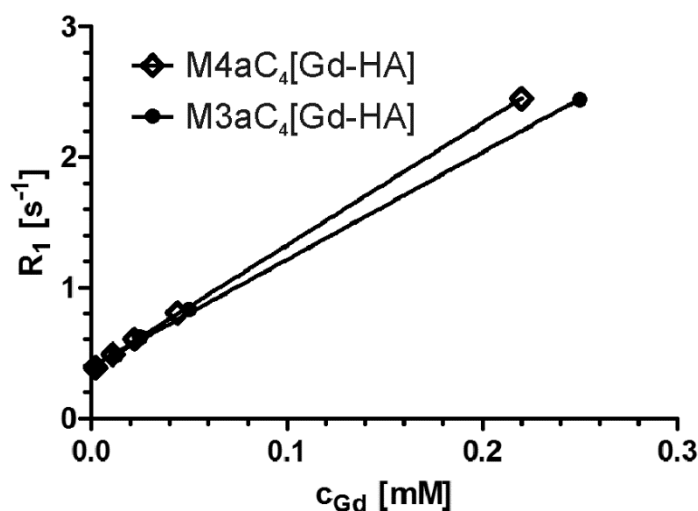


Figure 4.24 Representative curve of the longitudinal relaxation rate R_1 in agar phantoms with various concentrations of **M4aC₄[Gd-HA]** and **M3aC₄[Gd-HA]**.

The concentration-dependent increase of R_1 is also reflected in the T_1 -weighted images, obtained with a common Inversion Recovery-Rapid Acquisition with Relaxation Enhancement (IR-RARE) sequence.⁷⁸ For samples with more than 25 μg of NPs (dispersed in

100 μL agar containing water) a clear contrast enhancement in the agar layer was detectable (Figure 4.25).

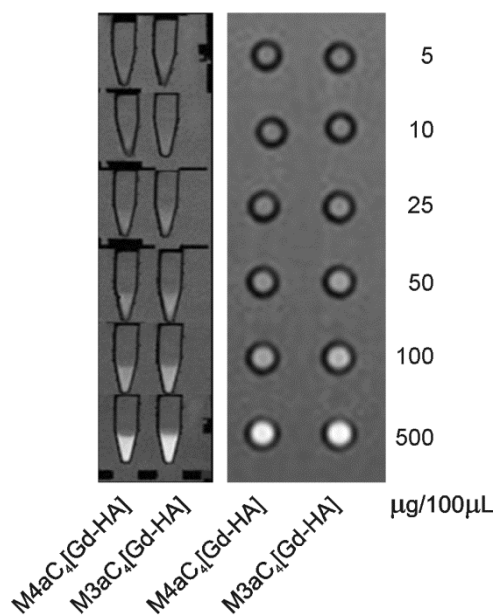


Figure 4.25 Sagittal and axial T_1 -weighted MR images of **M4aC₄[Gd-HA]** and **M3aC₄[Gd-HA]** in aqueous agar phantoms. Given concentrations are μg NPs per 100 μL agar solution corresponding to 2.2 - 220 $\mu\text{mol L}^{-1}$ for **M4aC₄[Gd-HA]** and 2.5 - 250 $\mu\text{mol L}^{-1}$ Gd for **M3aC₄[Gd-HA]**.

At a field strength of 3 T, the longitudinal relaxivities in water and medium of the materials **M4aC₄[Gd-HA]** ($r_1 = 8.8 \text{ mM}^{-1}\text{s}^{-1}$ and $r_1 = 6.4 \text{ mM}^{-1}\text{s}^{-1}$) and **M3aC₄[Gd-HA]** ($r_1 = 8.4 \text{ mM}^{-1}\text{s}^{-1}$ and $r_1 = 6.0 \text{ mM}^{-1}\text{s}^{-1}$) are increased by 47-54% and 100-113% in comparison to r_1 of the single complex Gd[DO3A-HA] ($r_1 = 5.7 \text{ mM}^{-1}\text{s}^{-1}$ and $r_1 = 3.0 \text{ mM}^{-1}\text{s}^{-1}$). Yet, in medium the values of r_1 of the particles, as well as of the single complex are 27-47% lower than in water. This effect is caused³ by interactions of CO_3^{2-} and PO_4^{3-} ions with the Gd(III) chelates of DO3A-like structure, which lead to reduced interactions between water and Gd(III).^{79,80}

By increasing the rotational correlation time τ_R of Gd(III) based CAs, their relaxivity can be improved.^{3,58} This is realised by immobilisation of the Gd(III) complexes on the silica surface. However, there are still high local rotational dynamics of the DO3A ligand possible, most likely due to the flexible hexylamine linker. Despite the slow global rotational dynamics of the particle, this leads to a less effective influence on the relaxivity. The longitudinal relaxivity might be increased by making the linker to the macrocycle more rigid e.g. by using an aromatic linker.⁶⁰ Moreover the τ_R effect strongly depends on the field strength, as can be seen in NMRD profiles of Gd chelates anchored to silica NPs.^{19,20} At 123 MHz the influence of τ_R on r_1 and thus, the difference between surface-bound and free Gd chelates is already strongly reduced compared to e.g. 20 MHz.

Table 4.24 Longitudinal and transverse relaxivity r_1 and r_2 of Gd(III) modified materials at 3T and room temperature.

material	fluid	Relaxivity per mM Gd		
		$r_1 / \text{mM}^{-1}\text{s}^{-1}$	$\Delta r_1 / \%$ ^{b)}	$r_2 / \text{mM}^{-1}\text{s}^{-1}$
M1C₃[Gd-BA]	water	13.3 ± 0.4	75	51.6 ± 24.6
M1C₃[Gd-GA]	water	13.1 ± 2.1	236	46.1 ± 0.8
M2[Gd-HA]	water	30.6 ± 1.9	437	74.7 ± 17.4
M3aC₄[Gd-HA]	water	8.4 ± 1.1	47	44.1 ± 3.4
M3bC₁₁[Gd-HA]	water	6.3 ± 1.1	11	51.0 ± 10.8
M3₅₀C₄[Gd-HA]	water	15.4 ± 1.5	170	52.7 ± 18.6
M4aC₄[Gd-HA]	water	8.8 ± 1.3	54	47.8 ± 6.7
Gd[DOTA-BA]	water	7.6 ± 0.3		10.5 ± 0.3
Gd[DOTA-GA]	water	3.9 ± 0.1		4.2 ± 0.0
Gd[DO3A-HA]	water	5.7 ± 1.2		12.0 ± 1.3
M1C₃[Gd-BA]	medium ^{a)}	8.5 ± 1.7	85	51.4
M1C₃[Gd-GA]	medium ^{a)}	11.7 ± 0.6	290	27.0 ± 2.8
M2[Gd-HA]	medium ^{a)}	5.2 ± 1.1	73	51.3 ± 33.4
M3aC₄[Gd-HA]	medium ^{a)}	6.0 ± 1.9	100	38.2 ± 8.8
M3bC₁₁[Gd-HA]	medium ^{a)}	6.3 ± 0.1	110	29.8 ± 0.2
M3₅₀C₄[Gd-HA]	medium ^{a)}	5.5 ± 1.1	83	34.6 ± 11.6
M4aC₄[Gd-HA]	medium ^{a)}	6.4 ± 0.7	113	50.2 ± 4.9
Gd[DOTA-BA]	medium ^{a)}	4.6 ± 0.7		7.1 ± 1.4
Gd[DOTA-GA]	medium ^{a)}	3.0 ± 0.1		3.9 ± 0.5
Gd[DO3A-HA]	medium ^{a)}	3.0 ± 0.3		5.1 ± 1.5

Values represent mean ± SD, n=2-7.

^{a)} Cell culture medium + 10% serum.

^{b)} Δr_1 is the increase of the longitudinal relaxivity compared to the respective single complex.

The longitudinal relaxivities of the C₁₁ modified material **M3bC₁₁[Gd-HA]** ($r_1 = 6.3 \text{ mM}^{-1}\text{s}^{-1}$ and $r_1 = 6.3 \text{ mM}^{-1}\text{s}^{-1}$ in water and medium, respectively) are increased by 11% and 110% in comparison to r_1 of Gd[DO3A-HA]. As discussed above, the little increase of r_1 in water indicates a less effective influence on the relaxivity because of the longer linker. Another reason for the decreased r_1 value in comparison to the C₄ materials is the agglomeration behaviour of the C₁₁ material. As **M3bC₁₁[Gd-HA]** forms larger agglomerates, access to the Gd sites might be hindered more than in the case of the C₄ materials.

The r_1 value of **M3₅₀C₄[Gd-HA]** in water ($r_1 = 15.4 \text{ mM}^{-1}\text{s}^{-1}$) is increased by 170% and thus stronger influenced as r_1 of the bigger particles, while in medium r_1 is only increased by 83% ($r_1 = 5.5 \text{ mM}^{-1}\text{s}^{-1}$), which is less than for the bigger particles.

The strongest influence on both, r_1 and r_2 , is observed for **M2[Gd-HA]** in water. The longitudinal relaxivity is increased by more than 400% ($r_1 = 30.6 \text{ mM}^{-1}\text{s}^{-1}$). Origins for the large increase of r_1 might be an improved water exchange rate or a decreased flexibility, due to the nature of the linker (compare Scheme 4.9). Yet, in medium the observed increase of r_1 by 73% is poor.

For all Gd[DO3A-HA] modified materials, the longitudinal relaxivities in medium are very similar ($5.2 - 6.4 \text{ mM}^{-1}\text{s}^{-1}$), so as already observed by the zetapotential measurements (compare 4.5.2.2), differences between the materials are compensated in medium.

The longitudinal relaxivity r_1 of the DOTA derivative Gd[DOTA-GA] in water ($r_1 = 3.9 \text{ mM}^{-1}\text{s}^{-1}$) is lower than r_1 of Gd[DO3A-HA]. Due to the additional carboxylic acid function of the ligand there is one coordination site less for water molecules, which leads to a decrease in relaxivity. The advantage of this DOTA derivative is that its r_1 is only decreased by 18% in medium.

The r_1 value of Gd[DOTA-BA] in water ($r_1 = 7.6 \text{ mM}^{-1}\text{s}^{-1}$) is increased in comparison to r_1 of Gd[DOTA-GA] and even higher than for Gd[DO3A-HA]. This might be up to an increased rotational correlation time τ_R due to the aromatic linker or to an increased amount of water bound to the Gd^{3+} . The interactions of the carboxylate next to the benzyl might be hindered due to the rigidity of the system. This would also explain the stronger decrease of r_1 in medium.

The longitudinal relaxivity values of the materials **M1C₃[Gd-BA]** and **M1C₃[Gd-GA]** in water ($r_1 = 13.3$ and $13.1 \text{ mM}^{-1}\text{s}^{-1}$, respectively) are comparable and increased in comparison to the single complexes. In medium r_1 of **M1C₃[Gd-BA]** is clearly decreased, whereas r_1 of **M1C₃[Gd-GA]** is only slightly decreased. Both materials show higher longitudinal relaxivities in medium than the materials with the DO3A derivative, which makes them more suitable as CA for *in vivo* applications.

The transverse relaxivities r_2 of all materials is significantly increased in comparison to r_2 of the respective single complexes in water, as well as in medium. So immobilisation of the Gd(III) complexes on the particles' surface causes a strong increase of r_2 . However, the increase is not too big and does not disturb measurements of T_1 -weighted images due to a too strong shortening of T_2 . In medium r_2 values are not as much decreased as r_1 values. All r_2

values are in the same range of magnitude and no dependency on the particle size is observable.

Although the longitudinal relaxivity per Gd of the materials is not significantly increased, the high number of Gd(III) per particle leads to remarkably high relaxivities per particle (up to $r_1 = 6.18 \times 10^5 \text{ mM}^{-1} \text{ s}^{-1}$ and $r_2 = 2.40 \times 10^6 \text{ mM}^{-1} \text{ s}^{-1}$ for **M1C₃[Gd-BA]** e.g.; compare Table 4.25). These relaxivity values are comparable with those obtained for luminescent hybrid nanoparticles¹⁴ and mesoporous silica particles.^{13,19,20} Thus, CA functionalised silica NPs with high local relaxivities were successfully synthesised.

Table 4.25 Longitudinal and transverse relaxivity r_1 and r_2 per NP.

material	fluid	number of Gd per NP	relaxivity per mM NP	
			$r_1 / \text{mM}^{-1} \text{s}^{-1}$	$r_2 / \text{mM}^{-1} \text{s}^{-1}$
M1C₃[Gd-BA]	water	46434	6.18×10^5	2.40×10^6
M1C₃[Gd-GA]	water	15023	1.97×10^5	6.93×10^5
M2[Gd-HA]	water	16452	5.03×10^5	1.23×10^6
M3aC₄[Gd-HA]	water	26007	2.18×10^5	1.15×10^6
M3bC₁₁[Gd-HA]	water	10691	6.74×10^4	5.45×10^5
M3₅₀C₄[Gd-HA]	water	5043	7.77×10^4	2.66×10^5
M4aC₄[Gd-HA]	water	31646	2.78×10^5	1.51×10^6
M1C₃[Gd-BA]	medium ^{a)}	46434	3.95×10^5	2.39×10^6
M1C₃[Gd-GA]	medium ^{a)}	15023	1.76×10^5	4.06×10^5
M2[Gd-HA]	medium ^{a)}	16452	8.55×10^4	8.44×10^5
M3aC₄[Gd-HA]	medium ^{a)}	26007	1.56×10^5	9.93×10^5
M3bC₁₁[Gd-HA]	medium ^{a)}	10691	6.74×10^4	3.19×10^5
M3₅₀C₄[Gd-HA]	medium ^{a)}	5043	2.77×10^4	1.74×10^5
M4aC₄[Gd-HA]	medium ^{a)}	31646	2.03×10^5	1.59×10^6

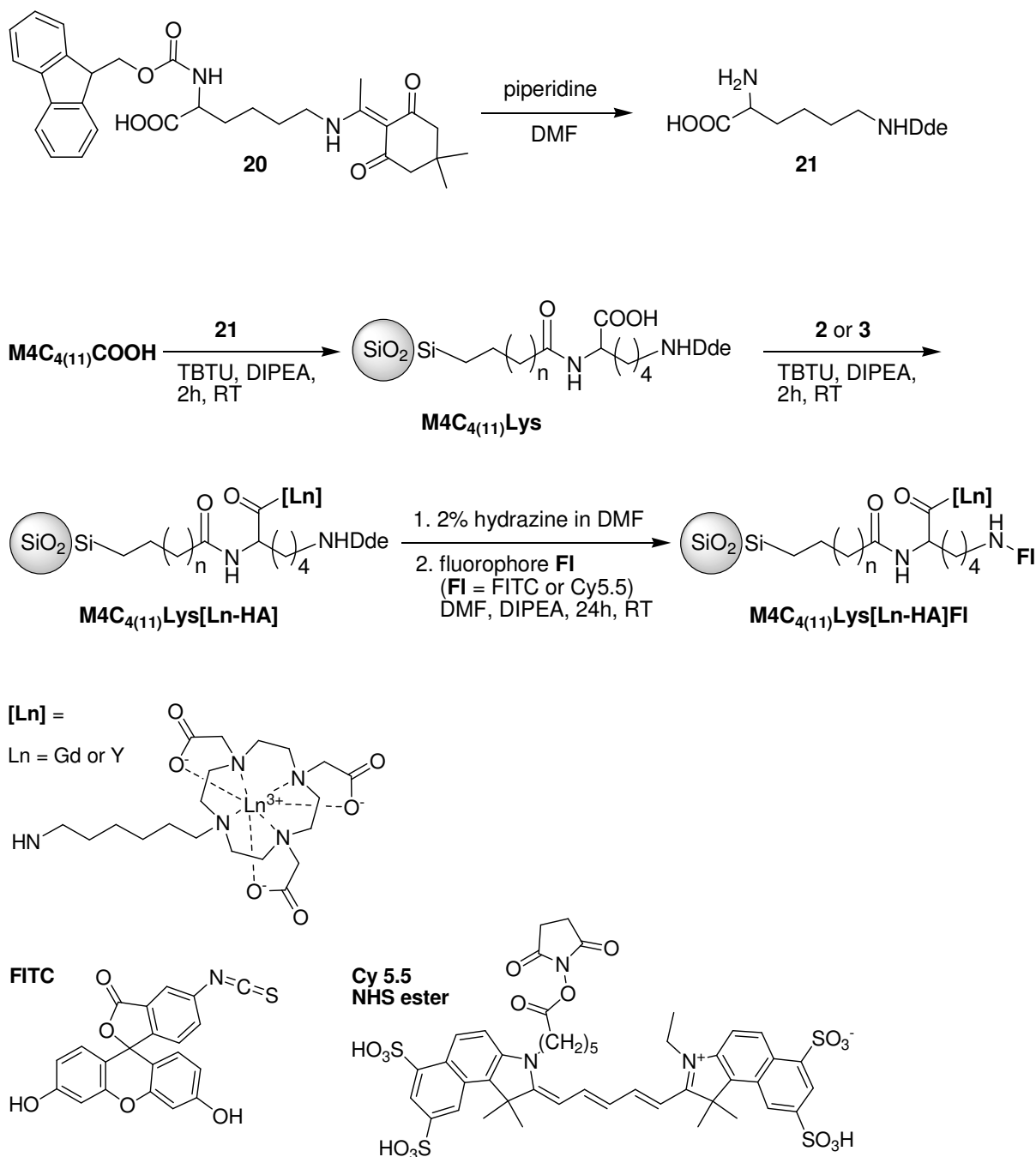
^{a)} Cell culture medium + 10% serum.

4.7 Multifunctionality

The interactions of NPs with cells play key roles in executing their biomedical functions and their toxicity. Thus, the design of new biomedical functions and the prediction of the toxicological properties of NPs *in vivo* require knowledge of the interactions of the NPs with the target cells. Issues to consider are the cellular uptake, location and biological consequences, such as cytotoxicity of the NPs. There are many parameters influencing these interactions, like the size and shape, composition, charge, and surface chemistry of the NPs.⁸¹ The use of imaging tools to probe NP-cell interactions is crucial to elucidating the mechanisms of NP induced toxicity. Of particular interest are mechanisms associated with cell penetration, translocation and subsequent accumulation inside the cell, or in cellular compartments.⁸² Fluorescence microscopy is currently one of the most powerful and versatile techniques available for biological studies. The technique uses fluorophores which have large absorption cross-sections at a specific wavelength and emit light at a longer wavelength. With fluorophore labeled NPs it is possible to image localisation of the NPs in living cells.⁸³ To study the biological properties of the CA modified NPs, fluorophores were additionally coupled to the surface of the NPs.

4.7.1 Syntheses of Bimodal Silica Particles

Bimodal NPs were synthesised starting from **M4C₄COOH** and **M4C₁₁COOH**. The biprotected lysine derivative *N*_α-Fmoc-*N*_ω-Dde-D-lysine was used as a bifunctional linker. First the Fmoc protecting group was cleaved and the lysine derivative was coupled to the particle surface with its α-amino group by means of the coupling agent TBTU and DIPEA. After binding of Gd[DO3A-HA] **3** to the carboxylic acid group of the lysine, the ω-amino group was deprotected to allow further functionalisation. The fluorescent dyes FITC and Cy.5.5, respectively, were finally coupled to allow optical imaging (OI) in *in vitro* cell studies (Scheme 4.14).



Scheme 4.14 Synthesis of bimodal NPs.

4.7.2 Characterisation and Examination of Bimodal NPs

4.7.2.1 Specific Surface Concentration of Gadolinium

The Gd(III) content of the bimodal NPs was determined after coupling of the Gd(III) complexes, but before coupling of the fluorophores. The fluorophores are very expensive and too big amounts of material are needed for the determination of Gd(III).

Table 4.26 Gadolinium content $\Gamma_{\text{Gd(III)}}$ of **M4C₄₍₁₁₎Lys[Gd-HA]**.

material	$\Gamma_{\text{Gd(III)}} / \mu\text{mol g}^{-1}$	$\alpha_{\text{Gd}}/\alpha_{\text{OH}} / \%$
M4aC₄Lys[Gd-HA]	21	6
M4bC₁₁Lys[Gd-HA]	11	3

The gadolinium content of the bimodal materials **M4aC₄Lys[Gd-HA]** and **M4bC₁₁Lys[Gd-HA]** (21 and 11 $\mu\text{mol g}^{-1}$, respectively) is lower than $\Gamma_{\text{Gd(III)}}$ of the directly [Gd] modified materials **M4aC₄[Gd-HA]** and **M3bC₁₁[Gd-HA]** (45 and 16 $\mu\text{mol g}^{-1}$, respectively). In the case of **M4aC₄Lys[Gd-HA]** the amount of Gd(III) is strongly decreased, which can be ascribed to sterical hindrance when coupling the lysine spacer to the particle surface. Relating to the total amount of silanol groups available on the unfunctionalised particles' surface a coverage of Gd(III) of 6 and 3%, respectively, has been achieved for the bimodal NPs.

Sterical considerations for the bifunctional materials are more complex than in the previous cases, as they should include the lysine spacer. Therefore, no explicit numbers are given.

4.7.2.2 *in vitro* Cell Studies

FITC functionalised NPs **M4C₄₍₁₁₎Lys[Gd-HA]FITC** were examined by fluorescence microscopy concerning localisation and cellular uptake (Figure 4.26). Green spots are NP agglomerates, blue spots in the left image are cell nuclei. Yellow arrows point to larger extracellular agglomerates, blue arrows point to smaller predominantly intracellular vesicles filled with NPs and located around the cell nuclei.

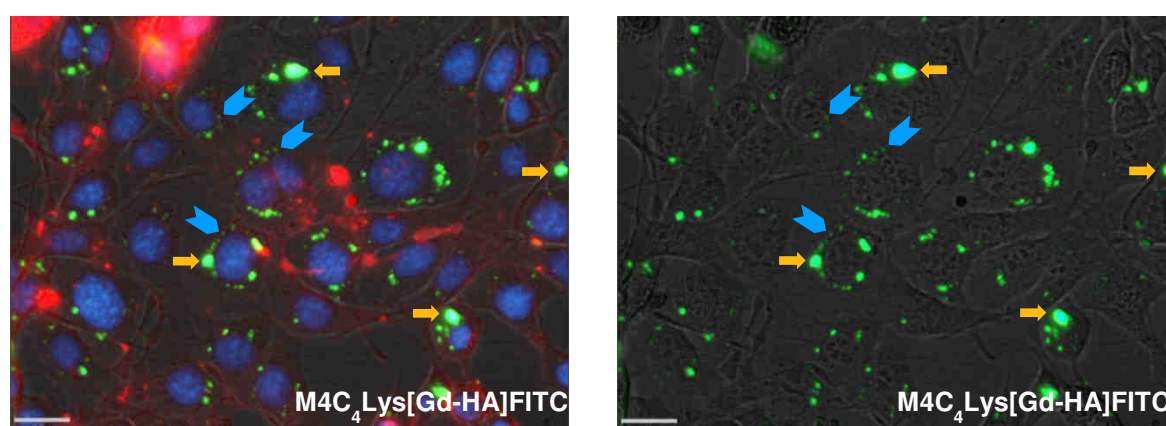


Figure 4.26 Fluorescence images of 3T3 mouse fibroblast cells incubated for 18 h with NPs in cell culture medium ($25 \mu\text{g NP mL}^{-1}$). Cell nuclei were counterstained with the DNA dye Bisbenzimid Hoechst 33342, extracellular fluorescence was quenched by Trypan Blue, and cells were thoroughly washed with HBSS prior to fluorescence microscopy. The bars represent 21 μm .

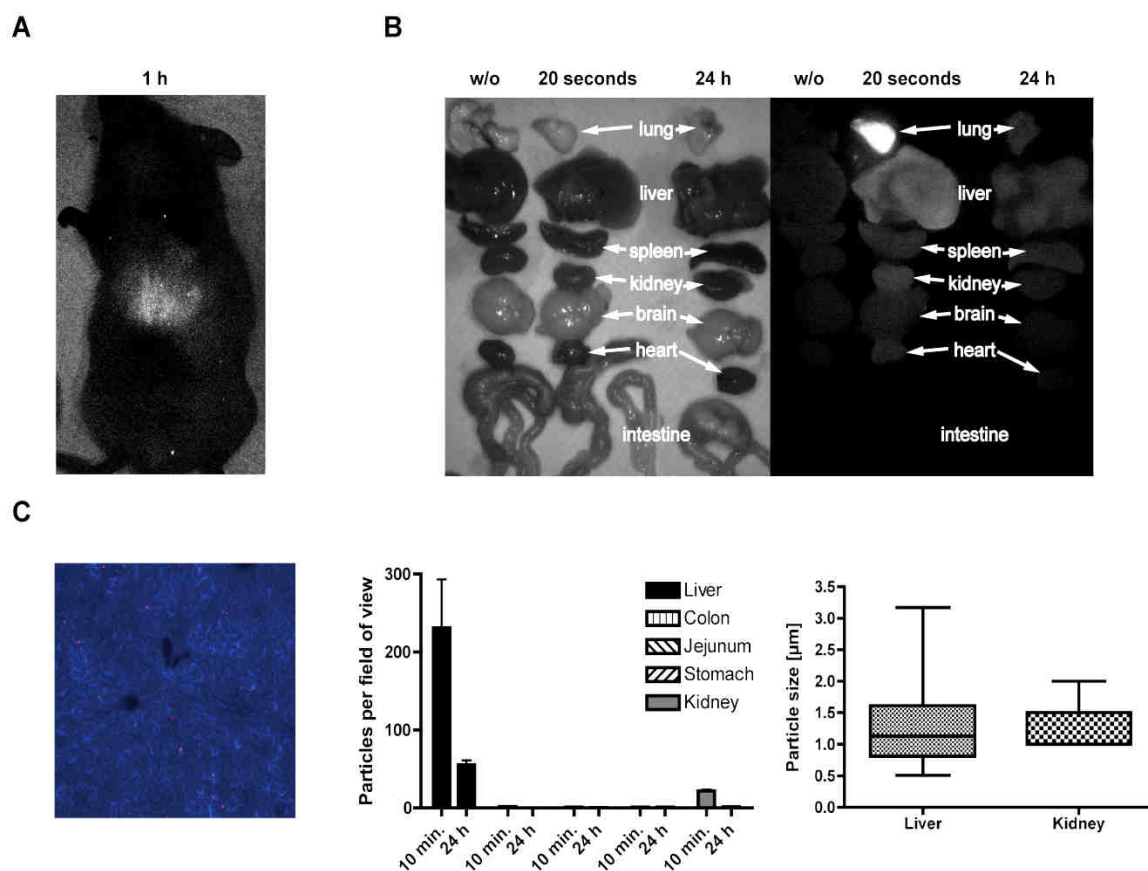
4.7.2.3 *in vivo* Studies

Figure 4.27 A) *In vivo* imaging of anesthetised mice was performed 1 h after injection. B) *Ex vivo* imaging of different organs was performed 20 sec and 24 h after injection. C) Mice received silica NPs *i.v.* and were sacrificed after 10 min or 24 h. Frozen sections of liver, gut, and kidney were analysed by fluorescence microscopy. The left image depicts a 10-fold magnification of a liver section. A red pseudocolor was used for Cy5.5 NPs, a blue pseudocolor was used for liver autofluorescence. Bar graph (middle) depicts silica NPs accumulation within different organs. NP aggregates were counted manually. The box plot (right) displays the size of NP aggregates within liver and kidney (determined from a 40-fold magnification).

To assess biodistribution within different organs Cy5.5 modified NPs **M4aC₄Lys[Gd-HA]Cy5.5** were injected intravenously into BALB/c recipients (0.3 mg / 200 μL / 20 g) and near-infrared fluorescence (NIRF) imaging was performed. After injection, a signal in the upper abdominal quadrants was detected *in vivo* (Figure 4.27 A). *Ex vivo* analysis of different organs revealed rapid accumulation of NPs in lung and liver directly after intravenous injection (Figure 4.27 B). Furthermore, NPs were detected in spleen, kidney, heart, and brain, but not in the intestine. After 24 h, the signal intensity was reduced in lung and liver and no signal was observed in any other organs. To investigate the distribution of the NPs on a

cellular level different organs were analysed by fluorescence microscopy (Figure 4.27 C, left). Quantification of histological sections confirmed the results obtained with NIRF imaging (Figure 4.27 C, middle). Furthermore, histological evaluation revealed aggregate formation within liver and kidney with mean sizes of about 1000 nm (Figure 4.27 C, right). Aggregate formation could be a result of intracellular particle accumulation in cells of the reticuloendothelial system (RES). However, none of the mice that received NPs presented with clinical signs of illness such as breathing problems and none of the mice died (n=5, data not shown).

4.8 Antibody modified Stöber Particles

The endothelium is the thin layer of cells that lines the interior surface of blood vessels. Endothelial cells (ECs) are excellent targets for molecular imaging because they are directly accessible for systemically administered agents. Therefore, targets on ECs can be used for molecular imaging. During the course of inflammatory diseases, such as graft versus host disease (GVHD), endothelial cells become activated and several molecular markers show up-regulated expression within GVHD target organs.⁸⁴ Some of these markers are involved in the multistep process of leucocyte recruitment. Initially, selectins expressed on activated endothelial cells tether leucocytes from the blood stream and induce rolling of leucocytes along the wall. In a next step, leucocytes adhere *via* integrins expressed on leucocytes and CAMs, such as α -VCAM-1 or α -ICAM-1, expressed on activated endothelial cells.^{85,86} The low baseline expression level of α -VCAM-1 or α -ICAM-1 on healthy ECs and its rapid upregulation upon inflammatory stimuli makes it a very attractive target for molecular imaging.⁸⁵ Thus, silica NPs should serve as a matrix to couple the antibodies (ABs) α -VCAM-1 or α -ICAM-1 next to Gd(III) complexes as MR imaging probes for molecular imaging. To develop a strategy for AB coupling and examination of AB coupled NPs, in preliminary experiments only ABs were coupled to the silica NPs **M4aC₄COOH**.

4.8.1 Synthesis

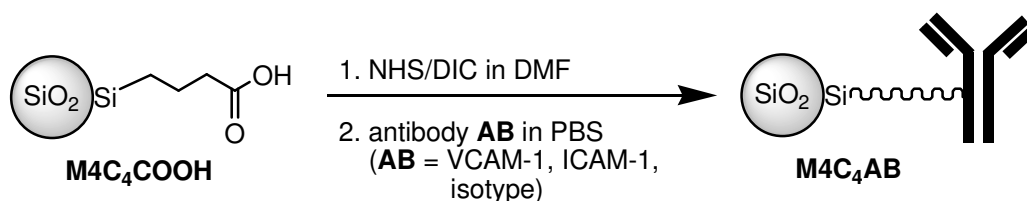
Biomolecules, such as ABs, contain a variety of functional groups, which can be used for coupling to another functional group. A common strategy for coupling ABs to another molecule or matrix is a reaction of amino-groups of the AB with appropriate functional groups of the other molecule or matrix. The primary coupling chemical reactions for modification of amines proceed by acylation and most of these reactions are rapid and occur

in high yield to give stable amide bonds. The most common activation chemistry for creating reactive acylating agents is an *N*-hydroxysuccinimide (NHS) ester. An NHS ester is formed by the reaction of a carboxylate with NHS in the presence of a carbodiimide. A number of standard protocols are well-established in the literature.⁸⁷

The ABs VCAM-1, ICAM-1 and an unspecific isotype control AB were coupled to **M4aC₄COOH**. Different activation strategies and different AB concentrations were examined.

In a first approach, the acid groups were activated with EDC and sulfo-NHS in PBS. The particles were centrifuged and resuspended in PBS (pH 7.4). However, after addition of the AB solutions (ABs in PBS, different AB concentrations (50, 100, 150 µg AB/mL), pH 7.4), flocculation occurred and the precipitate did not dissolve after adjusting pH from 6.5 to 7.1.

In the second approach, the acid groups were activated with DIC and NHS in DMF. The activated NPs were suspended in dry DMF (10 µL) and the ABs, dissolved in PBS were added. Concentrations of 50, 100, and 150 µg AB/mL were examined (Scheme 4.15). With this approach coupling was successful. The resulting materials **M4C₄AB_{VCAM}**, **M4C₄AB_{ICAM}** and **M4C₄AB_{ISO}** were resuspended and stored in PBS (pH 7.4) at 4°C.



Scheme 4.15 Coupling of antibodies to acid modified NPs.

4.8.2 Examination of AB modified NPs

4.8.2.1 Western Blot

The western blot (immunoblot) is a widely used analytical technique to detect proteins in a sample. It applies gel electrophoresis to separate native or denatured proteins by the length of the polypeptide or by the 3-D structure of the protein, respectively. The proteins are then transferred to a membrane (typically nitrocellulose or polyvinylidene fluoride), where they are detected using antibodies specific to the target protein.^{88,89}

The coupling efficacy of the ABs to the NPs was investigated by means of an immunoblot assay to detect the immunoglobulin heavy chain (IgH) of the NP bound antibody. From band

intensities of IgH and respective controls, coupling efficacy and the amount of antibodies bound to the NPs were determined (Figure 4.28 A, B). For the coupling of α -VCAM-1, isotype control, and α -ICAM-1 coupling efficacies of 0.4, 2.4, and 2.8% were determined. (Figure 4.28 A).

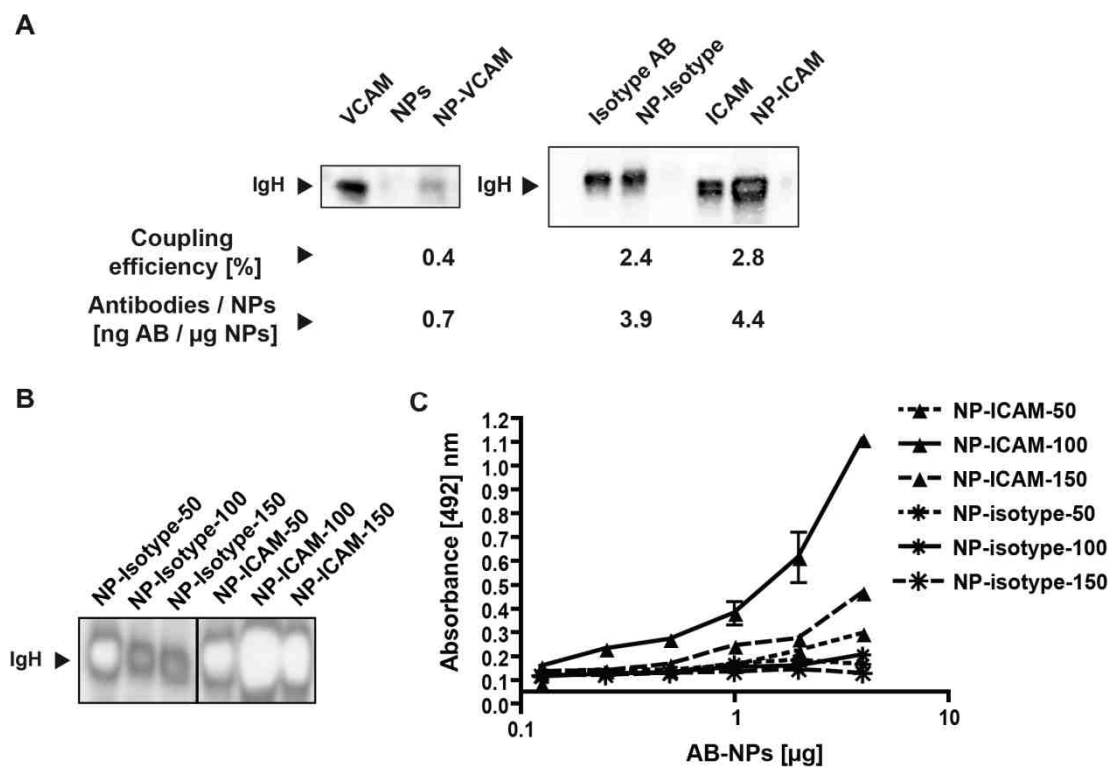


Figure 4.28 A) Left blot: western blot detection of α -VCAM-1 coupled silica NPs. Right blot: western blot detection of isotype and α -ICAM-1 coupled silica NPs. B) Different antibody concentrations used for the coupling reaction. C) ELISA results for quantification of α -ICAM-1 and isotype coupled silica NPs.

4.8.2.2 ELISA

An enzyme-linked immunosorbent assay (ELISA) is a biochemical technique used to detect the presence of an antibody or an antigen in a sample.⁹⁰

To test for antigen-specific binding, an ELISA-based assay that mimics turbulent flow conditions was established. Recombinant VCAM-1 or ICAM-1 proteins were immobilised on ELISA plates and the coated plates were incubated with α -VCAM-1, α -ICAM-1, or isotype coupled NPs in serial dilutions. After washing (using a vortexer), isotype coupled NPs were removed from the plate surface whereas α -ICAM-1 or α -VCAM-1 coupled NPs remained attached. To quantify particle binding a horseradish peroxidase (HRP) conjugated secondary

antibody was used for detection (Figure 4.28 C). As expected, for the isotype coupled NPs, no signals could be observed, whereas the signals detected for the α -ICAM-1 coupled NPs correlate nicely with the coupling efficacy determined in the western blot (Figure 4.28 B). The particles reacted with an AB solution of 100 μ g/mL give the brightest spot in the western blot and the curve with the highest slope in the ELISA detection. As the coupling efficacy of α -VCAM-1 was quite poor, ELISA results are not depicted. These results demonstrate, that ABs were coupled successfully to the silica NPs and that their antigen-specific binding properties are maintained. Thus, silica NPs pose an adequate platform for the synthesis of antibody modified particulate contrast agents. In combination with the results of Gd(III) complex and fluorophore coupling to the NPs, a way to synthesise multimodal contrast agents was established.

5 Conclusion

Nonporous spherical silica NPs with desired diameters in the colloidal range (50-2000nm) can be synthesised by means of the Stöber process. If the critical experimental parameters (concentrations, temperature, chemical identity of the precursor, catalyst, and solvent) are carefully controlled, the diameters of the resulting materials are reproducible within their standard deviations. The surface of the silica particles can be easily modified with functional groups to allow further functionalisation. Silanisation reactions with functional alkoxy silanes and a chlorination reduction reaction were successfully used to introduce amino, epoxy, and Si-H groups, respectively. Si-H groups can be converted into carboxylic acid groups by the addition of terminal unsaturated carboxylic acids. The introduction of Ln(III) complexes by forming peptide bonds with surface modified silica NPs works out fine.

Two different ways of Si-H functionalisation were compared. Interestingly, surface concentrations of Gd(III) chelate complexes and imaging properties of the resulting materials do not differ significantly between the materials, obtained by different ways of Si-H functionalisation. This makes the less complex silanisation with TES the preparation method of choice.

The agglomeration behaviour can be investigated by SEM, DLS and zetapotential measurements. Zeta values of the materials correlate well with their tendency to form agglomerations. Amino functionalised NPs have a positive zetapotential in PBS, all other materials show negative zetapotentials. In cell culture medium + 10% serum, differences in the potentials of the materials are compensated due to interactions with the components of the medium.

The agglomeration behaviour of the particles can be influenced by surface modification. The length of the spacer molecules play an important role and agglomeration can be prevented by introducing short spacers. Here the introduction of a C₄ spacer to **M3SiH** and **M4SiH** improved agglomeration in comparison to a C₁₁ spacer. Another possible reason for the improved agglomeration behaviour is the increased number of carboxylates on the particle surface in the case of the C₄ spacer. Interestingly, the charge of the complexes coupled to the surface plays a minor role and its influence is unpredictable. In the case of **M1C₃[Ln-BA]** and **M1C₃[Ln-GA]**, charged complexes improve agglomeration behaviour of the particles, whereas in the case of **M4C₁₁[Y-ButAm]** agglomeration was worse with the charged complex than in the case of **M4C₁₁[Ln-HA]** with its uncharged complex.

With the C₄ spacer higher Gd(III) surface concentrations were obtained, whereas the C₁₁ spacer leads to more stable materials under physiological conditions. Stability tests for all materials show that no Gd(III) ions are released from the chelates.

Gadolinium surface concentrations of up to 83 $\mu\text{mol g}^{-1}$ were reached, and the materials show the typical concentration-dependent increase of the longitudinal relaxation rate R_1 in a clinical 3 T MR scanner at room temperature. The longitudinal relaxivity values per Gd of the materials are increased in comparison to the uncoupled Gd(III) complex, and the high number of Gd(III) complexes per particle leads to remarkably high relaxivity values of up to $6.18 \times 10^5 \text{ mM}^{-1} \text{ s}^{-1}$ per particle. This is comparable to previously published, mesoporous silica materials. Bimodal NPs for magnetic resonance and optical imaging were successfully synthesised by the introduction of lysine as a bifunctional linker and coupling of fluorophores (FITC or Cy5.5) next to Gd(III) chelates. Finally, antibodies were successfully coupled to the NPs, while their specific interactions with an antigen were maintained.

In conclusion, CA functionalised nonporous silica NPs with a high local relaxivity, bimodal CA and fluorophore modified NPs, and antibody coupled NPs were obtained. These results indicate that this type of silica nanoparticles can pose a platform for the development of highly effective probes for MRI. Further functionalisation allows the synthesis of multimodal and/or targeted contrast agents for molecular imaging applications.

6 Experimental Part

6.1 Syntheses of the Lanthanide Complexes

6.1.1 Solvents and Reagents

All reagents were used without further purification, unless otherwise mentioned.

1,4,7,10-tetraazacyclododecane (cyclen, 98%) was purchased from CheMatech. Acetonitrile (extra dry, over molecular sieves, water <50 ppm) and *tert*-butyl bromoacetate (99%) were bought from Acros Organics. N_ω-Z-L-lysine (≥99.0%), YCl₃×6H₂O, Chelex 100, and xylenol orange were purchased from Sigma-Aldrich, HBr (48%) from Fluka, GdCl₃ hydrate (99,99%) from Chempur, palladium on charcoal (Pd/C, 10% Pa) from Merck. H₂ 5.0 and Ar 5.0 were used. Methanol was dried over magnesium. DO3A-hexylamine (DO3A-HA) was kindly provided by Dr. I. Mamedov, Max-Planck-Institute for Biological Cybernetics, Tübingen. All reagents not mentioned were obtained from the chemicals store at the University of Tuebingen.

The lanthanide(III) chloride stock solutions were prepared by dissolving the chloride salt in distilled water. The exact concentration was determined *via* complexometric titration with the disodium salt of EDTA in an acetic acid / sodium acetate buffer (pH 5.8) using xylenol orange as indicator.

6.1.2 Analytical methods

Mass Spectrometry. ESI mass spectra were recorded on a Bruker Daltonics esquire3000plus mass spectrometer (quadrupolar ion-trap) with an ESI interface. FAB spectra were recorded on a Finnigan Triple-Stage-Quadrupol Spectrometer (TSQ-70) from Finnigan-Mat.

Solution NMR Spectroscopy. ¹H and ¹³C{¹H} NMR spectra were recorded on a Bruker Avance II 400 MHz or a Bruker Avance II+ 500 MHz spectrometer at 26 °C, unless otherwise mentioned. ¹H and ¹³C resonances were assigned using standard 2D techniques (¹H-¹H COSY, ¹H-¹³C HSQC, ¹H-¹³C HMBC). The NMR spectra were recorded at the following frequencies: ¹H NMR: 400.13 and 500.13 MHz; ¹³C NMR: 100.61 and 125.76 MHz.

IR Spectroscopy. IR experiments were performed on a Bruker Vertex 70 FTIR Spectrometer. The spectra were recorded with a resolution of 4 cm⁻¹ and 16 scans from 4000 to 500 cm⁻¹ versus pure KBr as blank.

pH Electrode. pH values of the aqueous solutions were measured using a Schott handylab pH12 pH-meter equipped with a Mettler-Toledo Inlab[®] Micro glass electrode.

6.1.3 Syntheses

6.1.3.1 Synthesis of Gd[DO3A-HA] (3)

DO3A-HA (134 mg, 3.0×10^{-4} mol, 1 eq.) was diluted in water (2 mL) and the pH of the solution was adjusted to 6.7 by the addition of aqueous NaOH. Aqueous GdCl₃-solution (664 μ L, 3.3×10^{-4} mol, 1.1 eq.) was added and again the pH of the solution was adjusted to 6.9. Under stirring the solution was heated to 60 °C for 3 h. To remove excess of Gd(III), Chelex 100 was added and stirred for 1 h. The solution was decanted from the cation exchange resin and the water removed under vacuum at 40 °C. The raw product was used without further purification. Absence of free Gd(III) ions was confirmed by the xylenol-test.⁷⁷

MS (ESI) *m/z*: 601.1 ([M+H]⁺), 623.0 ([M+Na]⁺), mol. wt. calculated for C₂₀H₃₆GdN₅O₆: 600.19; **IR** (KBr): $\tilde{\nu}$ = 3662 - 3251 (br, ν (NH)), 2938, 2872 (s, ν (CH₂)), 1694 (m, ν (C=O)), 1621 (m, δ (NH)).

6.1.3.2 Synthesis of Y[DO3A-HA] (2)

The complex was synthesised according to the procedure described for **3**, replacing the GdCl₃-solution with an aqueous YCl₃-solution.

¹H-NMR (500 MHz, D₂O): δ_{H} = 1.19 - 1.37 (m, 4H, CH₂), 1.37 - 1.61 (m, 4H, CH₂), 2.09 - 3.99 (m, 26H, N(CH₂)₂N, NCH₂C=O, NCH₂CH₂, H₂NCH₂); **MS** (ESI) *m/z*: 532.1 ([M+H]⁺), 554.0 ([M+Na]⁺), mol. wt. calculated for C₂₀H₃₆N₅O₆Y: 531.17; **IR** (KBr): $\tilde{\nu}$ = 3646 - 3210 (br, ν (NH)), 2947, 2864 (s, ν (CH₂)), 1694 (m, ν (C=O)), 1621 (m, δ (NH)).

6.1.3.3 Synthesis of DOTA-ButAm (10)

Synthesis of 1,4,7-Tris(*tert*-butoxycarbonylmethyl)-1,4,7,10-tetraazacyclododecane (17)

Compound **17** was prepared from 1,4,7,10-tetraazacyclododecane and *tert*-butyl bromoacetate according to ref. 91 in 74% yield.

¹H NMR (400 MHz, CDCl₃): δ_{H} = 1.42, 1.43 (s, 27H, C(CH₃)₃), 2.76 - 2.98 (m, 12H, N(CH₂)₂N), 3.07 (m, 4H, HN(CH₂)₂), 3.26, 3.35 (s, 6H, NCH₂C=O), 9.98 (br s 1H, NH); **MS** (ESI) *m/z*: 515.2 ([M+H]⁺), mol. wt. calculated for C₂₆H₅₀N₄O₆: 514.37.

Synthesis of N_o-Z-2-bromolysine methyl ester (15)

To a stirred solution of N_o-Z-L-lysine (**13**) (5.00 g, 18 mmol, 1 eq.) in aqueous 2 N hydrobromic acid (50 mL) cooled to 0°C sodium nitrite (1.35 g, 20 mmol, 1.1 eq.) was added gradually over 45 min. 30 min after the last addition, the solution was extracted four times with ethyl acetate (200 mL). The combined organic layers were dried over sodium sulfate. Removal of the solvent under reduced pressure resulted in a yellow oil (5.79 g, 94% yield, about 60% pure due to ¹H NMR).

¹H NMR (400 MHz, CDCl₃): δ_H = 1.42 (m, 2H, BrCHCH₂CH₂), 1.53 (m, 2H, HNCH₂CH₂), 1.99 (m, 2H, BrCHCH₂), 3.19 (m, 2H, NHCH₂), 4.22 (m, 1H, BrCH), 5.09 (s, 2H, O=COCH₂), 7.27 - 7.39 (m, 5H, H_{Ar}), 9.46 (br s, 1H, O=COH).

The crude product **14** was solved in methanol (17 mL), conc. sulfuric acid (0.45 mL, 8.4 mmol, 0.5 eq.) was added and the solution refluxed for 1.5 h. After cooling to rt, the solvent was removed under reduced pressure. The remaining yellow oil was taken up in diethyl ether and washed with an aqueous 5% NaHCO₃ solution and with brine. After drying the organic solution with magnesium sulfate, the solvent was removed under reduced pressure and the crude product was purified on a silica gel column (chloroform / methanol 95:5) resulting in a yellowish oil (3.37 g, 53% yield).

¹H NMR (400 MHz, CDCl₃): δ_H = 1.32 (m, 2H, BrCHCH₂CH₂), 1.45 (m, 2H, HNCH₂CH₂), 1.97 (m, 2H, BrCHCH₂), 3.11 (m, 2H, NHCH₂), 3.69 (s, 3H, O=COCH₃), 4.16 (t, ³J_{HH}=7.1 Hz, 1H, BrCH), 5.04 (s, 2H, CH₂Ph), 5.22 (br s, 1H, NH), 7.24 - 7.31 (m, 5H, H_{Ar}); ¹³C{¹H} NMR (100.61 MHz, CDCl₃): δ_C = 24.4 (BrCHCH₂CH₂), 29.2 (HNCH₂CH₂), 34.4 (BrCHCH₂), 40.7 (NHCH₂), 45.6 (BrCH), 52.6 (O=COCH₃), 66.6 (CH₂Ph), 128.0, 128.1, 128.5 (C_{Ar}), 136.8 (CH₂C_{Ar}), 156.7 (NHC=O), 170.4 (O=COCH₃); MS (FAB) m/z: 357.9 ([M+H]⁺), 314.0 ([M+H-CO₂]⁺), mol. wt. calculated for C₁₅H₂₀BrNO₄: 357.06.

Synthesis of DOTA-ButAmZ(^tBu)₃Me (18)

Under an argon atmosphere DO3A(^tBu)₃ (**17**) (1.00 g, 1.9 mmol, 1 eq.) was dissolved in dry acetonitrile (20 mL). K₂CO₃ (788 mg, 5.7 mmol, 3 eq.) and a solution of **15** (766 mg, 2.1 mmol, 1.1 eq.) in dry acetonitrile (10 mL) were added and the mixture was refluxed for 24 h. After cooling to rt, the solid was filtered off and the solvent removed under reduced pressure. The crude product was purified on a silica gel column (pure CHCl₃, gradually increasing the ratio of MeOH to 20%) resulting in a colourless solid (1.01 g, 67% yield).

¹H NMR (400 MHz, CDCl₃): δ_H = 0.95 - 1.59 (br, 33H, C(CH₃)₃, CH(CH₂)₃), 1.61 - 3.19 (br, 25H, N(CH₂)₂N, NCH₂C=O, CH, CH₂NH), 3.33 (s, 3H, O=COCH₃), 4.72 (s, 2H, CH₂Ph), 5.54 (br s, 1H, NH), 6.84 - 7.07 (m, 5H, H_{Ar}); **¹³C{¹H} NMR** (100.61 MHz, CDCl₃): δ_C = 23.9, 25.2, 29.1 (CH(CH₂)₃), 27.1 (br, C(CH₃)₃), 39.6 (HNCH₂), 51.7 (O=COCH₃), 44.3, 46.3, 47.3, 47.7 (2C), 51.3, 51.9 (2C), 54.7, 54.9 (2C) (N(CH₂)₂N, NCH₂C=O), 59.8 (CH), 65.1 (CH₂Ph), 81.1, 81.4 (C(CH₃)₃), 126.9, 127.6, 136.3 (C_{Ar}), 155.9 (HNC=O), 171.9, 172.2 (2C) (O=COC(CH₃)₃), 175.7 (O=COCH₃); **MS** (FAB) m/z: 814.3 ([M+Na]⁺), mol. wt. calculated for C₄₁H₆₉N₅O₁₀: 791,50.

Synthesis of DOTA-ButAm(^tBu)₃Me (19)

Under argon atmosphere **18** (1.01 g, 1.3 mmol) was dissolved in dry methanol (50 mL) and Pd/C (10% Pd, 200 mg) was added. The mixture was vigorously stirred under a hydrogen atmosphere (balloon) for 3 h. The catalyst was filtered off and the solvent removed under reduced pressure, yielding a colourless solid (727 mg, 85 % yield).

¹H NMR (400 MHz, CDCl₃): δ_H = 0.98 (s, br, 27 H, C(CH₃)₃), 3.21 (s, 3H, O=COCH₃), 0.48 - 4.04 (br, 61H, C(CH₃)₃, CH(CH₂)₃, N(CH₂)₂N, NCH₂C=O, CH, CH₂NH₂), 7.97 (s, br, 2H, NH₂); **¹³C{¹H} NMR** (100.61 MHz, CDCl₃): δ_C = 24.1, 25.2, 26.4 (CH(CH₂)₃), 26.9 (br, C(CH₃)₃), 38.6 (H₂NCH₂), 51.1 (O=COCH₃), 44.1, 46.1, 47.1, 47.5 (2C), 51.5, 51.9 (2C), 54.5, 54.7 (2C) (N(CH₂)₂N, NCH₂C=O), 59.7 (CH), 80.8, 81.1 (C(CH₃)₃), 171.8, 172.0 (2C) (O=COC(CH₃)₃), 175.5 (O=COCH₃).

Synthesis of DOTA-ButAm (10)

Compound **19** was refluxed in 6 N HCl (30 mL) for 18 h. After cooling to rt, the aqueous phase was washed with diethyl ether (mL), and the solvent was removed under reduced pressure, resulting in a colourless solid **10** × nHCl (677 mg, 30% purity due to reaction with LnCl₃).

¹H NMR (400 MHz, CDCl₃): δ_H = 0.98 - 1.89 (br, 6H, CH₂), 2.23 - 4.39 (br, 25H, N(CH₂)₂N, NCH₂C=O, NCHC=O, CH₂NH₂); **MS** (ESI) m/z: 476.20 ([M+H]⁺), mol. wt. calculated for C₂₀H₃₇N₅O₈: 475.26.

6.1.3.4 Synthesis of Y[DOTA-ButAm]Na (11)

DOTA-ButAm (50 mg, 3.1×10⁻⁵ mol, 1 eq.) was solved in water (500 μL) and the pH was adjusted to 6.6 with NaOH. Then, aqueous YCl₃-solution (58 μL, 3.1×10⁻⁵ mol, 1 eq.) was

added and the pH of the solution was adjusted to 7.5 with NaOH. Under stirring the solution was heated to 60 °C for 3 h. To remove excess of Y(III), Chelex 100 was added and stirred for 1 h. The solution was decanted from the cation exchange resin and the water removed under vacuum at 40 °C. The raw product was used without further purification.

¹H NMR (400 MHz, D₂O): δ_H = 1.32 - 2.12 (br, 8H, CH₂), 2.32 - 3.51 (br, 23H, N(CH₂)₂N, NCH₂C=O, NCHC=O); MS (ESI) m/z: -560.2 ([M]⁻), mol. wt. calculated for C₂₀H₃₃N₅O₈Y⁻: 560.41.

6.1.3.5 Synthesis of DOTA-BA (4)

Compound **4** was prepared according to ref. 60.

MS (ESI) m/z: 525.2 ([M+H]⁺), mol. wt. calculated for C₂₃H₃₂N₄O₁₀: 524.52.

6.1.3.6 Synthesis of Ln[DOTA-BA][*n*-Bu₄N] (5, 6)

Compound **5** and **6** were prepared according to ref. 60.

5: MS (ESI) m/z: -609.2 ([M]⁻), mol. wt. calculated for C₂₃H₂₈N₄O₁₀Y⁻: 609.4.

6.1.3.7 Synthesis of DOTA-GA (7)

Compound **7** was prepared according to ref. 60.

MS (ESI) m/z: 477.1 ([M+H]⁺), mol. wt. calculated for C₁₉H₃₂N₄O₁₀: 476.48.

6.1.3.8 Synthesis of Ln[DOTA-GA][*n*-Bu₄N] (8, 9)

Compound **8** and **9** were prepared according to ref. 60.

8: MS (ESI) m/z: -561.6 ([M]⁻), mol. wt. calculated for C₁₉H₂₈N₄O₁₀Y⁻: 561.35.

6.2 Syntheses and Modification of Silica Nanoparticles

6.2.1 Solvents, Reagents and Equipment

All reagents were used without further purification, unless otherwise mentioned. Triethoxysilane (TES) (puriss, 99%), *N,N'*-diisopropylcarbodiimide (DIC) (99%), *N*_α-Fmoc-*N*_ω-Dde-D-lysine, benzene-1,3,5-tricarboxylic acid (98%), and 3-butenic acid (97%) were purchased from Sigma-Aldrich, (3-aminopropyl)triethoxysilane (APTES) (99%) from Acros Organics, hydrazine monohydrate (99+%) from Alfa Aesar, tetraethyl orthosilicate (TEOS) (puriss., ≥99.0% (GC)), (3-glycidyloxypropyl)trimethoxysilane (GOPTS) (purum, 97.0%), DMSO, (puriss., absolute, over molecular sieve (H₂O ≤0.005%), ≥99.5% (GC)), piperidine

(puriss. plus, $\geq 99.5\%$ (GC)), and NH_4OH (25% NH_3 in H_2O) from Fluka, thionyl chloride, *O*-(benzotriazol-1-yl)-*N,N,N',N'*-tetramethyluronium tetrafluoroborate (TBTU), *N*-hydroxysuccinimide (NHS), and diisopropylethylamine (DIPEA) from Merck, and 10-undecylenic acid from Riedel de Haen. Cy5.5 NHS-ester was bought from Lumiprobe and fluorescein-5-isothiocyanate (FITC) from Merck. H_2 5.0 and Ar 5.0 were used. Toluene and *n*-hexane were dried by distillation from sodium and benzophenone, followed by storage over molecular sieve (4 Å).

Ultraviolet Lamp. For the photochemical hydrosilylation a 700 W medium pressure Hg Lamp (Heraeus) was used.

Oven. A tube furnace RO 4/50 with thermicon P® control unit (Heraeus) was used for tempering of the NPs and for the chlorination-reduction sequence.

Centrifugation. Materials were separated, using a Sorvall RC 5C Plus centrifuge with a Sorvall SS-34 rotor, a Beckman L80 ultracentrifuge with a 70Ti rotor or an Eppendorf 5430 R centrifuge with a FA-45-24-11-HS rotor. Appropriate tubes were used at 15,000 - 20,000 rpm for 5-10 min.

6.2.2 Characterisation Methods

Nitrogen Isotherm Measurements (BET). Adsorption and desorption isotherms were measured at 77.35 K with nitrogen, using an ASAP 2010 V 4.01 G or an ASAP 2020 V 1.04 H instrument from Micromeritics. The samples were degassed 150 min at 100 °C and 1 mPa. The specific surface area was calculated according to the Brunauer, Emmet and Teller (BET) multipoint method.

Dynamic Light Scattering. DLS-measurements were performed on a Coulter n4plus submicron particle sizer with He-Ne laser (632.8 nm) at 20 °C. The samples were suspended in water by ultrasonication (30 min), the concentration was adjusted to get 5×10^4 - 1×10^6 counts s^{-1} . After 5 min of calibration five measurements were performed with a detection angle of 90°, and evaluated by means of SDP analysis.

Scanning Electron Microscopy. Scanning electron micrographs were recorded on a Zeiss DSM 962 (tungsten filament; **M0b** and derived materials), a Philips XL 30-FEG (field emission; **M0a** and **M0₁₃₀** and derived materials), or a FEI ESEM Dual Beam Quanta 3D FEG (field emission; **M0₅₀** and derived materials). Particles were suspended in ethanol by 30 min of ultrasonication (1 mg mL^{-1}), and 20 μL of the suspension were dropped on a silicon wafer (10 × 5 mm) or Al sample holders. Ethanol was removed by spinning the wafer on a

spincoater (4000 rpm for 30 s) and heating for 30 s or by spinning the Al holders per hand. The samples for the Philips XL 30-FEG were sputter coated with Au-Pd for 20 s in a Agar Sputter Coater B7340 prior to measuring. To evaluate the size of the particles statistically, 100-200 particles were measured in gimp 2.6 or CorelDraw.

Zetapotential Measurements. Zetapotential was measured on a Zetasizer Nano ZS from Malvern Instruments. The samples were suspended in a PBS solution or a solution of cell culture medium with 10% of serum, respectively. As the conductivity of suspensions for zetapotential measurements should be between 0.1 and 0.5 mS cm⁻¹, a PBS solution of 12 mM of PO₄³⁻ was diluted 1:100 with bidest. water to reach a conductivity of 0.2 mS cm⁻¹. The medium with 10% of serum also was diluted 1:100 with bidest. water to get a conductivity of 0.17 mS cm⁻¹. The pH of the solutions was adjusted to 7.4 and the samples suspended by 1 h of ultrasonication (0.15 mg mL⁻¹). For the measurements disposable capillary cells were used, and the suspensions injected through a 0.45 µm Millipore filter. After 3 min of temperature calibration, four measurements were performed at 25 °C, whereat the first of each sample was discarded. Particle size was determined from a scattering angle of 173°.

Elemental Analysis. Elemental analyses were performed on a vario MICRO cube, Elementaranalysensysteme GmbH, in the CHNS mode.

TG Measurements. TG measurements were performed on a STA 499 F3 Jupiter from Netzsch. The samples were heated under air from 30 - 1000 °C in Al₂O₃-crucibles with a rate of 10 °C min⁻¹ and gas flow rate of 20 mL min⁻¹.

Gd Content from T₁-Measurements. Gd functionalised particles were suspended in concentrated HNO₃, and heated to 120 °C for 24 h. By that treatment Gd(III) is released from the chelate. The T₁ of the water protons in those solutions was measured at 400 MHz and 26 °C, and the Gd(III)-concentrations were determined from a standard curve. Standard solutions were GdCl₃-solutions (0.01 - 2 mM) and a comparable amount of unfunctionalised silica NPs was added and treated with HNO₃, like the samples. Gd(III)-concentrations were calculated from Equations 1 and 2.

$$\frac{1}{T_{1,o}} = \frac{1}{T_{1,d}} + \frac{1}{T_{1,p}} \quad \text{Eq. 6.1}$$

$$\frac{1}{T_{1,o}} = \frac{1}{T_{1,d}} + r_1 \cdot [\text{Gd}] \quad \text{Eq. 6.2}$$

Calculation method for the Gd(III) number per particle. The number of Gd(III) per NP (n_{Gd}/NP) is calculated from Equations 6.3 - 6.5, where n_{Gd}/g is the number of Gd(III) ions per gram of NPs, n_{NP}/g the number of NPs per gram, $\Gamma_{\text{Gd(III)}}$ the surface concentration of Gd(III) in mol g^{-1} , N_{A} the Avogadro constant, A_{BET} the specific surface area of the particles and A_{geo} the surface area of the NPs, derived from d_{SEM} .

$$n_{\text{Gd}}/\text{NP} = n_{\text{Gd}}/\text{g} / n_{\text{NP}}/\text{g} \quad \text{Eq. 6.3}$$

$$n_{\text{Gd}}/\text{g} = \Gamma_{\text{Gd(III)}} \cdot N_{\text{A}} \quad \text{Eq. 6.4}$$

$$n_{\text{NP}}/\text{g} = A_{\text{BET}} / A_{\text{geo}} \quad \text{Eq. 6.5}$$

ICP Atomic Emission Spectrometry. ICP-AES measurements were performed by Mikroanalytisches Labor Pascher. Samples were dried at 30 °C in vacuo and treated with HNO_3/HCl at 180 °C. Gd was detected with a Thermo ICAP 6500, using Co as internal standard.

DRIFT Spectroscopy. DRIFT experiments were performed on a Bruker Vertex 70 FTIR Spectrometer. The spectra were recorded with a resolution of 4 cm^{-1} and 16 scans from 4000 to 500 cm^{-1} versus pure KBr as blank. DRIFT samples were mixed with dry KBr at a ratio of 1:5.

Solid State NMR Spectroscopy. ^{13}C CP/MAS NMR experiments were performed in 4 mm ZrO_2 rotors at a spinning speed of 10 kHz on a Bruker DSX 200 spectrometer, operating at 50.3 MHz for ^{13}C nuclei. Adamantane was used as external standard. ^{29}Si HPDEC/MAS NMR experiments were performed in 7 mm ZrO_2 rotors at a spinning speed of 4 kHz on a Bruker ASX 300 spectrometer, operating at 59.6 MHz for ^{29}Si nuclei. Q_8M_8 was used as external standard.

MR Imaging of $\text{M1C}_4[\text{Gd}]$ and $\text{M2C}_4[\text{Gd}]$ in Agar Phantoms. MRI experiments were performed in 1.5% agar to stabilise the dispersion of the material throughout the measurement. For this purpose, a stock of 10 mg mL^{-1} in water was well dispersed by sonication and dilutions between 100 and $10,000 \text{ }\mu\text{g mL}^{-1}$ were prepared. $50 \text{ }\mu\text{L}$ of these dilutions were immediately mixed with $50 \text{ }\mu\text{L}$ 1.5% agar, transferred into 0.6 mL tubes and gelled in ice. Afterwards, the agar gel was covered by $300 \text{ }\mu\text{L}$ water or complete cell culture medium. Thus, samples containing 5 to $500 \text{ }\mu\text{g}$ per $100 \text{ }\mu\text{L}$ **$\text{M1C}_4[\text{Gd}]$** (Gd content $45 \text{ }\mu\text{mol g}^{-1}$) and **$\text{M2C}_4[\text{Gd}]$** (Gd content $50 \text{ }\mu\text{mol g}^{-1}$), corresponding to $2.2\text{-}220 \text{ }\mu\text{mol L}^{-1}$ Gd and $2.5\text{-}250 \text{ }\mu\text{mol L}^{-1}$, respectively, were prepared. These samples were measured at 123 MHz (3 T)

and room temperature. Longitudinal and transverse relaxation rates were determined in axial slices of 1 mm thickness through the sample containing agar layer and the supernatant.

T_1 was measured, using an inversion-recovery sequence, with an adiabatic inversion pulse, followed by a turbo-spin-echo readout. Between 10 and 15 images were taken, with the time between inversion and readout varying from 23 ms to 3000 ms. With a repetition time of 10 s, 15 echoes were acquired per scan and averaged six times. For T_2 , a spin-echo sequence was used with echo times varying from 18 ms to 1000 ms in about 10 steps and a repetition time of 8 s. Diffusion sensitivity was reduced by minimizing the crusher gradients, surrounding the refocusing pulse. All experiments scanned 2562 voxels in a field-of-view of 110 mm in both directions, resulting in a voxel volume of $0.43 \times 0.43 \times 1 \text{ mm}^3$.

Data analysis was performed by fitting to relaxation curves with self-written routines under MATLAB 7.1 R14 (The Mathworks Inc., United States). The series of T_1 and T_2 relaxation data were fitted to the following equations:

a) T_1 series with varying $t = \text{TI}$: $S = S_0 (1 - \exp(-t / T_1)) + S(\text{TI} = 0) \exp(-t / T_1)$.

b) T_2 series with varying $t = \text{TE}$: $S = S_0 \exp(-t / T_2)$.

Nonlinear least-squares fitting of three parameters S_0 , $S(\text{TI} = 0)$, and T_1/T_2 was done for manually selected regions-of-interest with the Trust-Region Reflective Newton algorithm implemented in MATLAB. The quality of the fit was controlled by visual inspection and by calculating the mean errors and residuals.

In addition, sagittal as well as axial T_1 -weighted MR images were made with imaging sequences (IR-RARE and FLASH) and a spatial resolution typical for in vivo experiments ($0.6 \times 0.6 \times 1 \text{ mm}^3$).

Image intensities were evaluated in the axial images using ImageJ 1.44c (<http://rsb.info.nih.gov/ij>). A circular Region Of Interest (ROI) of 82 voxels was used.

Biodistribution studies. BALB/c recipients were injected intravenously with **M4C₄[Gd]Cy5.5** and biodistribution was analysed using a Maestrix 2 optical imaging system (CRI). 200 μL of 1.5 mg mL^{-1} silica NPs were injected. Background fluorescence was subtracted by the implemented software of the Maestro 2 device (unmixing function).

Western Blot of M4C₄AB. α -ICAM, α -VCAM or isotype control coupled silica NPs were boiled in SDS buffer to detach antibodies from nanoparticles and subsequently analyzed by 10% SDS-PAGE electrophoresis. Western blot detection was performed using a horseradish peroxidase (HRP) coupled secondary antibody. Band intensities were quantified

using imageJ software and coupling efficacy and the numbers of antibodies bound per particles were calculated.

ELISA of M4C₄AB. Antigen-specific binding of antibody coupled silica NPs was determined by enzyme-linked immunosorbent assay (ELISA). 96-well plates (Thermo Fischer Scientific) were coated with recombinant ICAM-1-Fc protein (R&A) (4 μ g/ml in PBS) and incubated with different amounts of AB coupled silica NPs as indicated. Different concentrations of antibodies were used during the coupling reaction as indicated. Plates were washed extensively to remove non-specifically bound particles. Particle binding was quantified using a HRP-coupled secondary antibody (Dianova) for detection.

6.2.3 Syntheses

Analytical data of the materials is given and discussed in chapter 4 (Results and Discussion) and is therefore not described here. Estimated amounts of functional groups to calculate the amounts of reactants are based on $\Gamma_{\text{Si-OH}}$ (Table 4.5, **M1** and **M2**) or Γ_{ligand} (Table 4.19, **M3bC₁₁COOH** and **M3/4aC₄COOH** (amount halved as sterical hindrance is assumed)).

Synthesis of silica nanoparticles (M0₁₃₀, M0₁₀₀). A solution of ethanol and water was heated to 75 °C. After 15 min of temperature equilibration, 12.46 M aqueous ammonia and TEOS were quickly added under strong stirring. After 2 h of vigorous stirring at 75 °C, the resulting particles were separated by centrifugation and washed with water, ethanol/water (3:1) and water again. For washing, the particles were treated by ultrasonication for 30 min and centrifuged after each step. The particles were dried at 100 °C (**M0b₁₀₀**) and then at 600 °C (**M0a₁₀₀**) under vacuum for at least 15 h each. Reaction conditions and yields are listed in Table 6.1.

Synthesis of silica nanoparticles (M0₅₀). Ethanol was heated to 35 °C. After 30 min, an aqueous NH₄OH solution and TEOS were added under strong stirring. The mixture was kept at 35 °C for 20 h and was then allowed to cool down to RT. The material was separated by centrifugation, dispersed in water/ethanol (3:1) by ultrasonication (50 ml) and separated by centrifugation again. The purification step was repeated with water/ethanol (1:3) and then with ethanol. The particles were dried over night at 100 °C in vacuo.

Table 6.1 Reaction conditions for the syntheses of **M0** materials.

material	reaction conditions					yield / g
	V(EtOH) / mL	V(TEOS) / mL	V(NH ₄ OH) / mL	V(H ₂ O) / mL	T / °C	
M0 ₁₃₀	400	30	20	72	75	5.4
M0a ₁₀₀	400	30	20	72	75	6.2
M0b ₁₀₀	100	7.50	5	18	75	1.6
M0 ₅₀	300	11.00	7.57	-	35	2.3

subscript numbers are average diameters

M0a dried at 600 °C, **M0b** only dried at 100 °C

Synthesis of rehydroxylated nanoparticles M0reh. 5 g of **M0**₁₃₀ (**M0**₁₀₀, 2.5 g) were suspended in 3.7% aqueous HCl (50 mL) and refluxed for 1 h to rehydroxylate the surface of the particles. The particles were separated by centrifugation and washed with water (two times) and ethanol. The particles were dried under vacuum at 100 °C for 16 h.

Synthesis of amino terminated nanoparticles M1C₃NH₂. The reaction was carried out under argon. **M0**_{130reh} (2 g) was suspended in dry toluene (15 mL) and APTES (233 µL) was added. The suspension was refluxed under argon for 24 h, then the particles were separated by centrifugation and washed with toluene and hexane (two times, each). The particles were dried under vacuum at 100 °C for 15 h. Yield: 1.8 g of a white powder.

Synthesis of GOPTS modified nanoparticles M2GOPTS. The reaction was carried out under argon. **M0**_{130reh} (2 g) was suspended in dry toluene (15 mL) and GOPTS (221 µL) was added. The suspension was refluxed under argon for 24 h. The particles were separated by centrifugation and washed with toluene and hexane (two times, each). The particles were dried under vacuum at 100 °C for 15 h. Yield: 1.9 g of a white powder.

Silanisation of silica nanoparticles (M3SiH). 2 g of **M0**_{100reh} (**M0**₅₀, 1g) were suspended in 30 (15) mL of dry toluene under argon, and 0.5 (0.25) mL of TES were added. The suspension was refluxed under argon for 24 h, then the particles were separated by centrifugation and washed with toluene and twice with ethanol. The particles were dried under vacuum at 100 °C for 15 h. Yield: 1.9 g of a white powder.

Chlorination-reduction of silica NPs (M4SiH). **M0**₁₀₀ (2 g) was reacted according to a procedure reported.⁶⁷ Under vacuum the silica NPs were heated to 200 °C for at least 6 h, then the temperature was raised to 800 °C over a period of 4 h and held for at least 6 h. Under argon 30 mL of thionyl chloride were heated to 60 °C under stirring and fluxed through the NPs for 4 h. Then the temperature was raised to 1000 °C and for another 4 h hydrogen was

fluxed through the NPs. Finally the NPs were cooled to RT under H₂-atmosphere. Yield: 1.8 g of a white powder.

Gd(III)-chelate modified silica nanoparticles (M1C₃[Gd-BA] and M1C₃[Gd-GA]). M1C₃NH₂ (100 mg, estimated 2.5×10^{-5} mol of -NH₂, 1 eq.) was suspended in DMSO (2 mL). Gd[DOTA-BA](*n*-Bu)₄N (Gd[DOTA-GA](*n*-Bu)₄N) (3.0×10^{-5} mol, 1.5 eq.) was dissolved in DMSO (1 mL) and TBTU (14 mg, 4.5×10^{-5} mol, 1.8 eq.) and DIPEA (51 μ L, 3.0×10^{-4} mol, 12 eq.) were added under stirring. After 5 min the nanoparticle suspension was added. The suspension was stirred for 3 h. The resulting material was separated by centrifugation and washed with DMF, water, ethanol, and *n*-hexane. The particles were dried at 60 °C under vacuum for 3 d. Yield: 91 (90) mg of slightly yellowish powder. Absence of free Gd(III) ions in the final materials was confirmed by the xylenol-test⁷⁷ of suspended materials in water.

Gd(III)-chelate modified silica nanoparticles (M2[Gd-HA]). M2GOPTS (200 mg, estimated 5×10^{-5} mol of -CHOCH₂, 1 eq.) was suspended in DMSO (3 mL) and a solution of Gd[DO3A-HA] **3** (5.5×10^{-5} , 1 eq.) in 1 mL of DMSO was added. TBTU (24 mg, 7.5×10^{-5} mol, 1.5 eq.) and DIPEA (65 μ L, 5.0×10^{-4} mol, 10 eq.) were added under stirring. The suspension was left under ultrasonication for 1 h and was then stirred for 1 h. The resulting material was separated by centrifugation and washed with DMF, water, ethanol, and *n*-hexane. Yield: 181 mg of slightly yellowish powder. Absence of free Gd(III) ions in the final materials was confirmed by the xylenol-test⁷⁷ of suspended materials in water.

4-Butenoic acid modified silica nanoparticles (M3C₄COOH and M4C₄COOH) and 10-Undecylenic acid modified silica nanoparticles (M3C₁₁COOH and M4C₁₁COOH) by photochemically induced hydrosilylation. The reaction was carried out under argon. Si-H functionalised particles were dried under vacuum at 100 °C for 1 h and suspended in dry *n*-hexane under ultrasonication for 30 min in a quartz Schlenk tube. Then 3-butenoic acid or 10-undecylenic acid was added and the suspension was degassed by 3-6 freeze-pump-thaw cycles. Under vigorous stirring the suspension was irradiated by a 700 W medium pressure mercury lamp for 5 days. Every day the suspension was treated with ultrasound for a few minutes. The resulting particles were separated by centrifugation and washed three times with *n*-hexane. The particles were dried under vacuum at 100 °C for 15 h and obtained as a white powder.

Table 6.2 Reaction conditions for the syntheses of acid modified materials.

material	reaction conditions			
	m (starting material) / g	V(acid) / μL	V(<i>n</i> -hexane) / mL	yield / g
M3aC₄COOH	1.6	122	20	1.5
M3₅₀C₄COOH	0.8	130	10	0.5
M4aC₄COOH	2.0	153	20	2.0
M3bC₁₁COOH	1.1	224	25	0.9
M4bC₁₁COOH	1.5	273	35	1.3

Gd(III)-chelate modified silica nanoparticles (M3C₄[Gd-HA] and M4C₄[Gd-HA]). The acid modified material (estimated Γ_{COOH} in mol g⁻¹, 1 eq.) was suspended in DMSO, and TBTU (1.5 eq.) and DIPEA (10 eq.) were added under stirring. After 5 min a solution of Ln[DO3A-HA] (**2** or **3**, 1 eq.) in DMSO was added. The suspension was left under ultrasonication for 2 h. The resulting material was separated by centrifugation and washed with DMF, water, ethanol, DCM and *n*-hexane. The particles were dried under vacuum at 40 °C for 16 h yielding a slightly yellowish powder. Absence of free Gd(III) ions in the final materials was confirmed by the xylenol-test of suspended materials in water.

Table 6.3 Reaction conditions for the syntheses of [Gd] modified materials.

material	reaction conditions			
	m (starting material) / g	n (Ln[DO3A-HA]) / mol	V (DMSO) / mL	yield / mg
M3aC₄[Gd-HA]	1	3×10^{-4}	30	903
M3₅₀C₄[Gd-HA]	0.1	2×10^{-4}	2	82
M4aC₄[Gd-HA]	1	3×10^{-4}	30	918
M4aC₄[Y-HA]	0.3	9×10^{-5}	6	156
M3bC₁₁[Gd-HA]	0.78	3.6×10^{-4}	8	771
M4bC₁₁[Gd-HA]	0.1	5.6×10^{-5}	6	89
M4bC₁₁[Y-HA]	0.27	1.9×10^{-4}	8	192

Gd(III)-chelate modified silica nanoparticles (M4C₁₁[Y-ButAm]). 100 mg of **M4C₁₁COOH** (estimated 1.5×10^{-5} mol of -COOH, 1 eq.) were suspended in DMF (5 mL) and TBTU (7.2 mg, 2.3×10^{-5} mol, 1.5 eq.) and DIPEA (255 μL , 1.5×10^{-4} mol, 10 eq.) were

added under stirring. After 5 min a solution of Y[DOTA-ButAm]^{Na} **11** (1.5×10^{-5} mol, 1 eq.) in 1 mL of DMF was added and rinsed with 1 mL of DMF. The suspension was left under ultrasonication for 2 h. The resulting material was separated by centrifugation and washed with DMF, water, ethanol, DCM and *n*-hexane. Yield: 91 mg of slightly yellowish powder.

Antibody functionalised nanoparticles (M4C₄AB). The antibodies (ABs) VCAM-1 (1.96 mg/mL), ICAM-1 (3.06 mg/mL) and an isotype (4.77 mg/mL) were coupled to **M4C₄COOH** (2.5 mg NPs + 50, 100 and 150 µg AB per mg NPs each).

The carboxylic acid groups were activated with NHS and DIC in dry DMF under an argon atmosphere. Therefore, 2.5 mg NPs were suspended in DMF (800 µL), a solution of NHS in DMF (110 µL, 6 M) and DIC (111 µL, 3 M) were added, and the suspensions stirred at RT for 2 h. The activated NPs were centrifuged and washed three times with dry DMF (2 mL, each). Then the activated NPs were suspended in dry DMF (10 µL) and the ABs, dissolved in PBS were added. PBS was added to get a total volume of 1 mL. The suspensions were gently stirred 1 day at RT and 2 days at 4°C, then the NPs were carefully centrifuged and washed with PBS. The NPs **M4C₄AB_{VCAM}**, **M4C₄AB_{ICAM}** and **M4C₄AB_{ISO}** were resuspended and stored in 500 µL PBS.

Syntheses of bifunctional nanoparticles (M4C₁₁₍₄₎Lys). *N*_α-Fmoc-*N*_ω-Dde-D-lysine was used as a bifunctional linker. First the Fmoc protecting group was cleaved by stirring a solution of *N*_α-Fmoc-*N*_ω-Dde-D-lysine (39.95 mg / 160 mg) in DMF (5 mL) with piperidine (1 mL) for 15 min. The piperidine was removed on a rotary evaporator and **M4C₁₁COOH / M4C₄COOH** (500 mg) was added and suspended by ultrasonication. TBTU (36.12 mg / 145 mg) and DIPEA (127.55 µL / 510 µL) were added and the suspension was left under ultrasonication for 2.5 h. The resulting material was separated by centrifugation, washed with DMF and ethanol and dried under vacuum at RT for 15 h.

Coupling of Gd(III)-chelates to M4C₁₁₍₄₎Lys. Ln[DO3A-HA] was coupled according to above procedure. Resulting materials are **M4C₁₁₍₄₎Lys[Gd-HA]**.

Coupling of FITC to M4C₁₁₍₄₎Lys[Gd-HA]. The Dde protecting group was cleaved by treating the NPs **M4C₁₁₍₄₎Lys[Gd-HA]** with hydrazine. The NPs (**M4C₁₁Lys[Gd-HA]**, 400 mg) were suspended in DMF (5 mL) and ultrasonicated for three min after adding hydrazine monohydrate (100 µL, 99%). Then the particles were centrifuged and washed with DMF and ethanol. The particles were resuspended in dry DMF (5 mL) and DIPEA (128 µL) and FITC (29.2 mg) were added. The suspension was stirred at RT in the dark for 24 h, then

the resulting material was centrifuged and washed with DMF and ethanol. **M4C₁₁Lys[Gd-HA]FITC** was dried under vacuum at rt for 15 h. Yield: 328 mg of an orange powder.

Coupling of Cy5.5 to M4C₁₁₍₄₎Lys[Gd-HA]. Cy5.5 was coupled according to the procedure given in ref. 92. **M4C₁₁Lys[Gd-HA]** (25 mg) was suspended in an aqueous NaHCO₃ solution (900 μL, 0.1 M) and Cy5.5 dissolved in dry DMF (100 μL) was added. The suspension was stirred in the dark for 24 h. The resulting material was centrifuged and washed with DMF, water and ethanol until the supernatant was clear. The particles were dried under vacuum at RT for two days and **M4C₁₁Lys[Gd-HA]Cy5.5** was obtained as a blue powder.

7 References

- 1 *The Chemistry of Contrast Agents in Medical Magnetic Resonance Imaging*; Tóth É., Merbach, A. E., Eds.; Wiley: Chichester, 2001.
- 2 Aime, S.; Botta, M.; Fasano, M.; Terreno, E. *Chem. Soc. Rev.* **1998**, *27*, 19-29.
- 3 Caravan, P.; Ellison, J. J.; McMurry, T. J.; Lauffer, R. B. *Chem. Rev.* **1999**, *99*, 2293-2352.
- 4 Lauffer, R. B. *Chem. Rev.* **1987**, *87*, 901-927.
- 5 Kubíček, V.; Tóth, É. *Adv. Inorg. Chem.* **2009**, *61*, 63-129.
- 6 Lowe, M. P. *Aust. J. Chem.* **2002**, *55*, 551-556.
- 7 Barbé, C.; Bartlett, J.; Kong, L.; Finnie, K.; Lin, H. Q.; Larkin, M.; Calleja, S.; Bush, A.; Calleja, G. *Adv. Mater.* **2004**, *16*, 1959-1966.
- 8 Hsiao, J.-K.; Tsai, C.-P.; Chung, T.-H.; Hung, Y.; Yao, M.; Liu, H.-M.; Mou, C.-Y.; Yang, C.-S.; Chen, Y.-C.; Huang, D.-M. *small* **2008**, *4*, 1445-1452.
- 9 Cho, K.; Wang, X.; Nie, S.; Chen, Z.; Shin, D. M. *Clin. Cancer Res.* **2008**, *14*, 1310-1316.
- 10 Davis, M. E.; Chen, Z.; Shin, D. M. *Nat. Rev. Drug Discovery* **2008**, *7*, 771-782.
- 11 Peer, D.; Karp, J. M.; Hong, S.; Farokhzad, O. C.; Margalit, R.; Langer, R. *Nat. Nanotechnol.* **2007**, *2*, 751-760.
- 12 Jin, Y.; Li, A.; Hazelton, S. G.; Liang, S.; John, C. L.; Selid, P. D.; Pierce, D. T.; Zhao, J. *Coord. Chem. Rev.* **2009**, *253*, 2998-3014.
- 13 Taylor-Pashow, K. M. L.; Della Rocca, J.; Huxford, R.; Lin, W. *Chem. Commun.* **2010**, *46*, 5832-5849.
- 14 Rieter, W. J.; Kim, J. S.; Taylor, K. M. L.; An, H.; Lin, W.; Tarrant, T.; Lin, W. *Angew. Chem. Int. Ed.* **2007**, *46*, 3680-3682.
- 15 Lanza, G. M.; Winter, P. M.; Caruthers, S. D.; Morawski, A. M.; Schmieder, A. H.; Crowder, K. C.; Wickline, S. A. *J. Nucl. Cardiol.* **2004**, *11*, 733-43.
- 16 Gianolio, E.; Giovenzana, G. B.; Ciampa, A.; Lanzardo, S.; Imperio, D.; Aime, S. *ChemMedChem* **2008**, *3*, 60-62.
- 17 Louie, A. *Chem. Rev.* **2010**, *110*, 3146-3195.

- 18 Voisin, P.; Ribot, E. J.; Miraux, S.; Bouziers-Sore, A.-K.; Lahitte, J.-F.; Bouchaud, V.; Mornet, S.; Thiaudière, E.; Franconi, J.-M.; Raison, L.; et al. *Bioconjugate Chem.* **2007**, *18*, 1053-1063.
- 19 Carniato, F.; Tei, L.; Dastrù, W.; Marchese, L.; Botta, M. *Chem. Commun.* **2009**, *10*, 1246-1248.
- 20 Carniato, F.; Tei, L.; Cossi, M.; Marchese, L.; Botta, M. *Chem. Eur. J.* **2010**, *16*, 10727-10734.
- 21 van Schooneveld, M. M.; Vucic, E.; Koole, R.; Zhou, Y.; Stocks, J.; Cormode, D. P.; Tang, C. Y.; Gordon, R. E.; Nicolay, K.; Meijerink, A.; et al. *Nano Lett.* **2008**, *8*, 2517-2525.
- 22 Schubert, U.; Hüsing, N. *Synthesis of Inorganic Materials*, Wiley-VCH, Weinheim: **2000**, 192 ff.
- 23 Wright, J. D.; Sommerdijk, N. *Sol-Gel Materials. Chemistry and Applications*, CRC Press, **2001**.
- 24 Brinker, C. J.; Scherer, G. W. *Sol-Gel Science: the physics and chemistry of sol-gel processing*, Academic Press, Inc.: San Diego **1990**.
- 25 Lindner, E.; Schneller, T.; Auer, F.; Mayer, H. A. *Angew. Chem.* **1999**, *111*, 2288-2309. *Angew. Chem. Int. Ed.* **1999**, *38*, 2155-2174.
- 26 Stöber, W.; Fink, A.; Bohn, E. *J. Colloid Interface Sci.* **1968**, *26*, 62-69.
- 27 van Blaaderen, A.; Kentgens, A. P. J. *J. Non-Cryst. Solids* **1992**, *149*, 161-178.
- 28 Tan, C. G.; Bowen, B. D.; Epstein, N. *J. Colloid Interface Sci.* **1987**, *118*, 290-293.
- 29 Unger, K. K. *Porous Silica: Its Properties and Use as Support in Column Liquid Chromatography*; Vol. 16, J. Chromatogr. Library, Elsevier: Amsterdam, 1979.
- 30 Van der Voort, P.; Vansant, E. F. *J. Liq. Chromatogr. Rel. Technol.* **1996**, *19*, 2723-2752.
- 31 Sandoval, J. E.; Pesek, J. J. *Anal. Chem.* **1991**, *63*, 2634-2641.
- 32 Wang, L.; Estévez, M. C.; O'Donoghue, M.; Tan, W. *Langmuir* **2008**, *24*, 1635-1639.
- 33 Marciniak, B. *Hydrosilylation: A Comprehensive Review on Recent Advances*, Springer, **2009**.
- 34 Pesek, J. J.; Matyska, M. T.; Williamsen, E. J.; Evanchic, M.; Hazari, V.; Konjuh, K.; Takhar, S.; Tranchina, R. *J. Chromatogr. A* **1997**, *786*, 219-228.
- 35 Plumeré, N. *Dissertation*, 2009, University of Tuebingen.
- 36 Buriak, J. M. *Chem. Rev.* **2002**, *102*, 1271-1308.

- 37 Nelles, J.; Sendor, D.; Ebberts, A.; Petrat, F. M.; Wiggers, H.; Schulz, C.; Simon, U. *Colloid Polym. Sci.* **2007**, *285*, 729-736.
- 38 Mischki, T. K.; Lopinski, G. P.; Wayner, D. D. M. *Langmuir* **2009**, *25*, 5626-5630.
- 39 Cicero, R. L.; Linford, M. R.; Chidsey, C. E. D. *Langmuir* **2000**, *16*, 5688-5695.
- 40 Lee, M. V.; Scipioni, R.; Boero, M.; Silvestrelli, P. L.; Ariga, K. *Phys. Chem. Chem. Phys.* **2011**, *13*, 4862-4867.
- 41 Atkins, P. W. *Physikalische Chemie*, VCH: Weinheim, 1996, 2. Auflage, 930 ff.
- 42 Wedler, G. *Lehrbuch der physikalischen Chemie*, Wiley-VCH: Weinheim 1997, 4. Auflage, 428 ff.
- 43 Langmuir, I. Surface Chemistry. In: *Nobel Lectures, Chemistry 1922-1941*, Elsevier Publishing Company: Amsterdam, 1966.
- 44 Brunauer, S.; Emmett, P.H.; Teller, E. *J. Am. Chem. Soc.* **1938**, *60*, 309-319.
- 45 Gregg, S. J. *Adsorption, surface area and porosity*, Academic Press Inc.: London 1982, 2nd ed.
- 46 Coulter, *Reference Manual of N4 Plus Submicron Particle Sizer*, 1995.
- 47 Lechner, M. D.; Gehrke, K.; Nordmeier, E. H. *Makromolekulare Chemie*, Birkhäuser Verlag: Basel 2003, 3. Auflage.
- 48 Kortüm, G. *Reflexionsspektroskopie*, Springer Verlag: Berlin 1969.
- 49 Goldstein, J. I.; Newbury, D. E.; Joy, D. C.; Lyman, C. E. *Scanning electron microscopy and x-ray microanalysis*, Kluwer Academic/Plenum Publishers: New York 2003, 3rd ed.
- 50 Plies, E. *Raster- und Transmissionselektronenmikroskopie*, Vorlesungsskript, 2008.
- 51 Idée, J.-M.; Port, M.; Raynal, I.; Schaefer, M.; Le Greneur, S.; Corot, C. *Fundam. Clin. Pharmacol.* **2006**, *20*, 563-576.
- 52 Tweedle, M. F.; Hagan, J. J.; Kumar, K.; Mantha, S.; Chang, C. A. *Magn. Reson. Imaging* **1991**, *9*, 409-415.
- 53 Wang, X.; Jin, T.; Comblin, V.; Lopez-Mut, A.; Merciny, E.; Desreux, J. F. *Inorg. Chem.* **1992**, *31*, 1095-1099.
- 54 Laurent, S.; Forge, D.; Port, M.; Roch, A.; Elst, L. V.; Muller, R. N. *Chem. Rev.* **2008**, *108*, 2064-2110.
- 55 Bulte, J. W. M.; Kraitichman, D. L. *NMR Biomed.* **2004**, *17*, 484-499.
- 56 Na, H. B.; Hyeon, T. *J. Mater. Chem.* **2009**, *19*, 6267-6273.
- 57 Na, H. B.; Song, I. C.; Hyeon, T. *Adv. Mater.* **2009**, *21*, 2133-2148.

- 58 Caravan, P. *Chem. Soc. Rev.* **2006**, *35*, 512-523.
- 59 Henig, J.; Mamedov, I.; Fouskova, P.; Tóth, É.; Logothetis, N. K.; Angelovski, G.; Mayer, H. A. *Inorganic Chemistry* **2011**, *50*, 6472-6481.
- 60 Henig, J.; Tóth, É.; Engelmann, J.; Gottschalk, S.; Mayer, H. A. *Inorg. Chem.* **2010**, *49*, 6124-6138.
- 61 Parker, D.; Millican, T. A.; Beeley, N. R. A. Preparation of azamacrocycles for imaging and treatment of tumors. EP 382583, Feb 12, 1990.
- 62 Feldmann, V. *Diplomarbeit*, 2009, University of Tuebingen.
- 63 Ruff, A. *Diplomarbeit*, 2008, University of Tuebingen.
- 64 Plumeré, N.; Ruff, A.; Speiser, B.; Feldmann, V.; Mayer H. A. *J. Colloid Interface Sci.*, submitted.
- 65 Zhuravlev, L.T. *Colloid Surface A* **2000**, *173*, 1-38.
- 66 Grillet, Y.; Llewellyn, P. L. in *The Surface Properties of Silicas*; Legrand, A. P., Ed.; Chapter 2 A, Wiley: Chichester, 1998, p. 23-27.
- 67 Plumeré, N.; Speiser, B.; Mayer, H. A.; Joosten, D.; Wesemann, L. *Chem.-Eur. J.* **2009**, *15*, 936-946.
- 68 Brühwiler, D. *Nanoscale* **2010**, *2*, 887-892.
- 69 Budny, A.; Novak, F.; Plumeré, N.; Schetter, B.; Speiser, B.; Straub, D.; Mayer, H. A.; Reginek, M. *Langmuir* **2006**, *25*, 10605-11.
- 70 Plumeré, N.; Speiser, B. *Electrochim. Acta* **2007**, *53*, 1244-1251.
- 71 Chu, C. H.; Jonsson, E.; Auvinen, M.; Pesek, J. J.; Sandoval, J. E. *Anal. Chem.* **1993**, *65*, 808-816.
- 72 *Handbook of surface and colloid chemistry*; Birdi, K. S., Ed.; CRC Press: Boca Raton, Fla., 2nd ed., 2003.
- 73 Morrison, I. D.; Ross, S. *Colloidal dispersions: suspensions, emulsions, and foams*; Wiley-Interscience: New York, 2002.
- 74 Evans, D. F.; Wennerström, H. *The colloidal domain: where physics, chemistry, biology, and technology meet*; Wiley-VCH: New York, 2nd ed., 1999.
- 75 Montalbetti, C. A. G. N.; Falque, V. *Tetrahedron* **2005**, *61*, 10827-10852.
- 76 *Adsorption on New and Modified Inorganic Sorbents*; Dabrovsky, A. Tertykh, V. A., Eds.; Elsevier: Amsterdam, 1996.
- 77 Barge, A.; Cravotto, G.; Gianolio, E.; Fedeli, F. *Contrast Med. Mol. Imaging* **2006**, *1*, 184-188.

- 78 Götz, G. F.; Hennig, J.; Ziyeh, S. *Fortschr. Röntgenstr.* **1995**, *162*, 140-144.
- 79 Burai, L.; Hietapelto, V.; Király, R.; Tóth, É.; Brücher, E. *Magn. Reson. Med.* **1997**, *38*, 146-150.
- 80 Chang, C. A.; Francesconi, L. C.; Malley, M. F.; Kumar, K.; Gougoutas, J. Z.; Tweedle, M. F. *Inorg. Chem.* **1993**, *32*, 3501-3508.
- 81 Zhao, F.; Zhao, Y.; Liu, Y.; Chang, X.; Chen, C.; Zhao, Y. *Small* **2011**, *7*, 1322-1337.
- 82 Tantra, R.; Knight, A. *Nanotoxicology* **2011**, *5*, 381-392.
- 83 Leung, B. O.; Chou, K. C. *Appl. Spectrosc.* **2011**, *65*, 967-980.
- 84 Eyrich, M.; Burger, G.; Marquardt, K.; Budach, W.; Schilbach, K.; Niethammer, D.; Schlegel, P. G. *Biol Blood Marrow Transplant* **2005**, *11*, 371-382.
- 85 Henseleit, U.; Steinbrink, K.; Sunderkotter, C.; Goebeler, M.; Roth, J.; Sorg, C. *Exp Dermatol* **1994**, *3*, 249-256.
- 86 Henninger, D. D.; Panes, J.; Eppihimer, M.; Russell, J.; Gerritsen, M.; Anderson, D. C.; Granger, D. N. *J Immunol* **1997**, *158*, 1825-1832.
- 87 Hermanson, G. T. *Bioconjugate Techniques*, Academic Press: San Diego, 1996.
- 88 Kurien B. T.; Scofield R. H. *Methods Mol Biol.* **2009**, *536*, 367-384.
- 89 Burnette, W. N. *Analytical Biochemistry* **1981**, *112*, 195-203.
- 90 Lee, L. J.; Yang, S.-T.; Lai, S.; Bai, Y.; Huang, W.-C.; Juang, Y.-J.; *Microfluidic Enzyme-Linked Immunosorbent Assay Technology*, in: *Advances in Clinical Chemistry*; Makowski, G. S. Ed.; Elsevier, 2006, *42*, 255-295.
- 91 Machitani, K.; Sakamoto, H.; Nakahara, Y.; Kimura, K. *Anal. Sci.* **2008**, *24*, 463-469.
- 92 <http://www.lumiprobe.com/protocols/nhs-ester-labeling>

8 Summary

The development of magnetic resonance imaging (MRI) towards one of the most powerful techniques in clinical diagnosis is accompanied by the progress in the design of paramagnetic contrast agents (CAs) to enhance imaging sensitivity. Most of the currently applied CAs for enhanced T_1 -contrast are based on gadolinium(III) chelate complexes and are mainly extracellular agents which only distribute non-specifically throughout the circulatory system and interstitial spaces. Since those agents are excreted easily and quite fast from the body, they are not suitable for long-term tracking applications. Therefore, nanoparticulate systems were developed and they are currently gaining increased importance in medical diagnosis and treatments. By tailoring hybrid nanomaterials, consisting of an inorganic matrix and functional organic moieties, materials with special properties can be made for various purposes, such as carriers of drugs or for imaging techniques.

In this work, silica nanoparticles (NPs) with a diameter of about 50, 100 and 130 nm were synthesised as matrix to couple Gd(III) chelate complexes as CAs for MRI, fluorophores as probes for optical imaging (OI), and biomolecules for molecular and targeted imaging applications (see Scheme 8.1). The starting materials **M0** were obtained by means of the Stöber process and particles were isolated from their suspensions prior to functionalisation. To covalently couple the functional molecules, the surface of the 130 nm NPs was modified with amino and epoxy groups, respectively, by coating the NPs with functionalised alkoxy silanes. The materials **M1C₃NH₂** and **M2GOPTS** were obtained. The 100 nm NPs were surface modified by two different ways of Si-H functionalisation. The first approach was a silanisation with triethoxy silane (TES), the second one a chlorination reduction sequence with thionyl chloride followed by hydrogen, yielding the materials **M3SiH** and **M4SiH**, respectively. The 50 nm particles were coated with TES to give **M3₅₀SiH**. Subsequently, the Si-H functionalised materials were reacted with terminated unsaturated carboxylic acids of different chain lengths (C_4 and C_{11}) in a photochemically induced hydrosilylation reaction (**M3C_nCOOH**, **M4C_nCOOH**, **M3₅₀C₄COOH**). The carboxylates on the particles' surface allow coupling of functional molecules by forming peptide bonds with amino groups.

The **M0** materials and the surface modified materials were carefully characterised regarding size and shape, surface area and porosity, surface chemical properties, extent of modification and functional groups, and particle-particle interactions.

Then, different Ln(III) complexes of DO3A (**1**, **2**) and DOTA (**3** and **4**, **5** and **6**, **7**) derivatives were synthesised and coupled to the surface modified materials by means of peptide coupling agents. The materials **M1C₃[Ln]**, **M2[Ln]**, **M3C_n[Ln]**, **M4C_n[Ln]**, and **M3₅₀C₄[Ln]** were obtained and characterised with regard to the extent of surface modification, agglomeration behaviour of the particles and the viability as contrast agents.

M1 and **M2** materials could be loaded less effectively with Gd(III) complexes than **M3** and **M4** materials. Surface concentrations of Gd(III) chelate complexes and imaging properties of the materials, obtained by different ways of Si-H functionalisation do not differ significantly. This makes the less complex silanisation with TES the preparation method of choice. With the C₄ spacer higher Gd(III) surface concentrations were obtained, whereas the C₁₁ spacer leads to more stable materials under physiological conditions. Stability tests for all materials show that no Gd(III) ions are released from the chelates. The C₄ materials contain more Gd(III) and therefore are the more effective CAs. Moreover, problems with the agglomeration of the particles could be overcome by introducing the C₄ spacer instead of the C₁₁ spacer. Simultaneously the number of functional groups on the silica surface could be increased, as a telomerisation reaction enables an overstoichiometric coupling of the C₄ spacer. Interestingly, the charge of the complexes coupled to the surface plays a minor role with regard to agglomeration effects.

Gadolinium surface concentrations of up to 83 $\mu\text{mol g}^{-1}$ were reached, and the materials show the typical concentration-dependent increase of the longitudinal relaxation rate R_1 in a clinical 3 T MR scanner at room temperature. The longitudinal relaxivity values per Gd of the materials are increased in comparison to the uncoupled Gd(III) complex, and the high number of Gd(III) complexes per particle leads to remarkably high relaxivity values of up to $6.18 \times 10^5 \text{ mM}^{-1} \text{ s}^{-1}$ per particle. This is comparable to previously published, mesoporous silica materials. Bimodal NPs for MRI and OI were successfully synthesised by the introduction of lysine as a bifunctional linker and coupling of fluorophores (**Fl** = FITC or Cy5.5) next to Gd(III) chelates, yielding **M4C₄₍₁₁₎Lys[Ln]Fl**. The bimodal materials were examined in *in vitro* cell studies regarding localisation and cellular uptake. Biodistribution of the NPs in mice was examined in *in vivo* studies and *ex vivo* derived organs. Finally, antibodies were successfully coupled to the 100 nm acid modified NPs, while their specific interactions with an antigen were maintained.

In conclusion, CA functionalised nonporous silica NPs with a high local relaxivity, bimodal CA and fluorophore modified NPs, and antibody coupled NPs were obtained. These results

indicate that this type of silica nanoparticles can pose a platform for the development of highly effective probes for MRI. Further functionalisation allows the synthesis of multimodal and/or targeted contrast agents for molecular imaging applications.

9 Zusammenfassung

Die Entwicklung der Magnetresonanztomographie (MRT) zu einer der wichtigsten Methoden in der medizinischen Diagnostik geht mit der Entwicklung paramagnetischer Kontrastmittel (CAs) zur Empfindlichkeitssteigerung einher. Die meisten der derzeit eingesetzten CAs zur Erhöhung des T_1 -Kontrasts basieren auf Gadolinium(III)-Chelatkomplexen. Diese dienen hauptsächlich als extrazelluläre Agenzien, die sich unspezifisch im Blutkreislauf und im Interstitium verteilen. Da diese Substanzen schnell und leicht aus dem Körper ausgeschieden werden, sind sie nicht für Langzeitanwendungen geeignet. Dazu wurden nanopartikuläre Systeme entwickelt, die in der klinischen Diagnostik zunehmend an Bedeutung gewinnen. Durch gezielte Synthesen von Hybrid-Materialien, die aus einer anorganischen Matrix und funktionellen organischen Molekülen aufgebaut werden, können Materialien mit ganz bestimmten Eigenschaften für diverse Anwendungen hergestellt werden (z.B. Drug-Carrier-Systeme oder Sonden für bildgebende Verfahren).

In dieser Arbeit wurden Silica-Nanopartikel (NPs) mit Durchmessern von 50, 100 und 130 nm hergestellt. Diese dienen als Matrix für die Anbindung von Gd(III)-Chelatkomplexen als CAs für die MRT, von Fluorophoren als Sonden für die optische Bildgebung und von Biomolekülen für molekulare und zielgerichtete bildgebende Verfahren (siehe Schema 9.1).

Die Ausgangsmaterialien **M0** wurden im Stöber Prozess hergestellt und die Partikel wurden vor der Funktionalisierung aus ihren Suspensionen isoliert. Um funktionelle Moleküle kovalent anbinden zu können, wurden die 130 nm NPs mit Amino- bzw. Epoxygruppen modifiziert. Die Materialien **M1C₃NH₂** und **M2GOPTS** wurden durch Beschichten der NPs mit funktionalisierten Alkoxysilanen erhalten. Die 100 nm NPs wurden auf zwei verschiedene Arten Si-H funktionalisiert. Der erste Weg war eine Silanisierung mit Triethoxysilan (TES) (**M3SiH**), der zweite eine Sequenz aus Chlorierung mit Thionylchlorid, gefolgt von der Umsetzung mit elementarem Wasserstoff (**M4SiH**). Die 50 nm NPs wurden mit TES beschichtet (**M3₅₀SiH**). Anschließend wurden endständig ungesättigte Carbonsäuren verschiedener Kettenlängen (C₄ und C₁₁) in einer photochemisch induzierten Hydrosilylierungsreaktion an die Si-H Bindungen addiert (**M3C_nCOOH**, **M4C_nCOOH**, **M3₅₀C₄COOH**). An die Carbonsäuregruppen auf der Partikeloberfläche können durch die Bildung von Peptidbindungen aminofunktionalisierte Moleküle angebinden werden. Die **M0** Materialien und die oberflächen-modifizierten Materialien wurden sorgfältig charakterisiert in Bezug auf ihre Größe und Form, spezifische Oberfläche und Porosität, chemische

Eigenschaften der Partikeloberflächen, Grad der Funktionalisierung und Anzahl funktioneller Gruppen an der Oberfläche, sowie interpartikuläre Wechselwirkungen.

Anschließend wurden verschiedene Lanthanoid Komplexe von DO3A- (**1**, **2**) und DOTA- (**3** und **4**, **5** und **6**, **7**) Derivaten synthetisiert und mit Hilfe von Peptidkupplungsreagenzien an die oberflächen-funktionalisierten NPs angebunden. Die Materialien **M1C₃[Ln]**, **M2[Ln]**, **M3C_n[Ln]**, **M4C_n[Ln]** und **M3₅₀C₄[Ln]** wurden erhalten und in Bezug auf Grad der Funktionalisierung, Agglomerationsverhalten und ihre Anwendbarkeit als Kontrastmittel charakterisiert.

Die Beladung an Gd(III)-Komplexen verlief für die **M1**- und **M2**-Materialien weniger effektiv als für die **M3**- und **M4**-Materialien. Die Oberflächenkonzentrationen an Gd(III) und die bildgebenden Eigenschaften der Materialien, die durch verschiedene Arten der Si-H-Funktionalisierung erhalten wurden, unterscheiden sich nicht deutlich, daher ist die weniger aufwendige Silanisierung mit TES die Methode der Wahl. Durch die Anbindung des C₄-Spacers wurden höhere Gd(III)-Konzentrationen erreicht, wohingegen die Anbindung des C₁₁-Spacers zu stabileren Materialien unter physiologischen Bedingungen führt. Stabilitätstests für alle Materialien zeigen, dass keine toxischen Gd(III)-Ionen aus den Chelaten freigesetzt werden. Die C₄-Materialien enthalten mehr Gd(III) und sind daher die effektiveren Kontrastmittel. Außerdem konnten Agglomerationsprobleme durch die Einführung des C₄- statt des C₁₁-Spacers überwunden werden. Gleichzeitig konnte die Anzahl an funktionellen Gruppen an der Silica-Oberfläche erhöht werden, da eine Telomerisierungsreaktion eine überstöchiometrische Anbindung der C₄-Säure ermöglicht. Interessanterweise spielt die Ladung der Komplexe eine geringe Rolle für das Agglomerationsverhalten.

Oberflächenkonzentrationen an Gd(III) von bis zu 83 $\mu\text{mol g}^{-1}$ wurden erreicht und die Materialien zeigen den typischen konzentrationsabhängigen Anstieg der longitudinalen Relaxationsrate R_1 in einem klinischen 3 T Magnetresonanztomographen bei Raumtemperatur. Die longitudinalen Relaxivitätswerte pro Gd der Materialien sind im Vergleich zu den ungebundenen Gd(III)-Komplexen erhöht und die hohe Anzahl an angebundenen Komplexen pro Partikel führt zu bemerkenswert hohen Relaxivitätswerten von bis zu $6.18 \times 10^5 \text{ mM}^{-1} \text{ s}^{-1}$ pro Partikel. Diese Werte sind vergleichbar mit denen bereits publizierter mesoporöser Materialien.

Durch die Einführung von Lysin als bifunktionellen Linker und die Anbindung von Fluorophoren (**Fl** = FITC oder Cy5.5) neben Gd(III)-Chelaten, wurden bimodale NPs als CA für die MRT und für optische Bildgebung erfolgreich synthetisiert (**M4C₄₍₁₁₎Lys[Ln]Fl**). Die bimodalen Materialien wurden in *in vitro* Zellstudien bezüglich ihrer Lokalisierung und Zellgängigkeit untersucht. Außerdem wurde die Bioverteilung der NPs in Mäusen in *in vivo* Studien und an entnommenen Organen *ex vivo* untersucht. Schließlich wurden Antikörper erfolgreich an die säure-funktionalisierten 100 nm Partikel angebunden, wobei ihre spezifischen Wechselwirkungen mit einem Antigen erhalten blieben.

Es wurden CA-funktionalisierte unporöse Silica NPs mit hohen lokalen Relaxivitäten, bimodale, mit CAs und Fluorophoren modifizierte NPs und Antikörper-funktionalisierte NPs hergestellt. Diese Ergebnisse zeigen, dass diese Art von Silica-Nanopartikeln eine geeignete Plattform für die Entwicklung hocheffizienter Kontrastmittel für die MRT darstellt. Durch weitere Funktionalisierung können multimodale und/oder zielgerichtete Kontrastmittel für die molekulare Bildgebung synthetisiert werden.

Meine akademische Ausbildung verdanke ich:

K. Albert; T. Chassé; H. Eckstein; K. Eichele; J. Enderlein; G. Gauglitz; J. Ihringer; W. Jäger; N. Kuhn; C. Maichle-Mössmer; M. E. Maier; H. A. Mayer; A. J. Meixner; H.-J. Meyer; U. Nagel; C. Ochsenfeld; H. Oberhammer; E. Plies; H. Pommer; V. Schurig; M. Schwarz; E. Schweda; B. Speiser; V. Urlacher; U. Weimar; L. Wesemann; D. Wistuba; K.-P. Zeller; T. Ziegler.

Lebenslauf

Persönliche Daten

Name: Verena Feldmann
Geburtsdatum, -ort: 28. November 1984, München

Schulausbildung

1991 - 1995 Volksschule Rosenheim-Happing
1995 - 2004 Finsterwalder-Gymnasium Rosenheim, Abitur

Hochschulausbildung

10/2004 - 09/2006 Grundstudium Chemie, Universität Tübingen, Vordiplom
10/2006 - 03/2009 Hauptstudium Chemie, Universität Tübingen, Diplom
10/2008 - 03/2009 Diplomarbeit bei Prof. H. A. Mayer, Universität Tübingen:
Funktionalisierte Silica-Nanopartikel als Kontrastmittel für die
Magnetresonanztomographie
04/2009 - 12/2011 Anfertigung der Doktorarbeit bei Prof. H. A. Mayer, Universität
Tübingen:
Multifunktionale Silica-Partikel als Kontrastmittel für Optische
Bildgebung und Magnetresonanztomographie